

University of Alberta

**Feasibility of Using Hyperspectral Data for Lithologic Mapping in Vegetated Areas
with Low Outcrop Exposure**

by

Jinkai Zhang



A thesis submitted to the Faculty of Graduate Studies and Research in partial fulfillment
of the requirements for the degree of Doctor of Philosophy

Department of Earth and Atmospheric Sciences

Edmonton, Alberta

Spring, 2004



Library and
Archives Canada

Bibliothèque et
Archives Canada

Published Heritage
Branch

Direction du
Patrimoine de l'édition

395 Wellington Street
Ottawa ON K1A 0N4
Canada

395, rue Wellington
Ottawa ON K1A 0N4
Canada

Your file *Votre référence*

ISBN: 0-612-96343-8

Our file *Notre référence*

ISBN: 0-612-96343-8

The author has granted a non-exclusive license allowing the Library and Archives Canada to reproduce, loan, distribute or sell copies of this thesis in microform, paper or electronic formats.

L'auteur a accordé une licence non exclusive permettant à la Bibliothèque et Archives Canada de reproduire, prêter, distribuer ou vendre des copies de cette thèse sous la forme de microfiche/film, de reproduction sur papier ou sur format électronique.

The author retains ownership of the copyright in this thesis. Neither the thesis nor substantial extracts from it may be printed or otherwise reproduced without the author's permission.

L'auteur conserve la propriété du droit d'auteur qui protège cette thèse. Ni la thèse ni des extraits substantiels de celle-ci ne doivent être imprimés ou autrement reproduits sans son autorisation.

In compliance with the Canadian Privacy Act some supporting forms may have been removed from this thesis.

Conformément à la loi canadienne sur la protection de la vie privée, quelques formulaires secondaires ont été enlevés de cette thèse.

While these forms may be included in the document page count, their removal does not represent any loss of content from the thesis.

Bien que ces formulaires aient inclus dans la pagination, il n'y aura aucun contenu manquant.

Canada

ABSTRACT

This study explores the feasibility of using hyperspectral data for lithologic mapping in the presence of vegetation and lichens. Three topics relevant to the analysis of such data were addressed, namely the impact of vegetation on the extraction of geological endmembers, the development of novel spectral mixture models to facilitate the retrieval of rock signatures, and the deconvolution of lichen and rock mixtures.

The research first uses a case study to demonstrate the challenges and a proposed strategy to conduct lithologic mapping in low outcrop vegetated areas using hyperspectral data. The results indicate that the convex-based endmember selection procedure may not be optimal to provide useful rock endmembers from the hyperspectral data in vegetated areas. Also a traditional image-to-map accuracy assessment methodology may not be adequate to perform accuracy checks when map units consist of small dispersed patches. The selection of rock endmembers and validation of unmixing results should be guided by field observations and spectral measurements. The second part of the thesis reports a novel partial unmixing method, Derivative Spectral Unmixing (DSU), incorporating derivative analysis into spectral mixture analysis. By focusing the analysis on an absorption feature unique to an endmember of interest, the DSU allows estimation of the abundance of the endmember without a thorough knowledge of the remaining endmembers. The robustness of DSU was demonstrated using a hyperspectral cube generated in the laboratory for a rock sample. Lastly, the study focuses on the deconvolution of lichen-rock mixtures using the Normalization Linear Mixture Model (NLMM). The results suggest that it is feasible to deconvolve lichen-rock mixtures using the NLMM with one of any field/laboratory lichen spectra. Thus geologists can group all

lichens into one endmember and further the analysis of rock and lichen mixtures without a detailed knowledge of lichen species occurring in the region of interest.

ACKNOWLEDGEMENTS

I would like to acknowledge first and foremost my supervisor and mentor, Dr. Benoit Rivard, for his constant support and encouragement, for carefully reading the manuscript, improving my English writing skills and providing valuable suggestions. He continually offered scientific insight and thoughtful criticism throughout my program. I feel honored to work and study with Dr. Rivard, who has been taking time and effort to teach me lessons that are beneficial both for my academic and professional career.

I am indebted to Dr. Arturo Sanchez for his constructive criticism and suggestions on data analysis methodology during my research. His help is invaluable to my research. I'd like to thank my other committee members, Dr. Andrew Bush, Dr. Jeremy Richards and Dr. Terry Caelli for their precious direction and advice guiding my research.

I would also like to thank Prof. CUI Chengyu of the Institute of Remote Sensing Applications (IRSA), Chinese Academy of Sciences, for his encouragement and suggestions during the early development of the thesis topic.

Thanks to Bechtel Robert for providing access to his spectral library for lichens, Karl Staenz of the Canada Center for Remote Sensing for access to ISDAS. Thanks to my friend, Jilu Feng, for his help in the spectral measurements and constructive suggestions for my research.

Thanks to Geoide National Centre of Excellence, NSERC, Canadian Foundation for Innovation, Noranda Ltd. and EarthScan Ltd. These institutions and industrial partners provided funding or in kind support for my research.

I am grateful for the study and research environment provided by Department of

EAS, university of Alberta. I thank all the members of the Earth Observation Systems Laboratory for their collective help and support.

Last but not least, I would like to thank my wife Yunping, and my son Daiwei for all of their love, cheer, and motivation. I also thank my parents, my brothers, my sisters, and my in-laws, for all of their support and understanding throughout my endless education.

TABLE OF CONTENTS

LIST OF TABLES

LIST OF FIGURES

LIST OF SYMBOLS AND ABBREVIATIONS

CHAPTER 1: INTRODUCTION	1
1.1 Background	1
1.2 Key research avenues	2
1.3 Thesis organization and Research conducted in this thesis	6
1.4 Major contribution to science	9
REFERENCES	10

CHAPTER 2: LITHOLOGIC MAPPING IN VEGETATED AREAS WITH LOW ROCK OUTCROP EXPOSURE USING PROBE-1 HYPERSPECTRAL

DATA	15
2.1 Introduction	15
2.2 Study area	17
2.3 Field reflectance spectra	18
2.3.1 Calibration sites	19
2.3.2 Lithologic units	19
2.4 Indoor reflectance spectra	20
2.5 View from Probe-1	22
2.5.1 Data acquisition and calibration	22

2.5.2 Data analysis	23
2.5.3 Unmixing results and accuracy assessment	26
2.6 Discussion and conclusion	28
2.6.1 Limitations of SMA	28
2.6.2 Limitations of the accuracy assessment method	29
REFERENCES	31

CHAPTER 3: DERIVATIVE SPECTRAL UNMIXING OF HYPERSPECTRAL

DATA APPLIED TO MIXTURES OF LICHEN AND ROCK 47

3.1 Introduction	47
3.2. Description of the model	50
3.2.1 Calculation of derivatives	50
3.2.2 Noise and smoothing	52
3.2.3 Derivative spectral unmixing (DSU)	53
3.3 Experiment	56
3.4 Selection of endmembers	57
3.5 Results	60
3.6 Discussion	60
3.7 Conclusions	61
REFERENCES	62

CHAPTER 4: SPECTRAL UNMIXING OF NORMALIZED REFLECTANCE

DATA FOR THE DECONVOLUTION OF LICHEN AND ROCK	
MIXTURES	73
4.1 Introduction	73
4.2 Materials and methods	75
4.2.1 Data acquisition	75
4.2.2 Spectral features of lichens	77
4.2.3 Spectral mean normalization	78
4.2.4 SMA of normalized spectra	79
4.3 Results	81
4.3.1 Impact of the normalization on lichen spectra	81
4.3.2 Impact of the normalization on the extraction of image endmembers	82
4.3.2.1 Visual extraction	82
4.3.2.2 Automated extraction	83
4.3.3 Unmixing results	84
4.4 Discussion and conclusions	85
REFERENCES	88
CHAPTER 5: CONCLUSIONS AND FUTURE WORK	100
5.1 Conclusions	100
5.2 Future work	102
APENDIX 1 DISCRIMINATION BETWEEN LICHEN AND ROCK/MINERALS	
 USING 2ND ORDER DERIVATIVE SPECTRA	104

A1.1 Background	104
A1.2 Description of the data used in this study	105
A1.3 Results	106
A1.3.1 Absorption features of lichen	106
A1.3.2 Optimal band for discrimination of rock and lichen	106
A1.3.3 Rock-lichen mixtures for the quartzite sample	107
A1.4 Discussion and conclusion	109
REFERENCES	110

LIST OF TABLES

CHAPTER 4:

Table 4-1 Spectral angle (radian) between five lichen species measured from 2000-2400 nm. (The spectrum for each species for the corresponding spectral region is shown on Figure 4.3a.)	92
Table 4-2 Statistics for regressions between the unmixing results and true abundance for rock and lichen	93

LIST OF FIGURES

CHAPTER 2:

- Figure 2.1. Field photograph of a diorite outcrop. Note the presence of rock encrusting lichen on the bedrock surface. 36
- Figure 2.2. Field reflectance spectra of basalt (a) and rhyolite (b). The strong water absorption features near 1900nm and 1400nm were discarded because of low signal-to-noise ratio. (a) solid lines: mean spectra for two field traverses, thin dashed line: yellow lichen, thick dashed line : grey lichen, thin dotted line: weathered basalt. Main lichen features are labeled. (b) solid lines: mean spectra for two traverses, dashed lines: one standard deviation from the mean. 37
- Figure 2.3. Indoor spectra of granite (a) and diorite (b). (a) solid line: broken surface, other lines: weathered surfaces; (b) solid line: broken surface, other lines: weathered surfaces. 38
- Figure 2. 4. Spectra used for the calibration of the Probe-1 data. (a) Uncorrected Probe-1 data for 5 calibration sites; (b) field spectra for corresponding calibration sites; (c) comparison between corrected Probe-1 spectrum and corresponding field spectrum for a site occupied by mafic volcanic rocks. The calibrated data remain noisy at 440nm, 1304-1503nm, 1772-2050nm and 2427-2501nm; thus these bands were excluded from the analysis. 39-40
- Figure 2.5. Endmember spectra extracted using the vertices of the simplex encompassing the data cloud shown in the upper right corner. Each colored cluster of pixels represents a potential endmember. (a): results including vegetated pixels. Labels for spectra are: a = vegetation 1, b = vegetation 2, c = vegetation 3, d = vegetation

4, e = gravel/sand 1, f = lake beach, g = shallow water, h= gravel/sand 2.

(b): results after masking vegetated pixels. Frames A and B respectively show absorption features for chlorophyll in residual vegetation and lichen and a lichen-specific feature. Labels for spectra are: a = rhyolite+vegetation+lichen, b = rhyolite+vegetation+lichen, c = soil, d = rhyolite+vegetation+lichen , e = rhyolite+vegetation+lichen and f = water. Labeling was conducted using the published geological map. 41-42

Figure 2.6. Endmember spectra used in the MTMF. Granite and rhyolite were extracted from the calibrated image cube. Diorite and basalt are average indoor or field spectra. 43

Figure 2.7. SMA results compared with geological map. (a) Geological map from Noranda inc.; (b) SMA results; (c) RGB color composite of bands at 849 nm (R), 652 nm (G), and 452nm (B). Box A: the single portion that is predicted as granite by SMA; Box B: the region where the geological map displays diorite as the unit interspersed with rhyolite whereas the SMA predicts the occurrence of basalt. 44- 45

Figure 2.8. Spectra extracted from the calibrated Probe-1 data within location A (refer to Figure 2.7). Rock-1(thin line) was extracted from pixels labeled as granite on the geological map. Rock-2 (thick line) is for pixels labeled as rhyolite on the geological map. 46

CHAPTER 3:

Figure 3.1 Photograph of the lichen encrusted quartzite sample and resulting

hyperspectral data cube. (a) Digital photo of rock sample showing green lichen (*R. geographicum*) and black lichen (*R. bolanderi*) and the red cross marks used for coregistration with the spectral data; (b) schematic diagram of the spectral measurement layout. Each cell (0.45 cm by 0.45cm) is corresponding to one spectral measurement; the sample is translated through the field of view of the instrument along two directions (showed by the two arrows), that correspond to the image rows and columns in (c); (c) Hyperspectral image cube generated according to the measurement layout illustrated in (b). This is a three dimensional view of the spectral data. The front face is a color composite of bands 430nm (Blue), 550nm (Green) and 710nm (Red). The top and side faces of the cube are colored to show the reflectance variation with wavelength of pixels in the first row and last column (red means high value). 66

Figure 3.2 Endmember spectra for green lichen, black lichen and rock. The selection of the spectra is detailed in section 3.4. The strong water absorption feature near 1900 nm was discarded because of low signal. Box A marks the 680nm region where green lichen has a unique absorption feature. Box B marks the 2195nm region where quartzite has a diagnostic absorption feature. 67

Figure 3.3 2nd derivative endmember spectra for quartzite, green lichen and black lichen at 680 nm (A) and 2195 nm (B). Quartzite has an overwhelming 2nd derivative value compared to green and black lichen at 2195nm while green lichen has distinct values near 680nm. 68

Figure 3.4 Mean, minimum, maximum, and standard deviation (STD) of 2nd derivatives values at 680 nm (A) and 2195 nm (B) for locations of the sample with green

lichen, black lichen and quartzite (rock).

69

Figure 3.5 Comparison between the abundances of green lichen (A) and quartzite (B) estimated using the DSU and “true” abundances observed from the digital photo. In both instances, the linear correlation has a slope <1 indicating that the DSU underestimates the true abundances. The circled areas show that data points tend to cluster when “true values” are approaching 0% or 100%, which reflects the natural variability of endmember surfaces that is not accounted for by DSU.

70-71

Figure 3.6 Distribution of the absolute errors of the estimated abundances for green lichen and rock. The error was calculated by subtracting the estimated abundance from the true abundance. The “X” symbol marks the median value for all the pixels; the box is for 15% and 85% percentile; whiskers for 5% and 95% percentile.

72

CHAPTER 4:

Figure 4.1 Photograph of the lichen encrusted quartzite sample and resulting hyperspectral data cube. (a) Digital photo of rock sample showing green lichen (*R. geographicum*) and black lichen (*R. bolanderi*) and the red cross marks used for coregistration with the spectral data; (b) schematic diagram of the spectral measurement layout. Each cell (0.45 cm by 0.45cm) is corresponding to one spectral measurement; the sample is translated through the field of view of the instrument along two directions (showed by the two arrows), that correspond to the image rows and columns in (c); (c) Hyperspectral image cube generated

according to the measurement layout illustrated in (b). This is a three dimensional view of the spectral data. The front face is a color composite of bands 430nm (Blue), 550nm (Green) and 710nm (Red). The top and side faces of the cube are colored to show the reflectance variation with wavelength of pixels in the first row and last column (red means high value). 94

Figure 4.2 Type spectra obtained for the sample shown in Figure 1. The strong water absorption feature near 1900 nm was discarded because of low signal. The Box marks the short wave infrared (SWIR) spectral region used in figures below. Quartzite has a strong hydroxyl (OH) absorption feature near 2194nm distinct from the broader absorptions features centered near 2100 nm and 2300 nm displayed by lichen. 95

Figure 4.3 Variability in lichen spectra in reflectance and normalized reflectance. a, b: Spectra of five lichen species. Each spectra is the mean of five different 0.78 cm² locations; c, d: Minimum, maximum value and mean \pm one standard deviation value of thirty pixels (each 0.64 cm²) occupied by lichen (green or black lichen) from the hyperspectral image of the quartzite sample (Figure 4.1). 96

Figure 4.4 Data clusters for the image shown on Figure 4.1 prior to (a and b) and following the spectral normalization (c and d). Circles mark the location for the visual extraction of potential endmembers. Black lines have a unit slope. Pixels occupied solely by lichen are located along this line due to the similarity in their spectral shape but varying magnitude (a, b). The distinction between two lichen endmembers is removed (d) or substantially reduced (c) (0.018 at 1730nm in c versus 0.32 in a). 97

Figure 4.5 Endmember spectra predicted using the IEA for a: the reflectance image, b: the normalized reflectance image. A single lichen endmember is required to solve the lichen-rock mixture of the normalized image. 98

Figure 4.6 Comparison between the abundance of lichen and rock estimated from the photo and the unmixing results using the endmembers shown in figure 4.5. a and b for unmixing results from reflectance data; c and d for unmixing results from normalized reflectance data. For the reflectance image, the unmixing results are abundances directly comparable with that estimated from the photo. For the normalized reflectance image, the unmixing results are weights proportional to the abundances estimated from the photo. 99

APENDIX 1:

Figure A1-1 Comparison between reflectance (a) and 2nd derivative spectra (b) for two lichen species. Solid and dashed lines are for *R. geographicum* and *R. bolanderi* respectively. The dominant lichen spectral features were labeled with vertical blue lines. The spectral region near 1900nm was masked because of the high noise level due to the strong water absorption. 112

Figure A1-2 Mean, standard deviation, minimum and maximum 2nd derivative values observed for the lichen and USGS mineral library at 1730nm and 2100nm. The statistics for lichens and minerals were calculated respectively from 85 spectra over 5 lichen species 481 spectra for 423minerals. The squares are mean values; the boxes are for mean \pm 1STD; the whiskers for maximum and minimum values. 113

Figure A1-3. Second order derivative values at 1730nm (b) and 2100nm (a) for mineral spectra of the USGS library. The x-axis is the index # of the minerals in the USGS library. 114

Figure A1-4 Mean, standard deviation, minimum and maximum 2nd derivative values observed for the lichen and USGS mineral library at 1730nm and 2100nm (9 minerals identified in Figure A1-2b excluded). The squares are mean values; the boxes are for mean \pm 1STD; the whiskers for maximum and minimum values. 115

Figure A1-5. Mean 2nd derivative values of 5 lichen species at 680nm and 1730 nm. Error bars include one standard deviation. 116

Figure A1-6 Scatter plots of reflectance (a) and 2nd derivative values (b) at 680nm and 1730nm measured from the lichen encrusted quartzite sample. Pure pixels for three surface types are marked by circles. 117

LIST OF SYMBOLS AND ABBREVIATIONS

AIS	<i>Airborne Imaging Spectrometer</i>
ATREM	<i>Atmosphere Removal</i>
AVIRIS	<i>Airborne Visible/Infrared Imaging Spectrometer</i>
DSU	<i>Derivative Spectral Unmixing</i>
FOV	<i>Field-of-view</i>
HYDICE	<i>Hyperspectral Digital Imagery Collection Experiment</i>
HyMAP	<i>Hyperspectral Mapping</i>
IEA	<i>Iterative Error Analysis</i>
IFOV	<i>Instantaneous Field of View</i>
ISDAS	<i>Imaging Spectrometer Data Analysis System</i>
MNF	<i>Minimum Noise Fraction</i>
MODTRAN	<i>Moderate-resolution Transmittance</i>
MTMF	<i>Mixture Tuned Matched Filtering</i>
NLMM	<i>Normalization Linear Mixing Model</i>
PCA	<i>Principal Component Analysis</i>
R^2	<i>Square of Correlation Coefficient (R)</i>
RMS	<i>Root Mean Square</i>
USGS	<i>US Geological Survey</i>
SAM	<i>Spectral Angle Mapping</i>
SMA	<i>Spectral Mixture Analysis</i>
STD	<i>Standard Deviation</i>

SWIR	<i>Short Wave Infrared</i>
VIS	<i>Visible</i>
VNIR	<i>Visible and Near-infrared</i>
WNNLS	<i>Weighted Nonnegative Least Squares</i>

CHAPTER 1

INTRODUCTION

1.1 BACKGROUND

Imaging spectrometry data or hyperspectral imagery acquired using airborne sensors have been used for geological investigations since the early 1980's. These systems acquire image data in hundreds of contiguous spectral bands with high spectral resolution ($< 20\text{nm}$), and laboratory quality spectrum can be constructed for each pixel in the scene (Clark, 2000). Past research has demonstrated that a key contribution of hyperspectral remote sensing to geology is to uniquely identify spectrally distinct minerals (e.g. hydroxyl bearing minerals) or lithologic units (Clark et al., 1993; Gaffey et al., 1993; Goetz et al., 1985; Mustard and Pieters, 1987; Farrand and Singer, 1991; Kruse 1993; Farrand and Harsanyi, 1995).

Among various hyperspectral analysis methods (Cloutis, 1996; Mustard and Sunshine, 1999), spectral mixture analysis (SMA) (Smith et al., 1990; Settle, 1996; Hu et al., 1999; Petrou and Foschi, 1999) deserves particular attention for lithologic mapping because the natural spatial variation of surface types (bedrock, vegetation, soil) occurs at scales smaller than the spatial resolution of sensors (Settle, 1993). Consequently the spectrum acquired by remote sensors is composed of the spectral contributions of multiple materials within the instantaneous field of view (IFOV). The basic premise of spectral mixture analysis (SMA) is that within a given scene, the surface is dominated by a small number of common materials with relatively constant spectral properties. It follows that the pixel-to-pixel variability in the scene is a result of varying proportions of

these ground components (usually referred as endmembers). The mixtures of endmembers are mathematically linear if the components are arranged in spatially distinct patterns, analogous to the squares on a checkerboard (Singer and McCord, 1979). Typically this approach involves two steps: to find spectrally unique signatures of endmembers and to express individual pixels as a linear combination of endmembers (Boardman, 1993). Endmembers needed for the unmixing can be selected in different ways. Library spectra can be used to unmix a scene or endmembers can be selected directly from the image. One of the new perspectives opened by this approach, together with the improved spectral resolution of sensors, is the possibility to quantify the abundances or fractions of endmembers within each pixel. Many researchers have demonstrated the applicability of SMA for mineral or lithologic mapping under sparse vegetation cover using hyperspectral data (Mustard and Pieters, 1987; Gillespie et al., 1990; Boardman and Huntington, 1996; Neville et al., 1998; Staenz et al., 1999).

1.2 KEY RESEARCH AVENUES

The advent of commercial airborne hyperspectral sensors in recent years has resulted in a surge of activity to use this technology for mineral exploration. A particular challenge for mineral mapping is the application of conventional analysis techniques to areas with substantial vegetation. Unlike sparsely vegetated regions in dry deserts, vegetation (including lichen) covers a larger proportion of rock surfaces in high latitude environments, complicating the extraction of mineral spectral features required for the production of mineral maps using imaging spectrometer data. The following key research avenues were identified in this research:

(a) The extraction of geological endmembers in the presence of vegetation (including rock-encrusting lichens). The most challenging work in spectral mixture analysis is to define a suite of spectral endmembers from the image data. For vegetated areas, the rock reflectance spectra that we aim to detect will be influenced by the presence of vegetation or lichen in the measured pixel (Murphy, 1995; Ager and Milton, 1987). Seigal and Goetz (1977) reported that weak mineral absorption features in the short-wave infrared (SWIR) could be obscured by as little as 10 percent green vegetation. Typically, the selection of image endmembers is achieved through the application of convex geometry, which has been shown to be very useful in arid/semiarid environments (Boardman, 1993). Principal Component Analysis (PCA; Bateson and Curtiss, 1997) or the Minimum Noise Fraction (MNF) transform (Green et al., 1988) are commonly required to reduce the data dimensionality for the visual analysis in this selection process. Because these dimension reduction methods are fundamentally statistical approaches dependent on the specific spectral characteristics of the scene, the variance in each band is crucial for the transformed result. In vegetated areas, rock outcrops commonly occupy a very low percentage of the land cover. Most of the scene variance will be determined by the dominant cover type, i.e. vegetation, which means that the transformed data may be optimal for the analysis of vegetation, but not for geological targets. When the data are viewed in n-dimensions using visualization tools to determine endmembers, the geological units/endmembers identified in the field may be unrecognized in the spectral feature space. The evaluation of the impact of vegetation on the extraction of geological endmembers will provide some guidelines for geological mapping using SMA in vegetated region.

(b) The deconvolution of lichen and rock mixtures. Outcrops in tundra environments are typically encrusted with lichens of various species. Lichens reduce the effective area of bedrock available for remote observation, potentially hampering the discrimination of varying rocks and minerals using spectral observations. Lichen may increase or decrease the rock reflectance (Satterwhite et al., 1985) and even mask some absorption features of the host rock (Ager and Milton, 1987; Rivard and Arvidson, 1992). One study has shown that lithologic mapping is feasible using mixtures of lichen and rock as image endmembers (Staenz et al. 2000), but the identification and abundance estimation of minerals using SMA is negatively impacted. The linear spectral mixture analysis provides a potential tool to address the complexity introduced by lichens (Bechtel et al., 2002), but two basic issues relevant to the selection of a lichen endmember remain unresolved: (a) Given that lichen rarely dominates the pixels of current hyperspectral data, one must rely on field or laboratory measurements of varying lichens to define one or more lichen endmember spectra. Consequently we have to deal properly with the differences in viewing and illumination geometry between field/laboratory spectra and imagery. (b) Given a lack of *a priori* knowledge of the lichen species occurring in a study area, how many lichen endmembers are required to account for the lichen contribution in SMA? Research on this issue will guide the effective incorporation of lichen endmembers into the spectral mixture model to perform a more accurate geological mapping using hyperspectral data in tundra environments.

(c) The development of novel spectral mixture models to suppress the intra-class variation and put a focus on the spectral shape. Defining a set of representative endmembers that are relevant to the mapping objectives is a challenge in SMA. This

issue is two fold. (i) SMA requires all endmembers in the scene to be well constrained in terms of their spectral magnitude and shape. But the spectral magnitude of the endmembers is much more difficult to obtain than their spectral shape in high latitude environments because topographic and atmospheric corrections of the image data are difficult and access to the field is limited. Typically, constraining the spectral shape is more important than the spectral magnitude because the former has a direct relationship with the composition of the target. The development of novel mixture models emphasizing the spectral shape will increase the sensitivity of the spectral mixture analysis to the diagnostic absorption features of geological targets. (ii) SMA uses one endmember spectrum for each class, which makes it difficult to incorporate the intra-class variation in spectral magnitude. It has been reported that the intra-class variation is sufficient to cause large errors in fractional estimates computed from spectral mixture analysis (Bateson et al., 2000). The minimization of intra-class variation should improve the accuracy of the abundance estimate of SMA. Previous studies have demonstrated that the spectral variation across different lichen species is mainly limited to the spectral magnitude in the SWIR spectral region (Rivard and Arvidson, 1992; Bechtel et al., 2002). With the effective suppression of the spectral variation within the lichen class, it will be possible for geologists to group all lichens as a single spectral endmember and use SMA to perform more detailed geological mapping in high latitude environments. The research on this avenue will increase the robustness of spectral mixing analysis and provide some new techniques for geological mapping using hyperspectral data.

This thesis will tackle the above issues using both airborne and laboratory hyperspectral data. The research is aimed at evaluating the limitations of existing

techniques and developing new methodologies to address the challenges associated with the mapping of geological targets in vegetated regions. Though specific problems and methodologies were targeted in this thesis, the science contribution of this thesis resides in the fundamental research results with broad geological applications.

1.3. THESIS ORGANIZATION AND RESEARCH CONDUCTED IN THIS THESIS

This thesis is organized in paper format. Following this introductory chapter, there are three chapters as manuscripts followed by a section summarizing conclusions and future work.

Chapter 2 is a pilot study to demonstrate the challenges and a proposed strategy to conduct lithologic mapping in low outcrop vegetated areas using hyperspectral data. Probe-1 data for a greenstone belt exposed north of Rouyn Noranda, an important gold mining camp of northern Quebec, Canada, was selected to investigate the impact of vegetation on the extraction of geological information. Field spectral observations were collected to document the spectral characteristics and diversity of the major lithologic units and to guide the analysis of the airborne hyperspectral data. The usefulness of a well-established endmember selection procedure based on a MNF transform (Boardman, 1998; Research Systems, Inc., 2000) was evaluated. The partial unmixing algorithm MTMF (Boardman, 1998) was used to discriminate the known broad lithologic units, and results were compared with an existing geological map using a conventional method of accuracy assessment (Congalton, 1991). This study focused on assessing the applicability of existing techniques (e.g. convex-based endmember selection, MTMF, and confusion-

matrix based accuracy assessment) in low rock outcrop environments. Pitfalls and possible modification to these techniques were also outlined. This chapter will be submitted to Photogrammetric Engineering and Remote Sensing with the following authorship: Rivard, B., Feng, J., Zhang, J., and Sanchez, A. Benoit Rivard and Jilu Feng executed the field work, established the premise of the research and the preliminary image analysis, and Arturo Sanchez-Azofeifa provided insightful suggestions for the accuracy assessment. I am third author on this paper. I redid and strengthened the analysis, calibrated the data and wrote much of data analysis, the results and discussions sections. This study was the first to be conducted in my PhD.

Chapter3 presents a Derivative Spectral Unmixing (DSU) model, which is an extension of the spectral mixture analysis (SMA) (Smith et al., 1990; Settle, 1996) and derivative analysis (Tsai and Philpot, 2002). The key strength of the DSU is that the abundance estimation of endmembers does not require a thorough knowledge of all endmembers at hand as long as the unknowns do not display conflicting absorption features with that of the material of interest. It capitalizes on the basic observation that many minerals have absorption features distinct from surrounding rock forming minerals (Hunt, 1977) and those of non-geological targets (e.g. vegetation). The DSU was assessed using spectral data acquired for a lichen covered rock sample, and the estimated fractions of lichen and rock are assessed against those obtained from a high spatial resolution digital photo. DSU is a partial unmixing algorithm because it does not require as input all endmembers present in the scene. It may be of general use as a partial unmixing technique applicable to varied hyperspectral remote sensing scenarios. This chapter was submitted to IEEE Transactions on Geoscience and Remote Sensing with the following

authorship: Zhang, J., Rivard, B., and Sanchez, A. I developed the derivative model and conducted the data generation and analysis. Benoit Rivard had inputs to the analysis and discussion of the results. Arturo Sanchez-Azofeifa provided insightful suggestions for the statistic analysis of the results.

Chapter 4 proposes a new unmixing methodology, the NLMM, to deconvolve lichen-rock spectral mixtures using a limited number of lichen spectral endmembers. In this study, I first investigated the ability of the spectral mean normalization technique to minimize the differences in viewing and illumination geometry between field/laboratory spectra and imagery. Then, based on the similarity of the SWIR spectral shape between different lichen species, the spectral mean normalization was used to suppress these across multiple lichen species. In order to incorporate the advantage of the normalization into SMA, the normalization linear mixing model (NLMM) was designed and assessed using the artificial hyperspectral data cube of one rock sample with lichen coatings. The experimental results showed that one normalized lichen endmember could account for the contribution to the mixture from different lichen species in the NLMM. The model provides a possible method for estimating the relative lichen abundance in sub-pixel scale, and would facilitate further mineral/rock mapping without *a priori* knowledge of the lichen species occurring in a study area. This chapter will be submitted to Remote Sensing of the Environment with the following authorship: Zhang, J., Rivard, B., and Sanchez, A. I conducted the comparative analysis of spectral libraries, developed the mathematical model and performed the data analysis.

Appendix 1 presents results that are closely related to those of Chapter 3. It includes a comparison between the 2nd derivative spectra of the entire USGS mineral spectral library and the lichen spectra of this thesis. The purpose is to utilize the advantage of the derivative spectra to identify spectral regions where lichen can be uniquely distinguished from minerals. The findings are also illustrated using n-dimensional views for the interpretation of mixture relationships between rock and lichen. This appendix is likely to be incorporated in a research note to Remote Sensing of the Environment.

1.4. MAJOR CONTRIBUTIONS TO SCIENCE

The major contributions of this thesis can be summarized as follows:

- (a) The current convex-based endmember selection procedures are not optimal for spectral mixture analysis of imagery for vegetated areas. The selection of endmembers should still be guided by field spectra to perform spectral mixture analysis in vegetated areas. The traditional accuracy assessment methodology may not be adequate to perform accuracy checks when mappable rock units are characterized by small dispersed patches on the image. Field work, rather than image to geological map verifications, may still be the most effective means to assess the results.
- (b) DSU is a promising new concept to map the rock/mineral abundance without detailed knowledge of all endmembers.
- (c) The 2nd derivative value at 1730nm is a robust indicator of the presence of lichen within a pixel. With this finding, the lichen-dominated pixels can be easily identified using the 2nd derivative spectra.

(d) Spectral normalization can suppress within-class variation for a variety of targets including lichen, and the Normalization Linear Mixing Model (NLMM) provides a novel way to unmix lichen-rock mixtures using one lichen endmember. These results suggest that it may be feasible to perform the SMA of airborne/spaceborne imagery in the SWIR using NLMM and one of any field/laboratory lichen spectra. The NLMM provides geologists with an opportunity to group all lichens into one endmember and facilitates the analysis of rock and lichen mixtures without detailed knowledge of lichen species occurring in the region of interest.

REFERENCES

- Ager C. M. and Milton N. M., 1987, Spectral reflectance of lichens and their effects on the reflectance of rock substrates, *Geophysics*, v.52, p. 898-906.
- Bateson, A., Asner, G. P. and Wessman, C. A., 2000, Endmember bundles: A New Approach to Incorporating Endmember Variability into Spectral Mixture Analysis, *IEEE Transactions on Geoscience and Remote Sensing*, v. 38, p.1083-1094.
- Bateson, A. and Curtiss, B., 1997, A method for manual endmember selection and spectral unmixing, *Remote Sensing of Environment*, v. 55, p. 229-243.
- Bechtel, R., Rivard, B. and Sanchez, A., 2002, Spectral properties of foliose and crustose lichens based on laboratory experiments, *Remote Sensing of Environment*, v. 82, p. 389-396.
- Boardman, J.W., 1993, Automating spectral unmixing of AVIRIS data using convex geometry, in summaries of the 4th Airborne Geoscience Conference, *JPL Publication* 93-26, Jet Propulsion Laboratory, Pasadena, CA, v. 1, p.11-14.

- Boardman, J.W., 1998, Leveraging the dimensionality of AVIRIS data for improved subpixel target unmixing and rejection of false positives: Mixture tuned matched filtering, http://popo.jpl.nasa.gov/docs/workshops/98_docs/8.pdf.
- Boardman, J.W. and Huntington, J.F., 1996, Mineral Mapping with 1995 AVIRIS Data: Summaries of the Sixth Annual JPL Airborne Earth Science Workshop, Pasadena, California, U.S.A., *JPL Publication 96-4*, v.1, p. 9-11.
- Clark, R.N., Swayze, G.E., Gallagher, A., King, T.V. and Calvin, W. M., 1993, The U.S. Geological Survey, Digital Spectral Library, Version 1: 0.2-3 um, *USGS Open File Report 93-592*, U.S. Geological Survey, Washington, D.C.
- Clark, R.N., 2000, Spectroscopy of rocks and minerals, and principles of spectroscopy, <http://speclab.cr.usgs.gov/PAPERS.refl-mrs/refl4.html>.
- Cloutis, E.A., 1996, Hyperspectral geological remote sensing - evaluation of analytical techniques, *International Journal of Remote Sensing*, v. 17, p. 2215-2242.
- Congalton, R. G., 1991, A review of assessing the accuracy of classifications of remotely sensed data, *Remote Sensing of Environment*, v. 37, p.35-46.
- Farrand, W.H. and Harsanyi, J.C., 1995, Discrimination of poorly exposed lithologies in imaging spectrometer data, *Journal of Geophysical Research-Planets*, v. 100(E1), p. 1565-1578.
- Farrand, W.H. and Singer, R.B., 1991, Analysis of altered volcanic pyroclasts using AVIRIS data, Proceedings of 3rd Airborne Visible / Infrared Imaging Spectrometer (AVIRIS) Workshop, Pasadena, CA, *JPL Publication 91-28*, v. 1, p. 248-257.
- Gaffey, S. J., Mc Fadden, L.A., Nash, D. and Pieters, C.M., 1993, Ultraviolet, visible, and near-infrared reflectance spectroscopy: laboratory spectra of geologic materials,

- in *Remote geochemical analysis: elemental and mineralogical composition*, C.M. Pieters, and P.A.J. Englert, eds., Cambridge University Press, Cambridge.
- Gillespie, A.R., Smith, M.O., Adams, J.B., Willies, S.C., Fischer, A.F. and Sabol, D.E., 1990, Interpretation of Residual Images: Spectral Mixture Analysis of AVIRIS Images, Owens Valley, California. Proceedings of the Second Airborne Visible/Infrared Imaging Spectrometer (AVIRIS) Workshop, Pasadena, California, *JPL Publication 90-54*, p. 243-270.
- Green A. A., Beramn M., Switzer P. and Craig M. D., 1988. A transformation for ordering multispectral data in terms of image quality and implications for noise removal, *IEEE Transactions on Geoscience and Remote Sensing*, v. 26, p. 65-74.
- Goetz, A.F., Vane, G., Soloman, J.E. and Rock, B.N., 1985, Imaging spectrometry for earth remote sensing, *Science*, v. 228, p. 1147-1153.
- Hu, Y. H., Lee, H. B. and Scarpace, F. L., 1999, Optimal linear spectral unmixing, *IEEE Transactions on Geoscience and Remote Sensing*, v. 37, p. 39–644.
- Hunt, G. R., 1977, Spectral signatures of particulate minerals in the visible and near infrared, *Geophysics*, v. 42, p. 501-513.
- Kruse, F.A., 1993, The spectral image processing system (SIPS) – interactive visualization and analysis of imaging spectrometer data, *Remote Sensing of Environment*, v. 44, p. 145-163.
- Murphy, R.J., 1995, The effects of surface vegetation cover on mineral absorption feature parameters, *International Journal of Remote Sensing*, v. 16, p. 2153 – 2164.
- Mustard, J.F. and Pieters, C.M., 1987, Abundance and distribution of ultramafic microbreccia in Moses Rock dike: Quantitative application of mapping spectroscopy,

- Journal of Geophysical Research*, v. 92(B10), p. 10376-10390.
- Mustard, J.F. and Sunshine, J.M., 1999, Spectral analysis for earth science: investigations using remote sensing data, in: *Remote sensing for earth sciences: Manual of Remote Sensing*, 3rd ed., v.3, ed. A.N. Rencz, John Wiley and Sons, New York, p. 251-307.
- Neville, R.A., Nadeau., C., Levesque, J., Szeredi, T., Staenz, K., Hauff, P. and Borstad, G.A., 1998, Hyperspectral Imagery for Mineral Exploration: Comparison of Data from Two Airborne Sensors, *Proceedings of the International SPIE Symposium on Imaging Spectrometry*, San Diego, California, v. 3438, p. 74- 82.
- Petrou, M. and Foschi, P. G., 1999, Confidence in linear spectral unmixing of single pixels, *IEEE Transactions on Geoscience and Remote Sensing*, v. 37, p. 624–626.
- Research Systems, Inc., 2000, ENVI User's Guide.
- Rivard, B. and Arvidson, E., 1992, Utility of Imaging Spectrometry for Lithologic Mapping in Greenland, *Photogrammetric Engineering and Remote Sensing*, v. 58, p. 945-949.
- Satterwhite, M. B., Henley, J. P. and Carney, J. M., 1985, Effects of Lichens on the reflectance spectra of granite rock surfaces, *Remote Sensing of Environment*, v. 18, p. 105-112.
- Settle, J.J., 1996, On the relationship between spectral unmixing and subspace projection, *IEEE Transactions on Geoscience and Remote Sensing*, v. 34, p. 1045–1046.
- Settle, J.J. and Drake, N. A., 1993, Linear mixing and the estimation of groundcover proportions, *International Journal of Remote Sensing*, v. 14, p. 1159-1177.
- Siegal, B.S. and Goetz, F.H., 1977, Effect of vegetation on Rock and Soil type discrimination, *Photogrammetric Engineering and Remote Sensing*, v. 43, p. 191-196.

- Singer, R.B. and McCord, T. B., 1979, Mars: Large Scale Mixing of Bright and Dark Surface Materials and Implications for Analysis of Spectral Reflectance, *Proceeding of the 10th Lunar and Planetary Science Conference*, p.1835-1848.
- Smith, M., Ustin, S. L., Adams, J. B. and Gillespie, A. R., 1990, Vegetation in deserts: I. A regional measure of abundance from multispectral images, *Remote Sensing of Environment*, v. 31, p.1-26.
- Staenz, K., Neville, R.A., Levesque, J., Szeredi, T., Singhroy, V., Borstad, G.A., and Hauff, P., 1999, Evaluation of *casi* and SFSI Hyperspectral Data for Environmental and Geological Applications – Two Case Studies. *Canadian Journal of Remote Sensing*, v. 25, p. 311-322.
- Staenz K., Secker J., Gao B.C., Davis C, 2000. Spectral Unmixing Applied to Vegetated Environments in the Canadian Arctic for Mineral Mapping, *XIXth ISPRS Congress and Exhibition*, Amsterdam, July 15-23.
- Tsai, F. and Philpot, W. D., 2002, A derivative-aided hyperspectral image Analysis System for land-cover classification, *IEEE Transactions on Geoscience and Remote Sensing*, v. 40, p. 416-425.

CHAPTER 2

LITHOLOGIC MAPPING IN VEGETATED AREAS WITH LOW ROCK OUTCROP EXPOSURE USING PROBE-1 HYPERSPECTRAL DATA

2.1 INTRODUCTION

High spectral resolution (hyperspectral) imaging provides a rich source of compositional information for geological investigations. With the simultaneous acquisition of image data in hundreds of contiguous spectral bands, laboratory quality spectra can be constructed for each pixel in the image (Goetz et al., 1985). When measured as a function of wavelength, the spectra exhibit specific albedo, continuum, and absorption features, which are a function of the material properties of the surface. A key contribution of hyperspectral imaging to geology is the mapping of mineral assemblages or lithologic units. For geological targets, the location of absorption features in the spectra are controlled by the chemical composition (mineralogy) of the surface, whereas the continuum and overall albedo are a function of non-selective absorption and scattering, as well as broad wavelength selective absorptions which can also be influenced by the physical properties of the surface (particle size, roughness, texture, etc.; Clark et al., 1993; Gaffey et al., 1993).

Typically, the methodology used for analysis of hyperspectral data is optimized for the objectives of the local investigation, for example the definition and mapping of broad-scale units. In geological terms this is often the identification of the presence of specific mineralogical assemblages or lithologic units. Mappable units are defined on the basis of shared textural and spectral properties as exhibited in the hyperspectral data.

Commonly the specific compositional properties of the units cannot be determined uniquely from the spectra. In such cases, field investigations can be used to assign field-based names to units defined on the basis of remote sensing analyses, which can then be extended beyond the investigation site on a regional scale.

Numerous studies have demonstrated the applicability of airborne hyperspectral data for mineral mapping in regions of low vegetation cover (Boardman and Huntington, 1997; Kruse, 1988). The advent of commercial airborne hyperspectral sensors in recent years has resulted in a surge of activity by the mining community to use this technology for mineral exploration. There is however little information regarding the feasibility of using these data to conduct lithologic mapping in areas of relatively low rock outcrop partially covered by lichen and surrounded by forest, as is commonly observed in boreal ecosystems. Scene-related factors, such as the presence of lichens on bedrock and topography, may impact the extraction of geological information for such environments. The presence of lichens on rock obscures key spectral features diagnostic of minerals (Rivard and Arvidson, 1992; Bechtel et al., 2002). Lichens reduce the effective area of bedrock available for observation, thereby potentially hampering the discrimination of varying rocks and minerals using spectral observations. The dominance of pixels representing forest in a scene can also hamper the extraction of geological information. Spectral analysis tools such as mixture analysis have been applied successfully for mineral mapping for regions free of vegetation (Kruse, 1997), but their use has yet to be demonstrated in vegetated areas, where data for geological targets is commonly sparse due to low outcrop abundance.

The objective of this chapter is to study the feasibility of conducting reconnaissance geological mapping in a boreal forest ecosystem, with sparse exposure of rock outcrops, using field based and airborne hyperspectral data. The aim is to discriminate the known broad lithologic units of a greenstone belt exposed north of Rouyn Noranda, an important gold mining camp of northern Quebec, Canada. Field based spectral observations are used to document the spectral characteristics and diversity of the main lithologic units and to guide the development of a method for the analysis of airborne hyperspectral data adapted to this environment. The pitfalls of a more traditional endmember extraction approach are discussed. Finally, a traditional accuracy assessment technique was applied to our results using a lithologic map.

2.2 STUDY AREA

The study area is located in the Abitibi greenstone belt immediately north of Rouyn Noranda, approximately 500 km northwest of Montreal in the province of Quebec, Canada (Figure 2.1). The study site occupies 3.3 x 13 km in a terrain characterized by subdued topography with variations in elevation rarely exceeding 70 meters. Boreal forest and agricultural fields are the dominant land cover types in the study area. Bedrock is invariably partially covered by lichen coatings but is largely devoid of other forms of vegetation cover (Figure 2.1). The Abitibi greenstone belt is part of the Superior geological Province of the Canadian shield (Stockwell, 1964) and contains arcuate and complexly deformed metavolcanic belts alternating with metasedimentary belts and intruded by granitic rocks. Felsic volcanic rocks, basalt, granite and diorite are the four dominant rock types exposed within the study area. The metavolcanic rocks are part of

the Blake River group which consists of a bimodal suite of basalts and rhyolites accompanied by felsic volcanoclastic rocks (Dimroth, et al., 1973; Gelinás et al., 1977; Gelinás, 1984). These rocks are intruded by diorite and granite. Minor occurrences of argillites, greywackes and conglomerates of the Pontiac group are found, but more exposures are observed south of the study area. Of particular interest to mining companies is the distribution of felsic volcanic rocks that are closely associated with the occurrence of economic minerals. The Bousquet mine, located approximately 50 km east of the study area, is one of many large gold producing mines in the Abitibi belt.

2.3 FIELD REFLECTANCE SPECTRA

The spectra of dominant rock types in the study area were acquired using a Analytical Spectral Devices FieldSpec FR portable spectroradiometer, which operates in the 350-2500 nm spectral range and is characterized by a resolution of 3 nm at 700 nm, 10 nm at 1500 nm, and 10 nm at 2100 nm (Analytical Spectral Devices, 2001). Measurements were collected at 0° emission angle using solar illumination at high zenith angle and under clear sky conditions. Each measurement was an average of 15 consecutive spectra collected for a ground footprint 12 cm in diameter. Radiance coefficients (Hapke, 1981), e.g. reflectance, were obtained by determining the ratios of data acquired for a sample to data acquired for a spectralon standard panel under the same illumination and observation conditions. Measurement of the standard panel took place within minutes of the natural targets to minimize changes in illumination conditions attributable to atmospheric conditions.

2.3.1 Calibration sites

Reflectance spectra were acquired from four separate calibration sites for the purpose of atmospheric calibration of the Probe-1 airborne data. The sites include a paved surface of 30 by 40 m, a gravel lot 10 by 20 m, and two sand pits. These sites span a range of reflectance values, lack topography, and are not likely to have been disturbed over the one-year period between the ground and airborne surveys. In addition they display relatively uniform spectral characteristics over an area of three by three Probe-1 pixels (21 by 21 m). Linear traverses were conducted at each site, and spectra were acquired at spots at every 1.5m interval within the traverse. More than 30 spectra were collected from each site. The average field spectrum has a standard deviation which does not exceed 4% for all four sites, confirming the compositional and textural homogeneity of the calibration sites.

2.3.2 Lithologic units

Reflectance spectra were obtained for ten bedrock sites representative of the dominant rock types in the region (granite, diorite, felsic volcanic rocks, basalt, and two metasedimentary units). Each site had an exposed surface of one to three Probe-1 pixels (7-21m). Spectra were acquired along linear traverses at an interval of 0.5 m. More than 20 spectra were collected along traverses at each site. In addition an average spectrum was determined for the dominant surface type (weathered rock, lichens) to characterize the spectral endmembers.

Data acquired in the traverse mode provide a measure of the heterogeneity of the natural surface. The variance of these spectra is indicative of the nature of each rock type. The mafic volcanic rocks (dominantly basalt) are fine to medium-grained and appear

relatively homogeneous in the field. This characteristic is evident from the spectral data of two traverses, each encompassing twenty spectra, which display average spectra with less than 2% difference in reflectance (Figure 2.2a). Lichen cover on these rocks consists of two dominant groups (yellow and grey crustose), which were also measured in the field (Figure 2.2a). The average traverse spectra for this rock unit display absorption features around 680 nm and 2100 nm attributable to lichen (Rivard and Arvidson, 1992) and lie closer to the lichen endmembers than that of the weathered rock, indicating that the average spectra are a mixture of weathered basalt with an important contribution by lichen.

In comparison with the mafic volcanic rocks, the felsic volcanic rocks (e.g. flows, lapilli tuffs) are heterogeneous in terms of composition and texture. Variations are observed at the scale of meters in the field. Lichens are present but cover is not extensive, consistent with the lack of a spectral feature near 680 and 2100 nm. The traverse spectra illustrate the variability observed in the field. The average spectra calculated for each of two traverses display a maximum standard deviation of 9% and a maximum reflectance difference of 12% (Figure 2.2b). The weathered felsic volcanic rocks display a set of distinct absorption features at 2200 and 2350 nm (Figure 2.2b), as opposed to the single feature displayed by the mafic volcanic rocks around 2328 nm (Figure 2.2a).

2.4 INDOOR REFLECTANCE SPECTRA

Because of logistical constraints (e.g. accessibility and weather conditions), spectra for granite and diorite were acquired indoors from rock samples. Granite and diorite

appeared in the field to display relatively uniform textural and compositional properties allowing indoor measurement of representative spectra using representative samples with natural and freshly broken surfaces. Measurements from samples preclude an assessment of reflectance at the scale of Probe-1 pixels and of the role of lichens in modulating the reflectance of these rock units. The indoor data were acquired with an incidence angle of 45° , illuminating a footprint of approximately 4.4 cm viewed at an emission angle of 0° . Spectra of weathered granite and weathered diorite (Figure 2.3) display vibration absorption features associated with the presence of water (1400 and 1940 nm), hydroxyl ions (between 2200 and 2350 nm), and the presence of $\text{Fe}^{+2}/\text{Fe}^{+3}$ in the rock forming minerals (between 850-1200 nm). For each rock type the spectra of different weathered surfaces differ in amplitude, but the observed center wavelength position of the absorption features is constant. Variations in amplitude are attributable to micro topography and grain size variations. Diorite displays very uniform spectral properties consistent with the uniform grain size observed in the field. Diorite is characterized by two hydroxyl bands centered around 2263 and 2325 nm (Figure 2.3b). Granite displays two hydroxyl bands centered at lower wavelengths (2199 and 2261 nm) in addition to a band at 2348 nm (Figure 2.3a). The spectra of weathered granite for two samples display variable amplitude possibly indicating that textural variability is more important than assessed in the field.

2.5 VIEW FROM PROBE-1

2.5.1 Data acquisition and calibration

The hyperspectral airborne data were obtained with the Probe-1 sensor on October 4, 1998. Probe-1 is a commercial imaging spectrometer that operates on a variety of platforms. It is a whiskbroom instrument with 128 spectral channels spanning a wavelength range of 440-2500 nm with bandwidths ranging from 11 to 18 nm. The sensor has a 60° field of view and an instantaneous field of view of about 2.5 mrad along track and 2.0 mrad across track. For the flight altitude of this study (3,450 m) the nominal nadir ground resolution is 7 m.

In order to compare the image spectra with the library of field and indoor spectra, the raw data were converted to reflectance values. Radiative transfer models such as MODTRAN (Berk et al., 1989) and ATREM (Gao and Goetz, 1990) could not be used for this purpose because the at-sensor radiance values were not accurate. The cause is an undocumented opto-mechanical realignment of the sensor between the last calibration and its deployment for this study (pers. comm. J.Secker). The average field spectrum for each calibration site was resampled to the Probe-1 bandpass characteristics and regressed against the average digital values derived from the Probe-1 data extracted for the calibration sites. Average spectra were used to minimize sensor noise and any within-target variations. Linear fits were performed for each band; the slope and intercept values carry atmospheric and instrumental effects and allow radiance coefficients for the surface to be extracted from the Probe-1 data. In using this approach, it is assumed that there are no variations in illumination across the image; therefore, changes in radiance due to the presence of clouds or topography are ignored. This simple method has been

extensively used to calibrate hyperspectral data to reflectance (Roberts et al., 1986; Conel et al., 1987; Kruse et al., 1990).

Figure 2.4 shows the average Probe-1 uncorrected spectra and corresponding average field reflectance spectra for the calibration sites. The uncertainty of the calibration was assessed by comparing the calibrated Probe-1 data to field reflectance values for additional locations. As shown on Figure 2.4c for a site occupied by mafic volcanic rocks the magnitude of the calibrated reflectance is lower than the field reflectance, but away from atmospheric bands the spectral shapes are similar. This aspect of the calibration results is important for the determination of lithology because the spectral shape is directly related with the mineral composition of the rock.

2.5.2 Data analysis

Spectral mixture analysis (SMA) of hyperspectral data has been shown to be an effective method for mapping mineralogy in sparsely vegetated terrains (Kruse et al., 1990; Kruse et al., 1993; Ben-Dor et al., 1995). SMA is a physically based model that assumes that within a given scene, the surface is dominated by a small number of materials with relatively constant spectral properties. It follows that the pixel-to-pixel variability in the scene results from varying proportions of these common components (endmembers). The mixtures of endmembers are mathematically linear if the components are arranged in spatially distinct patterns, analogous to the squares on a checkerboard (Singer and McCord, 1979). Once endmembers are selected the abundance of each endmember in a given pixel can be determined using the following equations

$$R_b = \sum_{i=1}^m f_i r_{ib} + E_b , \quad (2-1)$$

$$0 \leq f_i \leq 1.0, \sum_{i=1}^m f_i = 1.0, \quad (2-2)$$

where R_b is the reflectance of a pixel at band b , f_i is the fractional abundance of endmember i (from a total of m endmembers), r_{ib} is the reflectance at band b of endmember i , and E_b is the error of the fit for band b . The endmember abundances can be estimated from Eq. 2-1 and 2-2 through least squares technique (Yosio, 1991) or singular value decomposition (Boardman, 1989).

SMA requires that all endmembers in a scene be well identified, a task difficult to accomplish in many instances. Partial unmixing methods provide a means of estimating the fraction of specific endmembers without a complete knowledge of scene endmembers. The Mixture Tuned Matched Filtering (MTMF) algorithm in the ENVI commercial software is based on a spectral detection method presented by Harsanyi and Chang (Harsanyi and Chang, 1994), which maximizes the response of each endmember selected while suppressing the response of the unknown composite background. MTMF was used in this study to predict the abundance of felsic volcanic rocks (rhyolite), mafic volcanic rocks (basalt), diorite, and granite based on endmember spectra extracted from the field and from the scene.

One of the challenges of SMA or MTMF is to define a set of spectral endmembers that are relevant to the mapping objectives and which are representative of the physical components on the surface. Typically the selection of endmembers is achieved through the application of convex geometry, which has been shown to be useful for determining the number of endmembers in a data set, and for estimating their spectral properties (Boardman, 1993). A simplex is fit to the convex hull of the n -dimensional data cloud

and the vertices of the simplex define the spectral properties of the endmembers. The method is repeatable but has the disadvantage that it is fundamentally a statistical approach dependent on the specific spectral characteristics of the scene. The resulting endmembers may not have a physical meaning of relevance to the objectives of the study. When applied to this study it failed to provide useful geological endmembers due to the predominance of non-geological targets (e.g. different vegetation types and water bodies) in the scene.

Figure 2.5 provides an illustration of this method applied to the Probe-1 data of our study area. Without masking pixels dominated by vegetation, the n-dimensional data cloud exhibits several data clusters at the vertices of the simplex (Figure 2.5a), none of which are relevant to the objective of geological mapping. After masking vegetated pixels, the extremities of the data cloud (Figure 2.5b) include mixtures of rock (e.g. rhyolite) and vegetation or lichen identified by the chlorophyll feature around 680nm (Frame A) and a lichen-specific feature near 1730nm (Frame B), illustrating that the spectral variance in the scene is still largely controlled by vegetation (including lichen) at a subpixel scale. In addition, the endmember spectra for important map units (basalt, diorite, and granite) cannot be identified. Thus, this traditional approach for endmember selection does not seem practical for scenes where vegetation dominates and bedrock exposure is minimal. In this study, knowledge of the general geology of the area guided the selection of field sites and thus endmembers. Endmember spectra for granite and felsic volcanic rocks (rhyolite) were extracted from the Probe-1 data for known field sites (Figure 2.6). The variation in amplitude of the field measurements acquired for these lithologic units (Figures 2.2b and 2.3a) indicated that an average measurement over

several Probe-1 pixels would provide a more representative endmember for each unit than could be achieved from the field survey. For diorite we chose a spectrum acquired indoors for the sample most representative of the bedrock textural properties observed in the field. Based on the textural and compositional homogeneity observed in the field for basalt and on the uniformity of average spectra for multiple traverses, an average traverse spectrum was used as an endmember.

2.5.3 Unmixing results and accuracy assessment

The primary result of the SMA is fraction images of endmembers that show the distribution and sub-pixel abundance of the endmember components in the scene. The fraction images can be used to identify lithologic units and map their distribution. In the case of the MTMF two output images are generated per endmember. A 'score' image provides a means of estimating the relative degree of match to the endmember and the approximate sub-pixel abundance. The 'infeasibility' image is used to reduce the number of "false positives" that are sometimes found using matched filters. Pixels with high infeasibility are likely to be matched filter false positives. Two dimensional scatter plots of the score and infeasibility images were used to select correctly matched pixels which should have a high 'score' and low 'infeasibility' value. This threshold operation was guided by our general geological map knowledge of the area. Then, using the Spectral Angle Mapper (SAM) algorithm (Kruse et al., 1993), the eight output images were classified into a single image displaying a class per endmember (Figure 2.7b). SAM is a vector-based approach that measures the angular distance between two vectors as a means for classification. Spectra whose vectors are separated by small angles are considered most similar. As an input to SAM we used the score and infeasibility

signatures of the sites where field spectral measurements and samples were collected to determine the endmembers. The maximum angle in radians was set to preserve the areas shown on the infeasibility and score images. Throughout the analysis, areas dominantly occupied by vegetation were masked from the image in order to reduce the processing time and facilitate the interpretation of the classified score/infeasibility maps (Figure 2.7).

To analyze the unmixing result, the geological map was coregistered with the endmember map (Figure 2.7). A color composite of bands at 849nm (R), 652nm (G), and 452nm (B) (Figure 2.7) shows rock outcrops in blue and vegetation in shades of red, yellow and green, but the composite provides no information on lithology. A visual comparison of the classified unmixing results with the geologic map shows an overall good correspondence between predicted occurrences and the map units. Rhyolite outcrops dominate and form contiguous strips of bedrock exposures which can be traced for hundreds of meters. Basalt is a more recessive unit and as shown by the predicted occurrences forms smaller and more sparsely distributed outcrops commonly not exceeding a few tens of meters. Detected diorite outcrops are sparse and small, only representing a very small fraction of the map unit.

The validity of a mixture model solution using a particular suite of endmembers can be tested using three criteria: the infeasibility image, the score image (absolute values of the fractions), and the spatial patterns and coherency of the fraction images. Typically the absolute values of the fractions are unknown; one relies on the score/infeasibility image as a broad measure of quality of the model and on the spatial coherence of each lithology. To define the spatial extent of a lithology (e.g. an outcrop) and generate a “map”, the method of analysis required that a threshold be applied to retain areas

characterized by a high score and low infeasibility. While some combination of experience with the method and the particular scene can aid in establishing a reasonable threshold, determining the threshold value remains an arbitrary decision. To assess the accuracy of the map resulting from the MTMF (Figure 2.7b) we utilized a common technique for accuracy assessment of land cover map derived from remote sensing (Fitzpatrick-Lins, 1981; Congalton, 1991; Fenstermaker, 1994; Ma and Redmond, 1995). The final accuracy of the SMA maps was determined using a confusion matrix proposed by Congalton (Congalton, 1991). Our results were compared against the lithological map shown on Figure 2.7. Total outcrop mapped represented 0.6% of the study area. The final accuracy assessment, considering an error limit of 30%, indicates that only the rhyolite class was mapped within the acceptable error (77.3% accuracy, 22.7% error). The diorite, basalt and granite classes reported accuracies of 12.3% (87.7% error), 45.8% (54.2% error) and 35.5% (64.5% error), respectively.

2.6. DISCUSSION AND CONCLUSIONS

2.6.1 Limitations of the SMA method

Granite is found in a single portion of the map (location A on Figure 2.7b) and forms pixel-size outcrops (a few tens of meters). Most of the outcrops in the northern part of location A appear on the map as felsic volcanic rocks. An average spectrum was extracted from the calibrated Probe-1 data for a large outcrop in the northern part of location A (rhyolite on the map) and compared with that of the field site visited in the southern part of location A (Figure 2.8). Both spectra are similar in amplitude and display absorption features similar to that of the granite endmember used for the SMA (Figure

2.6). The data suggest that the rhyolite in this portion of the map cannot be distinguished from the granite on spectral grounds, but this limitation appears to be restricted to location A. This limitation is likely the main cause of the poor accuracy results for granite.

Location B on Figure 2.7b presents a difficulty with the interpretation of the results. The SMA results for the rhyolite appear to fit the available map pattern within reasonable limits, but the map displays diorite as the unit interspersed with rhyolite whereas the SMA predicts the occurrence of basalt. In this case there is no obvious limitation introduced by the spectral characteristics of the diorite and basalt endmembers (Figure 2.6) that display distinct absorption features. The cause of the discrepancy has not yet been determined and may rest with the reliability of the geological map.

2.6.2 Limitations of the accuracy assessment method

Many of the diorite and basalt outcrops detected by Probe-1 are small and consist of only a few pixels. In addition, outcrops are often dispersed and their overall occurrence is very low (0.6% for all rock types). The low outcrop occurrence means that a mismatch of a few outcrops will substantially impact the accuracy of the results. In the case of diorite, the SMA results are often in close proximity to areas reported on the map. However since the reported map areas are typically small, small map errors in the location of the contacts or small errors in the coregistration of the image with the geological map will substantially impact the accuracy of the results. Both of these limitations have likely impacted the results for diorite. The fact that most predicted diorite occurrences lie within a few pixels of an equivalent map unit is of use to geologists. For basalts we note that the accuracy is higher than that observed for diorite,

which is likely due to the larger areas reported on the map. As seen from Figure 2.7, many basalt outcrops occur in proximity to contacts with rhyolite. In these cases the same factors affecting the accuracy for diorite would come into play.

Based on these observations, the accuracy assessment method appears to work well for map units with large patches (e.g. rhyolite, basalt) and rock types with substantial outcrop exposure (e.g. rhyolite). For map units characterized by small patches (e.g. diorite), it may be necessary to implement a buffer around every predicted outcrop during the assessment to minimize mapping and registration errors which can substantially degrade the accuracy due to the low abundance of outcrops.

Our results indicate that conventional accuracy assessment techniques may not be adequate to perform accuracy checks when the data present the limitations outlined above. Field work, rather than image to geological map verifications, may still be the most effective means to assess the results.

ACKNOWLEDGEMENTS

Field work was funded by grants to B. Rivard by the Geoides National Centre of Excellence and NSERC and grant 2041 from the Canadian Foundation for Innovation to Arturo Sanchez. We wish to thank John Gingerich, Mike Peshko, and Jules Riopel from Noranda Inc. for field support and access to the Probe-1 hyperspectral data. Greg Lipton of EarthScan Ltd provides field support. This is contribution #10 of the Earth Observation Systems Laboratory.

REFERENCES

- Analytical Spectral Devices, 2001, www.asdi.com
- Bechtel, R., Rivard, B. and Sanchez, A., 2002, Spectral properties of foliose and crustose lichens based on laboratory experiments, *Remote Sensing of Environment*, v. 82, p. 389–396.
- Ben-Dor, E. and Kruse, F.A., 1995, Surface mineral mapping of Makhtesh Ramon Negev, Israel using GER 63 channel scanner data, *International Journal of Remote Sensing*, v. 16, p. 3529-3553.
- Berk, A., Bernstein, L.S. and Robertson, D.C., 1989, MODTRAN: A moderate resolution model for LOWTRAN 7, Final Report, GL-TR-0122, AFGL, Hanscom, AFB, Maryland, USA, 37 p.
- Boardman, J.W., 1989, Inversion of imaging spectrometer data using singular value decomposition, in *Proceedings of IGARSS'89, 12th Canadian Symposium on Remote sensing*, p. 2069-2072.
- Boardman, J.W., 1993, Automating spectral unmixing of AVIRIS data using convex geometry concepts, *Summaries of the fourth Annual JPL airborne Geoscience Workshop, JPL Publication 93-26*, v. 1, p. 11-14.
- Boardman, J.W. and Huntington, J.F., 1997, Mineralogical and Geochemical Mapping at Virginia City, Nevada using 1995 AVIRIS Data, in *Proceedings of the 12th ERIM Conference on Applied Geological Remote Sensing*, Denver, p. I191-I198.
- Clark, R.N., Gallagher, A.J. and Swayze, G.A., 1990, Material absorption band depth mapping of imaging spectrometer data using a complete band shape least-squares fit

- with library reference spectra, In *Proceedings of 2nd Airborne Visible/Infrared Imaging Spectrometer (AVIRIS) Workshop, JPL Publication 90-54*, Jet Propulsion Laboratory, pp. 176-186.
- Clark, R.N., Swayze, G.E., Gallagher, A., King, T.V. and Calvin, W. M., 1993, The U.S. Geological Survey, Digital Spectral Library, Version 1: 0.2-3 um, *USGS Open File Report 93-592*, U.S. Geological Survey, Washington, D.C.
- Conel, J. E., Green, R. O., Vane, G., Bruegge, C. J., Alley, R. E. and Curtiss, B. J., 1987, Airborne imaging spectrometer-2: radiometric spectral characteristics and comparison of ways to compensate for the atmosphere, in *Proceedings, SPIE*, v. 834, p. 140 - 157.
- Congalton, R. G., 1991, A review of assessing the accuracy of classifications of remotely sensed data, *Remote Sensing of Environment*, v. 37, p. 35-46.
- Dimroth, E., Boivin, P., Goulet, N. and Larouche, M., 1973, Tectonic and volcanological studies in the Rouyn-Noranda area, Quebec Dept Nat. Resources, Open File manuscript, p. 1-60.
- Fenstermaker, L. K., 1994, *Remote Sensing Thematic Accuracy Assessment: A Compendium*, Bethesda, Maryland, American Society for Photogrammetry and Remote Sensing.
- Fitzpatrick-Lins, K., 1981, Comparison of Sampling Procedures and Data Analysis for a Land-Use and Land-Cover Map, *Photogrammetric Engineering and Remote Sensing*, v. 47, p. 343-351.
- Gaffey, S. J., Mc Fadden, L.A., Nash, D. and Pieters, C.M., 1993, Ultraviolet, visible, and near-infrared reflectance spectroscopy: laboratory spectra of geologic materials,

- in *Remote geochemical analysis: elemental and mineralogical composition*, C.M. Pieters, and P.A.J. Englert, eds., Cambridge University Press, Cambridge, p. 43-78.
- Gao, B.C. and Goetz, A.F.H., 1990, Column atmospheric water vapour and vegetation liquid water retrievals from airborne imaging spectrometer data, *Journal of Geophysical Research*, v. 95, p. 3549-3564.
- Gelinas, L., Brooks, C., Perreault, G., Carignan, J., Trudel, P. and Grasso, F., 1977, Chemo-stratigraphic division within the Abitibi volcanic belt, Rouyn-Noranda, Quebec, in *Volcanic regimes in Canada*, W.R.A. Baragar, L.C. Coleman, and J.H. Hall eds. Geological Association of Canada, Special Paper 16, p. 265-295.
- Gelinas, L., Trudel, P. and Hubert, C., 1984, Chemo-stratigraphic divisions of the Blake River Group, Rouyn-Noranda, Abitibi, Quebec, *Canadian Journal of Earth Sciences*, v. 21, p. 220-231.
- Goetz, A.F., Vane, G., Soloman, J.E. and Rock, B.N., 1985, Imaging spectrometry for earth remote sensing. *Science*, v. 228, p. 1147-1153.
- Hapke, B., 1981, Bidirectional Reflectance Spectroscopy 1: Theory, *Journal Geophysical Research*, v. 86, p. 3039-3054.
- Harsanyi, J.C. and Chang, C. I., 1994, Detection of low probability subpixel targets in hyperspectral image sequences with unknown backgrounds, *IEEE Transactions on Geoscience and Remote Sensing*, v. 32, p. 779-785.
- Kruse, F.A., 1988, Use of Airborne Imaging Spectra Data to Map Minerals Associated with Hydrothermally Altered Rocks in the Northern Grapevine Mtns., Nevada and California, *Remote Sensing of Environment*, v. 24, p. 31-51.

- Kruse, F. A., 1997, Regional geological mapping along the Colorado Front Range from Ft. Collins to Denver using the Airborne Visible/Infrared Imaging Spectrometer (AVIRIS), *Proceedings of the 12th ERIM Conference on Applied Geological Remote Sensing*, Denver, p. II91-II98.
- Kruse, F. A., Kierein-Young, K. S. and Boardman, J. W., 1990, Mineral mapping at Cuprite, Nevada with a 63 channel imaging spectrometer, *Photogrammetric Engineering and Remote Sensing*, v. 56, p. 83-92.
- Kruse, F.A., Lefkoff, A.B. and Dietz, J.B., 1993, Expert system based mineral mapping in northern Death Valley, California/Nevada using the airborne visible/infrared imaging spectrometer (AVIRIS), *Remote Sensing of Environment*, v. 44, p. 309-335.
- Ma, Z. and Redmond, R., 1995, Tau Coefficients for Accuracy Assessment of Classification of Remote Sensing Data, *Photogrammetric Engineering and Remote Sensing*, v. 61, p. 435-439.
- Rivard, B. and Arvidson, E., 1992, Utility of Imaging Spectrometry for Lithologic Mapping in Greenland, *Photogrammetric Engineering and Remote Sensing*, v. 58, p. 945-949.
- Roberts, D. A., Yamaguchi, Y. and Lyon, R. J. P., 1986, Comparison of various techniques for calibration of AIS data, in *Proceedings, 2nd AIS workshop, JPL Publication 86-35*, Jet Propulsion Laboratory, Pasadena, CA, p. 21-30.
- Singer, R.B. and McCord, T. B., 1979, Mars: Large Scale Mixing of Bright and Dark Surface Materials and Implications for Analysis of Spectral Reflectance, *Proceeding of the 10th Lunar and Planetary Science Conference*, p.1835-1848.

Stockwell, C. H., 1964, Fourth report on structural province, orogenesis, and time classification of rocks of the Canadian Precambrian shield, *Geological survey of Canada*, Paper 64-17, part II, p. 1-21.

Yosio, E., 1991, The least-square mixing models to generate fraction images derived from remote sensing multispectral data, *IEEE Transactions on Geoscience and Remote Sensing*, v. 29, p.16-20.

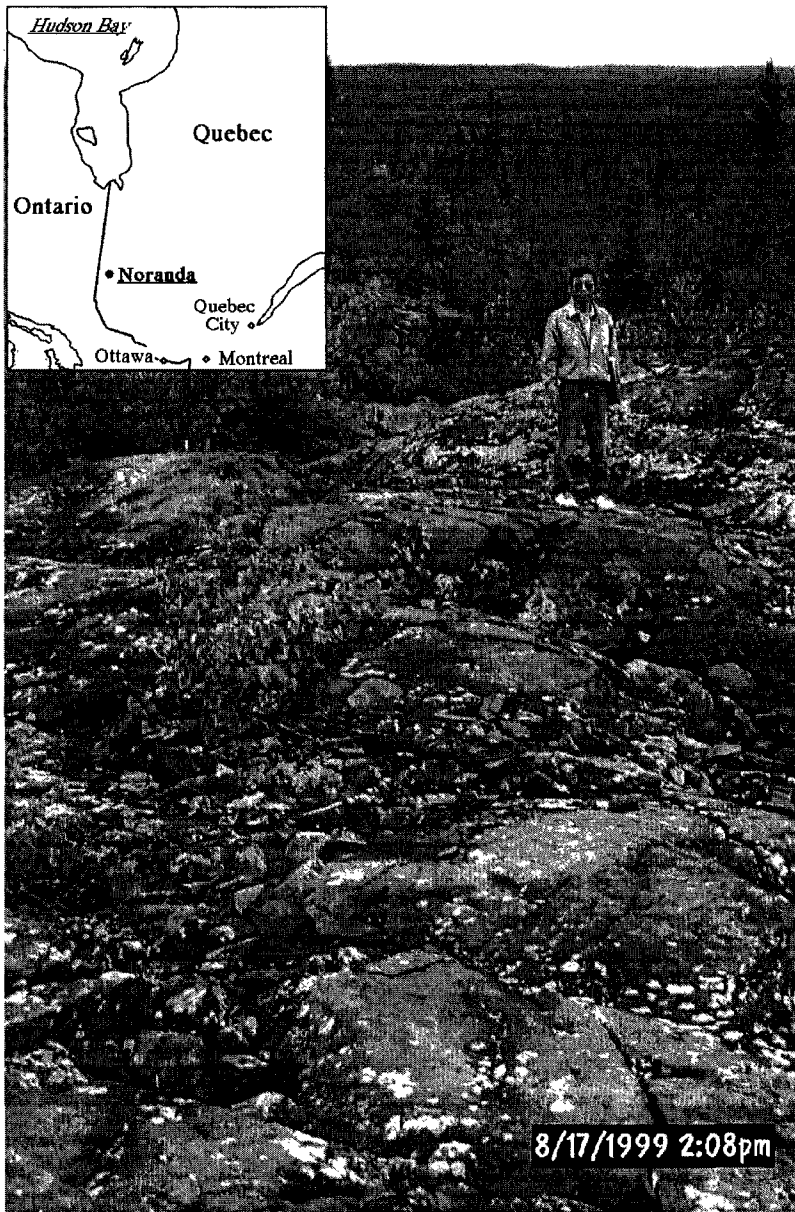


Figure 2.1. Field photograph of a diorite outcrop. Note the presence of rock encrusting lichen on the bedrock surface.

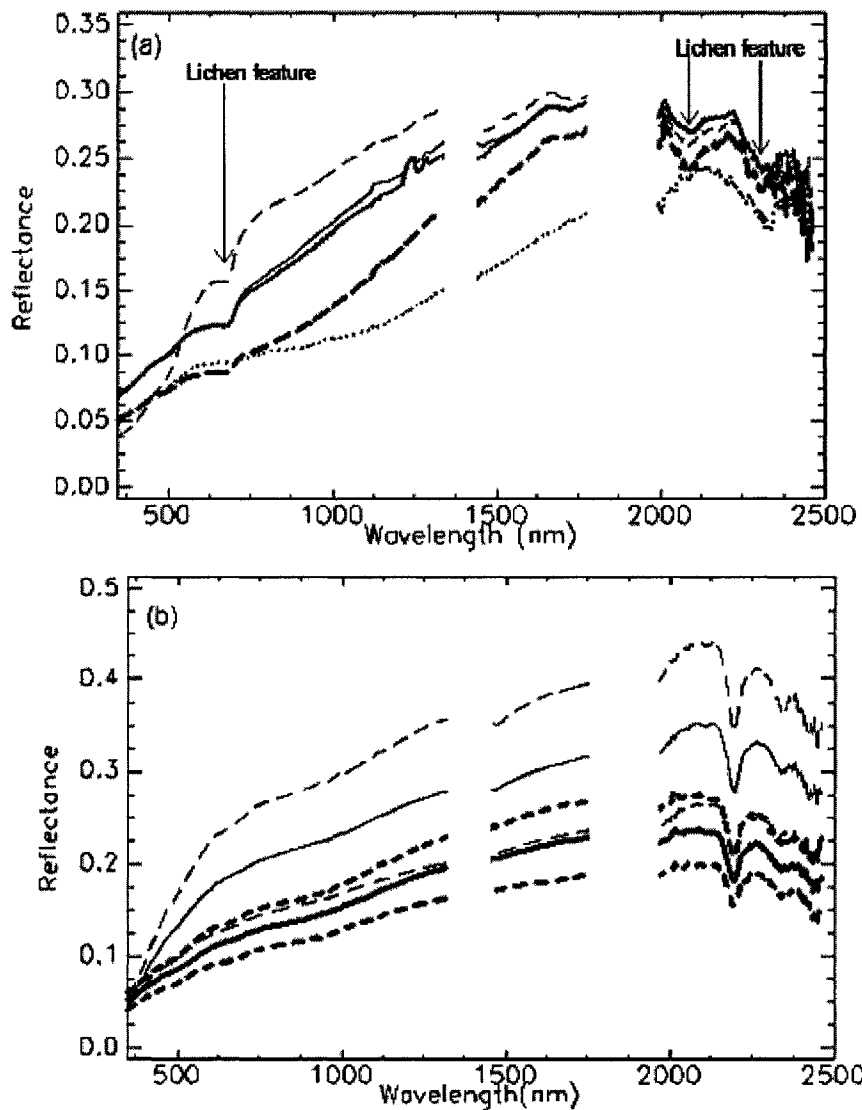


Figure 2.2. Field reflectance spectra of basalt (a) and rhyolite (b). The strong water absorption features near 1900nm and 1400nm were discarded because of low signal-to-noise ratio.

(a) solid lines: mean spectra for two field traverses, thin dashed line: yellow lichen, thick dashed line : grey lichen, thin dotted line: weathered basalt. Main lichen features are labeled.

(b) solid lines: mean spectra for two traverses, dashed lines: one standard deviation from the mean.

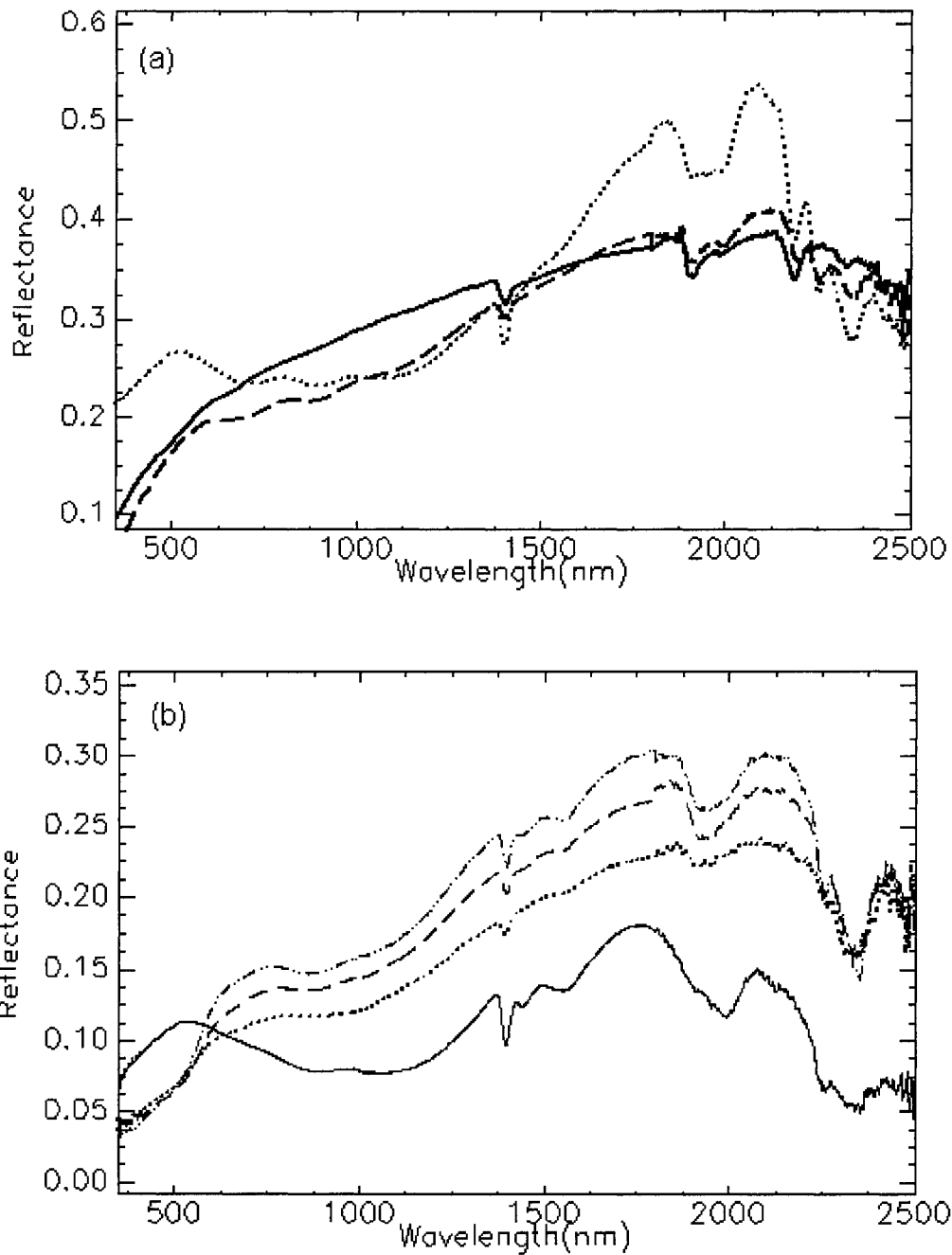


Figure 2.3. Indoor spectra of granite (a) and diorite (b). (a) solid line: broken surface, other lines: weathered surfaces; (b) solid line: broken surface, other lines: weathered surfaces.

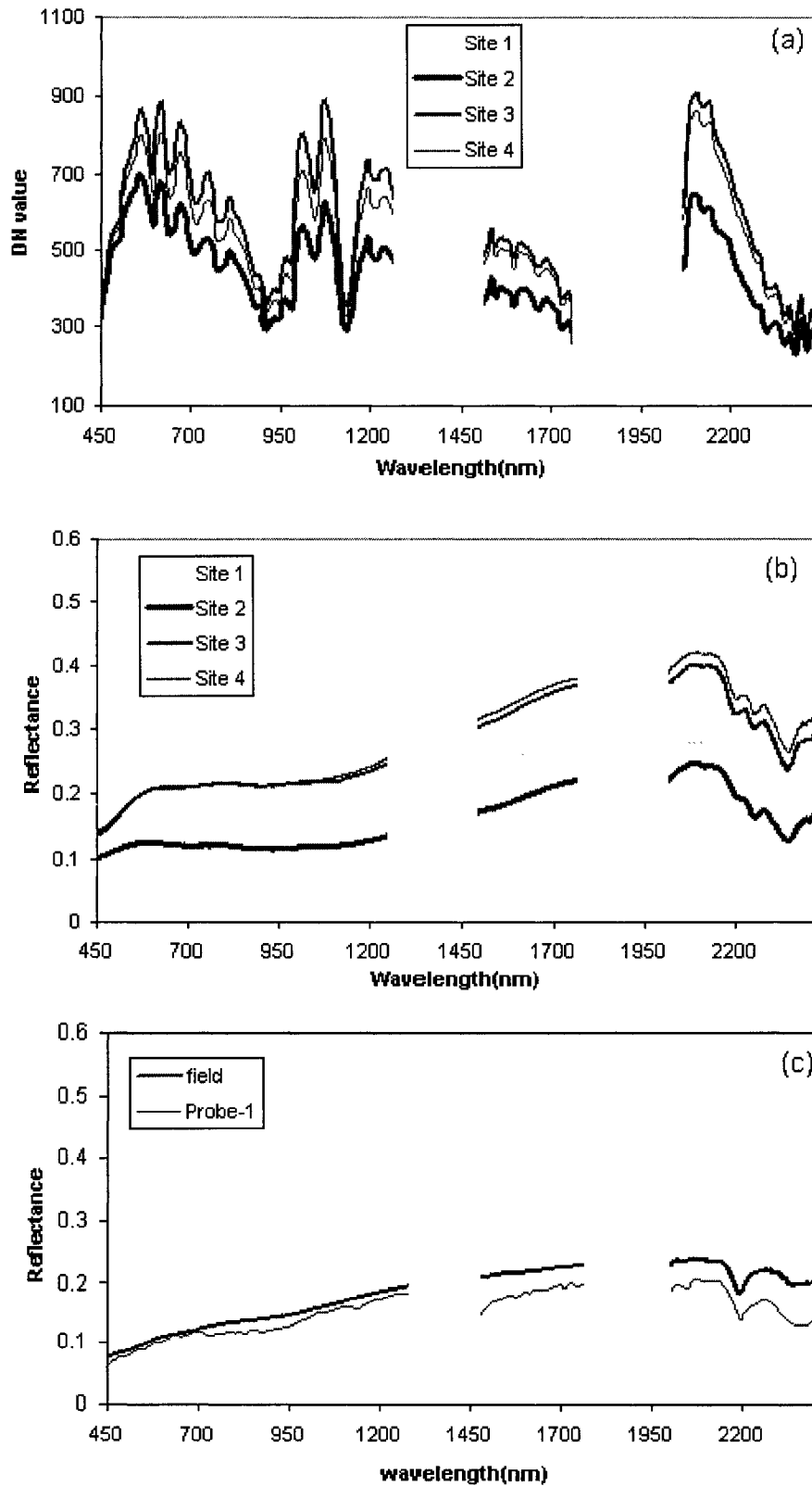


Figure 2.4. Spectra used for the calibration of the Probe-1 data. (a) Uncorrected Probe-1

data for 4 calibration sites; (b) field spectra for corresponding calibration sites; (c) comparison between corrected Probe-1 spectrum and corresponding field spectrum for a site occupied by mafic volcanic rocks. The calibrated data remain noisy at 440nm, 1304-1503nm, 1772-2050nm and 2427-2501nm, thus these bands were excluded from the analysis.

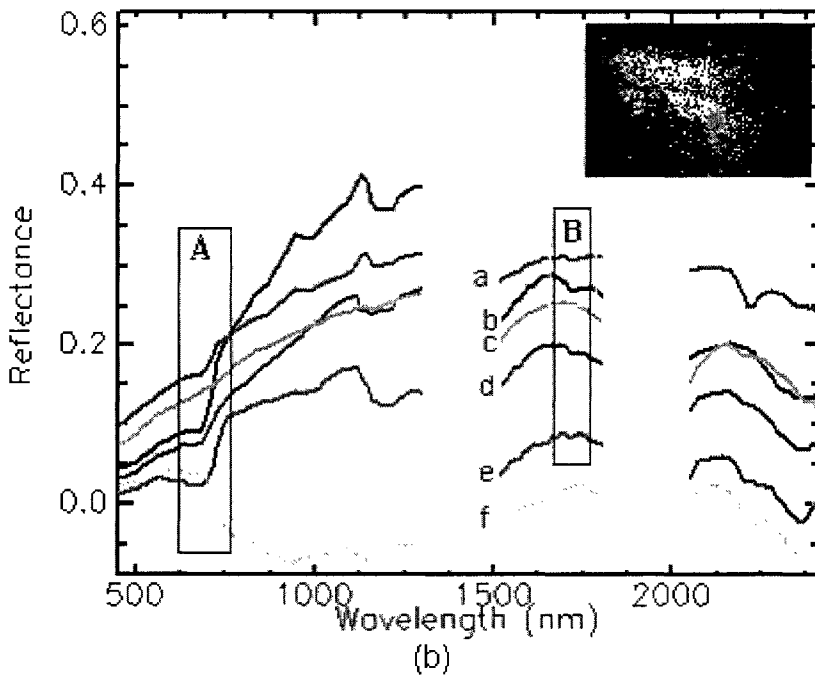
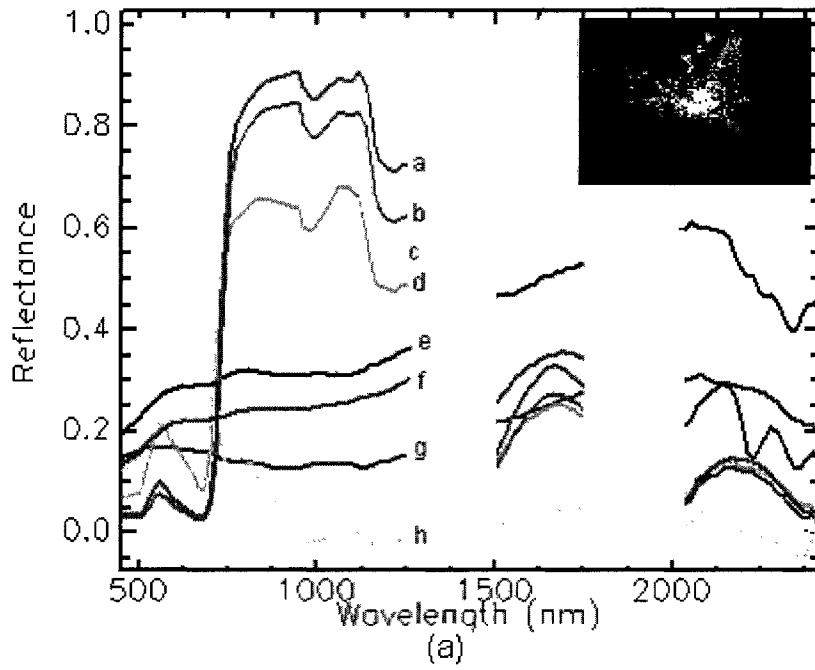


Figure 2.5. Endmember spectra extracted using the vertices of the simplex encompassing the data cloud shown in the upper right corner. Each colored cluster of pixels represents a potential endmember.

- (a): results including vegetated pixels. Labels for spectra are: a = vegetation 1, b = vegetation 2, c = vegetation 3, d = vegetation 4, e = gravel/sand 1, f = lake beach, g = shallow water, h= gravel/sand 2.
- (b): results after masking vegetated pixels. Frames A and B respectively show absorption features for chlorophyll in residual vegetation and lichen and a lichen-specific feature. Labels for spectra are: a = rhyolite+vegetation+lichen, b = rhyolite+vegetation+lichen , c = soil, d = rhyolite+vegetation+lichen , e = rhyolite+vegetation+lichen and f = water. Labeling was conducted using the geological map.

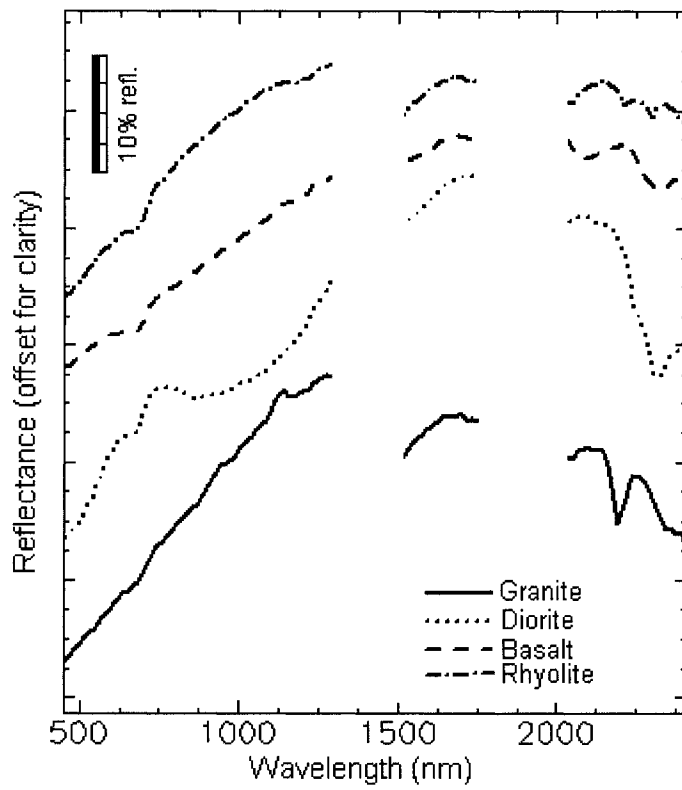


Figure 2.6. Endmember spectra used in the MTMF. Granite and rhyolite were extracted from the calibrated image cube. Diorite and basalt are average indoor or field spectra.

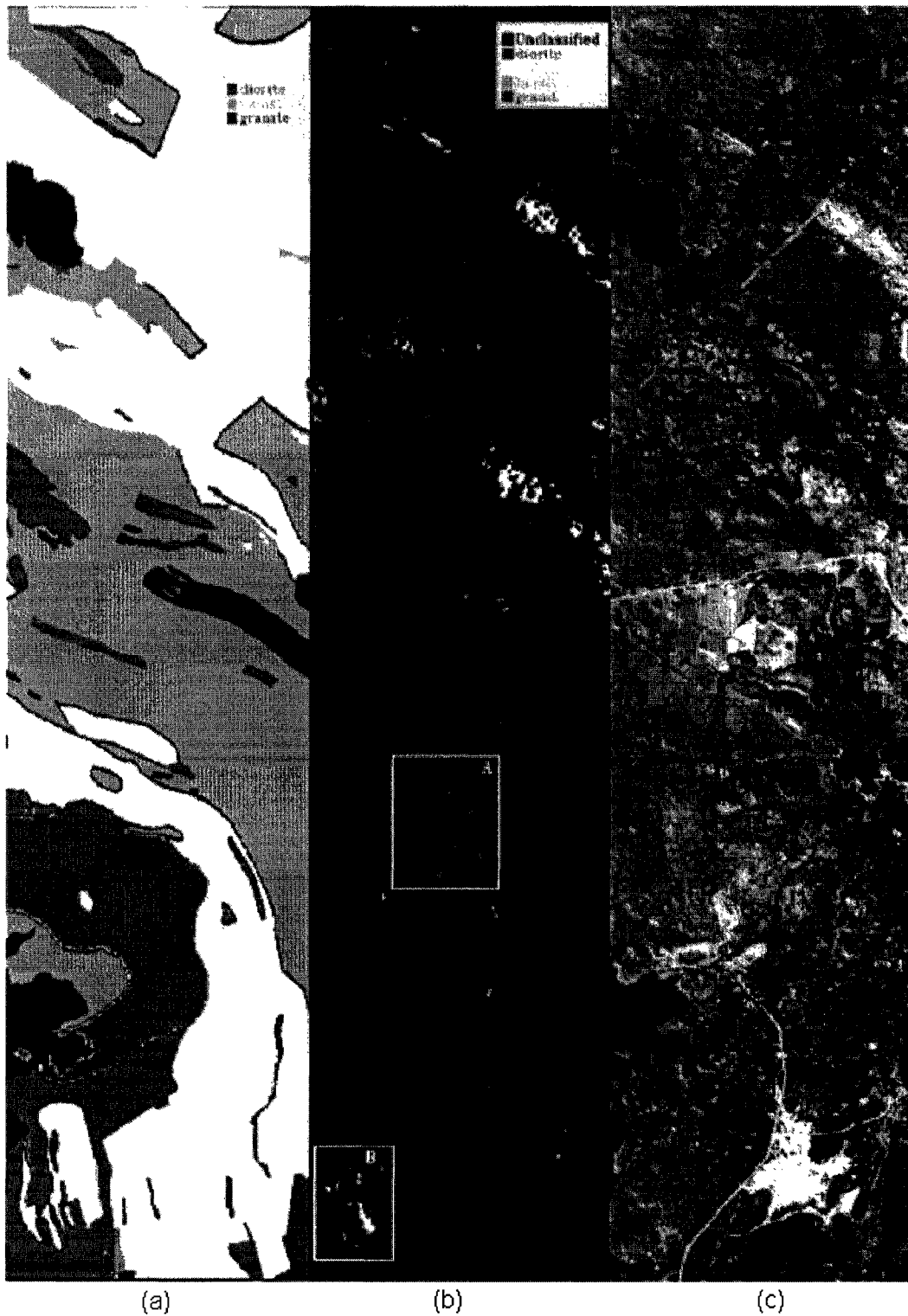


Figure 2.7. SMA results compared with geological map. (a) Geological map from Noranda inc.; (b) SMA results; (c) RGB color composite of bands at 849 nm (R), 652 nm (G), and 452nm (B). Box A: the single portion that is predicted as granite by SMA; Box

B: the region where the geological map displays diorite as the unit interspersed with rhyolite whereas the SMA predicts the occurrence of basalt.

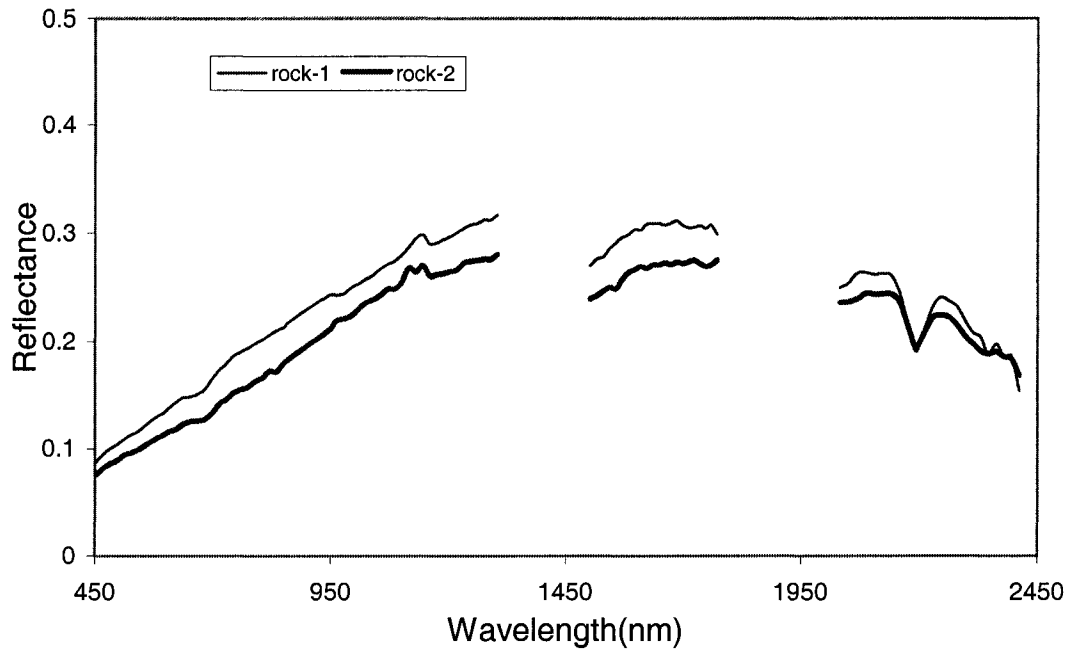


Figure 2.8. Spectra extracted from the calibrated Probe-1 data within location A (refer to Figure 2-7b). Rock-1 (thin line) was extracted from pixels labeled as granite on the geological map. Rock-2 (thick line) is for pixels labeled as rhyolite on the geological map.

CHAPTER 3

DERIVATIVE SPECTRAL UNMIXING OF HYPERSPECTRAL DATA APPLIED TO MIXTURES OF LICHEN AND ROCK

3.1 INTRODUCTION

As an integration of 'imaging' and 'spectroscopy', hyperspectral remote sensing provides researchers with the opportunity to perform the detailed identification and mapping of constituents of the earth's surface through the analysis of spectral absorption features. With the simultaneous acquisition of image data in hundreds of contiguous spectral bands, laboratory quality spectra can be constructed for each pixel in the hyperspectral image (Clark, 1999).

A challenge in the analysis of hyperspectral data is the effective use of the available spectral information. Derivative analysis of reflectance spectra has been used in hyperspectral remote sensing (Demetriades-Shah et al., 1990; Philpot, 1991; Tsai and Philpot, 2002) and in analytical chemistry (Butler and Hopkins, 1970; Huiand and Gratzl, 1996) for eliminating background signals, resolving overlapping spectral features, and enhancing spectral contrast, thereby increasing the estimation accuracy of target information. The computation of derivative spectra involves the change in a dependent variable (reflectance) relative to an independent variable (wavelength), and is sensitive to the shape rather than the magnitude of spectra. It follows that derivatives should be relatively insensitive to variations in illumination intensity caused by changes in sun angle or topography (Tsai and Philpot, 1998). First and second order derivative spectra have been applied to improve the estimation of leaf chemical constituents (Wessman,

1989; Miller and Wu, 1991), sediment in water, and water constituents (Chen et al., 1992). Few researchers have pursued the use of derivatives for hyperspectral remote mapping of rocks/minerals. Scheinost et al. (1998) used second derivative spectra to identify Fe oxide minerals in soils.

Spectral mixture analysis (SMA) has been used extensively in hyperspectral remote sensing to quantify the coverage of components at a sub pixel scale (Kruse et al., 1993; Ben-Dor and Kruse, 1995). SMA assumes that the pixel-to-pixel variability in a scene results from varying proportions of spectral endmembers. Spectral endmembers can be derived from the imagery or measurements in the laboratory/field. The spectrum of a mixed pixel can then be calculated as a linear combination of the endmember spectra weighted by the area coverage of each endmember within the pixel if the scattering and absorption of electromagnetic radiation is dominated by a single component on the surface (Singer and McCord, 1979). Fractional abundances of endmembers can be obtained for each pixel if the amplitude and shape of every endmember are known whether or not the complete suite of endmembers is of interest to the user. However, the task of defining every endmember can be difficult as evident from the importance attributed to the topic in the recent literature (Tompkins et al., 1997; Bateson et al., 2000; Okin et al., 2001; Dennison and Roberts, 2003). The effectiveness of SMA can be compromised when the required spectral endmembers are not well constrained in terms of their spectral magnitude and shape. The spectral magnitude of the endmembers is more difficult to obtain than their spectral shape, in part because the effects of the atmosphere and topography are difficult to constrain. Typically, constraining the spectral shape is

more important than the spectral magnitude because the former has a direct relationship with the composition of the target.

The integration of derivative analysis and SMA offers a way to address these problems for the following reasons.

- The derivative of a spectrum can precisely model changes in the shape of the original spectrum and is not sensitive to the spectral magnitude.
- Low frequency information is removed or reduced using derivatives.
- Computation of the derivative involves a differentiation that is a linear transform; therefore SMA can be applied to derivatives of target spectra and spectral endmembers.

This chapter presents a Derivative Spectral Unmixing (DSU) model, which is an extension of the spectral mixture analysis and derivative analysis. Using a DSU approach, it is possible to estimate the fraction of an endmember characterized by one or more diagnostic absorption features despite having only a general knowledge of the spectral shapes of the remaining endmembers. DSU may be used in many hyperspectral remote sensing scenarios as long as the spectral data has a sufficient signal to noise ratio to retain key spectral features in the derivative spectra. Section 3.2 describes the mathematical foundations of the model including that of derivative and SMA analysis. The DSU algorithm is then tested using laboratory spectral data for a natural geological sample partially coated with lichens and the estimated endmember fractional abundances (rock and lichens) are compared to known surface abundances. Section 3.3 describes the experiment conducted to generate the test data set, and Section 3.4 describes the selection

of spectral endmembers for unmixing. Finally, sections 3.5 and 3.6 present the results of the DSU and a discussion of their accuracy.

3.2 DESCRIPTION OF THE MODEL

3.2.1 Calculation of derivatives

Derivatives were estimated using a finite difference approximation (Atkinson, 1989). An advantage of the finite difference approximation is that the derivatives can be computed according to different finite band resolutions (band separations) to extract spectral features of interest at different spectral scales. The spectrum extracted from the hyperspectral data is a function of the wavelength (λ), which can be represented in discrete form as

$$s = [s(\lambda_1), s(\lambda_2), s(\lambda_3), \dots, s(\lambda_n)] \quad (3-1)$$

where s is the spectrum, and $s(\lambda_i)$ is the reflectance value at wavelength λ_i (e.g. the value at the i th band). The first derivative can be estimated to the first order accuracy ($O(\Delta\lambda)$) by

$$\left. \frac{ds}{d\lambda} \right|_i \approx \frac{s(\lambda_i) - s(\lambda_j)}{\Delta\lambda} \quad (3-2)$$

where $\left. \frac{ds}{d\lambda} \right|_i$ is the first derivative at wavelength λ_i , $\Delta\lambda$ is the separation between adjacent bands, $\Delta\lambda = \lambda_j - \lambda_i$ and $\lambda_j > \lambda_i$. Similarly, the second derivative can be approximated to the second order accuracy ($O(\Delta\lambda^2)$) by

$$\left. \frac{d^2s}{d\lambda^2} \right|_j \approx \frac{s(\lambda_i) - 2s(\lambda_j) + s(\lambda_k)}{(\Delta\lambda)^2} \quad (3-3)$$

where $\left. \frac{d^2s}{d\lambda^2} \right|_j$ is the 2nd derivative value at wavelength λ_j , $\Delta\lambda = \lambda_j - \lambda_i = \lambda_k - \lambda_j$ and $\lambda_k > \lambda_j > \lambda_i$. Accordingly, any higher order derivatives can be calculated using an iteration from the first derivative.

The choice of band separation $\Delta\lambda$ is closely related to the magnitude and resolution of the derivative spectrum and can have an important impact not only on the wavelength location of inflection points but also on that of zero-crossings. As the band separation ($\Delta\lambda$) increases, the magnitude of the spectral derivative will be depressed because the derivative is normalized by a power of $\Delta\lambda$. A large band separation can result in the loss of spectral detail and the attenuation of key spectral features. Generally, $\Delta\lambda$ should be less than the spectral feature of interest to precisely detect the absorption band. The spectral resolution of the data must also be taken into consideration. If a band separation smaller than the sensor spectral resolution is selected, artifacts may be introduced in the result. In this study, the band separation was selected to be close to the spectral resolution of the original data (5nm for the visible spectral region; 10nm for the short wave infrared spectral region).

Differentiation enhances high frequency noise while suppressing low frequency background noise and this effect is compounded as the order of the derivative increases. Although some studies have demonstrated the advantages of high order derivative spectra for the characterization of absorption features (Huguenin and Jones, 1986; Tsai and Philpot, 1998), we found that the noise levels after the second differentiation render the results difficult to interpret. Thus we used derivatives of the first and second order.

3.2.2 Noise and smoothing

The enhancement of noise caused by differentiation is largely related to high-frequency noise, the process of differentiation being effectively a form of high-pass filter. Thus, some spectral smoothing preprocessing is required prior to derivative analysis. Smoothing algorithms used in spectroscopy include the Savitzky-Golay (Savitzky and Golay, 1964), the Kawata-Minami's Linear Least Mean-Square (Kawata and Minami, 1982) and the Mean Filter (Tsai and Philpot, 1998). When the noise is at a high frequency with respect to the spectral features of interest, as is the case in this study, there should be little significant differences between the three methods (Tsai and Philpot, 1998). The Mean Filter smoothing algorithm was used in this study because it is straightforward and requires the least computation time. A Mean Filter locally smoothes the data within a predetermined moving window by calculating the mean value of samples which is then attributed to the middle sampling point of the smoothing window. The algorithm can be represented as

$$\hat{s}(\lambda_j) = \frac{\sum_{i=1}^n s(\lambda_i)}{n}, \quad (3-4)$$

where n (number of sampling points) is the size of the filter, and j is the index of the midpoint. $\hat{s}(\lambda_j)$ is the new value of the midpoint in the window. The larger the filter window, the smoother the result, and the more likely the loss of useful detailed spectral information. Excessive smoothing can introduce artifacts in the form of band distortion and changes in the location of the center of the absorption feature (Kawata and Minami, 1982). In this study, the filter size was gradually increased until relatively smooth

derivative spectra were obtained. A filter size of 7 was selected because larger sizes resulted in loss of spectral details in the 2nd derivative spectra.

3.2.3 Derivative Spectral Unmixing (DSU)

A classical approach to solve the mixed pixel problem is the linear unmixing model, which assumes that the materials (endmembers) present in a pixel are linearly mixed. The mixed pixel spectrum can be described by

$$s_m(\lambda) = \sum_{i=1}^k f_i sp_i(\lambda), \quad (3-5)$$

$$0 \leq f_i \leq 1.0, \sum_{i=1}^k f_i = 1.0 \quad (3-6)$$

where $s_m(\lambda)$ is the spectrum of the mixture, $sp_i(\lambda)$ is the i th endmember spectrum, f_i is the abundance fraction of i th endmember in the mixture, and k is the total number of endmembers needed to model accurately the mixture spectrum.

If the original spectrum can be modeled as a linear combination of all endmembers, its derivative will also conform to the linear mixing model. In the derivative spectral domain the linear mixing model can be expressed as

$$\frac{d^n s_m(\lambda)}{d\lambda^n} = \sum_{i=1}^k \left(f_i \frac{d^n sp_i(\lambda)}{d\lambda^n} \right), \quad (3-7)$$

$$0 \leq f_i \leq 1.0, \sum_{i=1}^k f_i = 1.0, \quad (3-8)$$

where $\frac{d^n s_m(\lambda)}{d\lambda^n}$ is the n th derivative of the spectrum of the mixed pixel, $\frac{d^n sp_i(\lambda)}{d\lambda^n}$ is the n th derivative of the i th endmember spectrum ($sp_i(\lambda)$), f_i is the abundance fraction of the i th endmember in the mixture and k is the total number of endmembers. The

derivative mixing model has the same form as the reflectance/radiance mixing model with the distinction that derivatives are used for both the mixture and endmember spectra.

If equation (3-7) is rewritten to isolate the abundance of a single endmember (k th endmember):

$$f_k = \frac{\frac{d^n s_m(\lambda)}{d\lambda^n} - \sum_{i=1}^{k-1} (f_i \frac{d^n sp_i(\lambda)}{d\lambda^n})}{\frac{d^n sp_k(\lambda)}{d\lambda^n}} \quad (3-9)$$

and $SUM_{Non_interest} = \sum_{i=1}^{k-1} (f_i \frac{d^n sp_i(\lambda)}{d\lambda^n})$, (3-10)

then

$$f_k = \frac{\frac{d^n s_m(\lambda)}{d\lambda^n} - SUM_{Non_interest}}{\frac{d^n sp_k(\lambda)}{d\lambda^n}} . \quad (3-11)$$

With a good approximation of $SUM_{Non_interest}$, the fraction f_k of the endmember of interest can be derived.

Here we define a key property of derivatives that applies to spectra of a variety of natural targets and which enables a simplification of (3-11). As an example we focus our discussion on geological targets. The spectra of most minerals are complicated functions of the wavelength (λ) in the visible (VIS), near infrared (NIR), and short wave infrared (SWIR) spectral region, but the spectra can be approximated as a simple linear function (Equation (3-12)) within specific spectral region (e.g. $[\lambda_1, \lambda_2]$) free of spectral features

$$s = a\lambda + c , \quad (3-12)$$

where a and c are regression coefficients, λ is the wavelength, $\lambda \in [\lambda_1, \lambda_2]$. The second derivative values for such spectral segment will be

$$\frac{d^2 s}{d\lambda^2} = 0, \lambda \in [\lambda_1, \lambda_2]. \quad (3-13)$$

Thus if an endmember spectrum can be characterized by (3-12) in a specific wavelength region, the contribution of this endmember to the second derivative spectrum of the mixture will be zero in this spectral region. Consequently the mixing model will require one less endmember if derivative spectra are analyzed as opposed to reflectance spectra.

Many minerals have absorption features distinct from surrounding rock forming minerals (Hunt, 1977) and those of non-geological targets (e.g. vegetation). Therefore it is commonly feasible to determine a spectral region $[\lambda_1, \lambda_2]$ where a mineral endmember of interest has a distinct absorption band and where remaining endmembers in the mixture have a spectral shape that can be modeled by equation (3-12). In such instance, the solution for endmember f_k characterized by the unique spectral feature can be simplified (compare with equation (3-11)) as

$$f_k \approx \frac{\frac{d^2 s_m(\lambda)}{d\lambda^2}}{\frac{d^2 s p_k(\lambda)}{d\lambda^2}} \quad \lambda \in [\lambda_1, \lambda_2], \quad (3-14)$$

using the second derivatives since $SUM_{Non_interest} = 0$. The fraction of endmember, f_k , is easily estimated using the 2nd derivative spectra of the mixture and of the endmember of interest.

For a mixture of more than 2 endmembers, it may be necessary to use more than one spectral region to calculate the fractions of multiple endmembers of interest. If an endmember of interest has a distinct spectral feature that does not overlap with that of the remaining endmembers in the mixture, equation (3-14) can be used to calculate the fractional abundance of this endmember.

3.3 EXPERIMENT

The DSU algorithm was tested using spectral measurements of a geological surface coated with rock encrusting lichens. The rock sample (Figure 3.1) was collected in June 1999 from the Gog Quartzite Formation in Jasper, Alberta, Canada (52°12'N, 117°15'W). The sample comprises three surface types, namely green lichen (*R. geographicum*), black lichen (*R. bolanderi*) and the rock substrate (*quartzite*). The quartzite substrate is ideal to test the abundance predictions of the DSU because it provides uniformly high reflectance and, as discussed in section 3-4, mineral absorption features that are well understood and discernable from that of lichen. The spectral measurements were taken in the laboratory using a FieldSpec FR spectroradiometer that operates in the 350-2500 nm spectral range and is characterized by a spectral resolution of 3 nm at 700 nm, 10 nm at 1500 nm, and 10 nm at 2100 nm (Analytical Spectral Devices, 2001). Measurements were recorded as reflectance (as opposed to radiance) using an average of twenty scans in order to minimize instrument noise. A field of view (FOV) of 0.45 cm in diameter was achieved by bringing a fiber optic (FOV 25 °) into a position normal to the surface within 1 cm of the sample. The sample was illuminated with one quartz halogen lamp at an incident angle of 30 degrees. Reflectance spectra were obtained by determining the ratios

of data acquired for a measurement of the sample to data acquired for the 99% reflectance Spectralon panel under the same illumination and observation conditions. To generate a data set with variable abundance of green lichen, black lichen, and rock, the rock sample surface was measured following a constant grid increment of 0.45 cm along two orthogonal directions (Figure 3.1b). Finally the spectral measurements were arranged as an image cube in accordance to their physical alignment in the grid (Figure 3.1c).

To assess the accuracy of the predictions from the DSU analysis, a digital photo of the sample was registered to the spectral cube and used to estimate the abundances of lichen and rock within each spectral pixel. Each spectral pixel is encompassed by 100 pixels of the digital photo. The spatial resolution of the photo implies that a single surface type characterizes most pixels. A supervised maximum likelihood classification was used to assign each photo pixel to one of 3 endmember surface types (green lichen, black lichen and rock). Grids of 0.45cm by 0.45cm (one grid cell corresponding to one spectral measurement) were overlaid on the registered rock photo, and the endmember fraction within each spectra pixel was automatically estimated by counting the total number of pixels that belong to a given surface type on the photo.

3.4 SELECTION OF ENDMEMBERS

Bechtel et al. (2002) have shown that rock-encrusting lichens transmit very little light (<3%) from 350-2500 nm. These findings support the use of linear mixture models for the deconvolution of lichen/rock mixtures. Black crustose lichens display a reflectance less than 7% in the visible range (Figure 3.2). *R. geographicum* is a mosaic

of tiny green 'tiles' (areoles) set against a distinctly black background (Johnson et al., 1985). The green appearance of this lichen comes from the presence of these areoles, not from the lichen thallus itself (Bechtel et al., 2002). The reflectance is near 5% at 400 nm and quickly rises to approximately 11-17% from 520 nm until the chlorophyll absorption near 685 nm (box A on Figure 3.2). *R. geographicum* shows a green peak at approximately 550 nm that is more characteristic of vascular plants than some of the darker colored lichens. Both lichens display a gradual increase in reflectance to 1380 nm followed by an absorption feature centered near 1445 nm caused by water in the lichen. The spectra then display an increase in reflectance reaching a maximum value around 1860 nm. Beyond the water absorption feature near 1935 nm (masked on figure 2) the spectra of both lichens are similar in shape. The same observations were reported by Bechtel et al. (2002) for a wider range of lichen species.

Ager and Milton (1987) identified three broad absorption features near 1730, 2100, and 2300 nm, which are attributable to the presence of cellulose in lichen (Figure 3.2). A broad feature near 2355 nm is present in lichens (Bechtel et al., 2002); however, this feature also appears in the quartzite spectra, so this feature cannot be uniquely associated with lichen. The quartzite spectrum is characterized by a distinct absorption band at 2195nm (Box B on Figure 3.2) when compared to the lichens. The lichens display a similar and nearly linear spectral shape near 2195nm and thus their second derivative values are close to zero near this wavelength (Figure 3.3). Green and black lichen can be distinguished based on the unique absorption feature of green lichen near 680nm due to the presence of chlorophyll (Box A in Figure 3.2). In this wavelength region rock and black lichen display second derivative values approaching zero (Figure 3.

3). Based on the observation above, equations (3-15) and (3-16) can provide an estimation of the rock and green lichen abundances:

$$f_{rock_estimate} \approx \frac{\left. \frac{d^2 s_m}{d\lambda^2} \right|_{2195nm}}{\left. \frac{d^2 s_{rock}}{d\lambda^2} \right|_{2195nm}}, \quad (3-15)$$

$$f_{green_estimate} \approx \frac{\left. \frac{d^2 s_m}{d\lambda^2} \right|_{680nm}}{\left. \frac{d^2 s_{green}}{d\lambda^2} \right|_{680nm}}. \quad (3-16)$$

The DSU algorithm requires the selection of one spectrum for each class that is unmixed, in this case green lichen and quartzite. For this purpose spectral pixels were selected from large surface areas identified from the digital photo and containing one surface type (pure pixels). Figure 3.4 provides the mean, minimum, maximum and standard deviation (STD) of the second derivative values for each class. Black lichen was included for comparison. Each of these natural surfaces spans a range of values and the two pixels with the maximum 2nd derivative values at 680 nm and 2195 nm were selected as endmember spectra for green lichen and rock respectively (also shown on Figs 3-2 and 3-3).

3.5 RESULTS

The abundances of green lichen and rock in each pixel were estimated using Eq. (3-15) and (3-16) and compared to the “true values” obtained from the analysis of the high-resolution digital photo (Figure 3. 5). The correlations between the two data sets were examined using ordinary least squares (OLS) at a confidence interval of 95%. Because the data are expected to show a linear correlation, a parametric regression test was used rather than a non-parametric approach. For green lichen, $f_{green_estimate} = 0.9672 * f_{green_truth} + 0.023$ and $R^2 = 0.9403$. For quartzite $f_{rock_estimate} = 0.9377 * f_{rock_truth} + 0.0358$ and $R^2 = 0.9260$. Although the estimated values for both surface types are a little smaller than the true values (slope < 1), a significant linear correlation exists between the two data sets (p value = 0) (Figure 3.5). The distribution of the absolute errors between the estimated and true abundances is illustrated in Figure 3.6. For green lichen, 70% of the pixels have an error within -0.01 and 0.05, and 90% of the pixels have an error between -0.05 and 0.12. For rock, 70% of the pixels have an error within -0.08 and 0.07, and 90% of the pixels have an error between -0.13 and 0.18. For “true values” approaching 0% or 100%, the estimated abundances tend to cluster (Figure 3.5, circles a, b, c and d). The errors illustrate the natural spectral variability of the endmember surfaces, a factor that is not accounted for by DSU where a single spectrum per endmember is used.

3.6 DISCUSSION

The results of our laboratory experiment suggest that DSU is a promising approach to derive sub-pixel abundances. To illustrate the premise of the model we chose to

calculate abundances of green lichen and rock because they display documented absorption features that are not shared by other scene components. The computation of rock/mineral abundance is relevant to the analysis of hyperspectral imagery in geology. In practice geologists would likely group all lichens as a single spectral endmember. By focusing on a spectral region unique to lichens (e.g. 1730 nm) where rock/minerals lack spectral contrast (Bechtel et al., 2002), the DSU could be used to determine the total lichen coverage within each pixel of a hyperspectral image. (Appendix 1 presents some related research results.)

By choosing endmembers with maximum 2nd derivative values, we introduced a bias towards the underestimation of true abundances. In addition, an underlying assumption of the model is that endmembers other than the one of interest have null 2nd derivative values at the wavelength used for the DSU. Figure 3.3 and 3.4 indicate that this is not true in this experiment and will likely not be true for other natural targets, thereby contributing errors. Future work will apply the DSU to airborne/spaceborne hyperspectral imagery. The signal to noise ratio (SNR) of imaging hyperspectral data (e.g. HYMAP, HYDICE) is lower than that of our laboratory data, thus the separation of useful signal from noise will be a very important factor in determining the usefulness of the DSU for mineral mapping.

3.7 CONCLUSIONS

This chapter combines spectral mixture analysis and derivative spectra to present a new unmixing model termed the “derivative spectral unmixing”. The key strength of this concept is that the abundance estimation of endmembers does not require a thorough

knowledge of all endmembers at hand as long as the unknowns do not display conflicting absorptions features with that of the material of interest. The DSU results for our laboratory experiment shows that the algorithm is promising for the quantitative analysis of hyperspectral data. The experiment in this chapter demonstrates that bias in the selection of the endmembers can introduce errors in the final abundance estimation. Several improvements and extensions to the algorithm may be the focus of future research. The incorporation of the intra-class variation into the DSU model should improve the accuracy of the results. The example in this chapter made use of only one band per endmember class for the abundance estimation. The use of multiple diagnostic bands per endmember may improve the estimated fractions.

ACKNOWLEDGMENTS

This research was funded by grants from the Geoid Canadian Network Centres of Excellence, the Canada Foundation for Innovation and the National Science and Engineering Research Council of Canada.

REFERENCES

- Ager, C. M., and Milton, N. M., 1987, Spectral reflectance of lichens and their effects on the reflectance of rock substrates. *Geophysics*, v. 52, p. 898-906.
- Analytical Spectral Devices, www.asdi.com, 5335 Sterling Drive, Suite A, Boulder, CO 80301, 2001.
- Atkinson, K.E., 1989, *An Introduction to Numerical Analysis*, Second Edition, John Wiley and Sons: New York.

- Bateson, C. A., Asner, G. P. and Wessman, C. A., 2000, Endmember Bundles: A New Approach to Incorporating Endmember Variability into Spectral Mixture Analysis, *IEEE Transactions on Geoscience and Remote Sensing*, v. 38, p. 1083-1094.
- Bechtel, R., Rivard, B. and Sanchez, A., 2002, Spectral properties of foliose and crustose lichens based on laboratory experiments, *Remote Sensing of Environment*, v. 82, p. 389-396.
- Ben-Dor, E. and Kruse, F. A., 1995, Surface mineral mapping of Makhtesh Ramon Negev, Israel using GER 63 channel scanner data, *International Journal of Remote Sensing*, v. 16, p. 3529-3553.
- Butler W. L. and Hopkins, D. W., 1970, Higher derivative analysis of complex absorption spectra, *Photochemistry and Photobiology*, v. 12, p. 439-450.
- Chen, Z., Curran P. J. and Hansom, J.D., 1992, Derivative reflectance spectroscopy to estimate suspended sediment concentration, *Remote Sensing of Environment*, v. 40, p. 67-77.
- Clark, R.N., 1999, Spectroscopy of Rocks and Minerals, and Principles of Spectroscopy, Available: <http://speclab.cr.usgs.gov/PAPERS.refl-mrs/refl4.html>
- Demetriades-Shah, T. H., Stevenand M. D. and Clark, J. A., 1990, High resolution derivatives spectra in remote sensing, *Remote Sensing of Environment*, v. 33, p. 55-64.
- Dennison, P. E. and Roberts, D. A., 2003, Endmember selection for multiple endmember spectral mixture analysis using endmember average RMSE, *Remote Sensing of Environment*, v. 87, p. 123-135.

- Huguenin R. L. and Jones, J. L., 1986, Intelligent information extraction from reflectance spectra: Absorption band positions, *Journal of Geophysical Research*, v. 91, p. 9585-9598.
- Huiand K. and Gratzl, M., 1996, Anomalies of convolutional smoothing and differentiation, *Analytical Chemistry*, v. 68, p. 1054-1057.
- Hunt, G. R., 1977, Spectral signatures of particulate minerals in the visible and near infrared, *Geophysics*, v. 42, p. 501-513.
- Johnson, D., Kershaw, L., MacKinnon, A. and Pojar, J., 1985, *Plants of the Western Boreal Forest and Aspen Parkland*, Edmonton, Canada: Lone Pine Publishing.
- Kawata, S. and Minami, S., 1982, Adaptive smoothing of spectroscopic data by a linear mean- square estimation, *Applied Spectroscopy*, v. 38, p. 49-58.
- Kruse, F.A., Lefkoff, A.B. and Dietz, J.B., 1993, Expert system based mineral mapping in northern Death Valley, California/Nevada using the airborne visible/infrared imaging spectrometer (AVIRIS), *Remote Sensing of Environment*, v. 44, p. 309-335.
- Miller J. R. and Wu, J., 1991, Seasonal patterns in leaf reflectance red edge characteristics, *International Journal of Remote Sensing*, v. 12, p. 1509-1523.
- Okin, G.S., Roberts, D.A., Murray, B. and Okin, W.J., 2001, Practical limits on hyperspectral vegetation discrimination in arid and semiarid environments, *Remote Sensing of Environment*, v. 77, p. 212-225.
- Philpot, W. D., 1991, The Derivative Ratio Algorithm: Avoiding Atmospheric Effects in Remote Sensing, *IEEE Transactions on Geoscience and Remote Sensing*, v. 29, p. 350- 357.

- Savitzky A. and Golay, M. J., 1964, Smoothing and differentiation of data by simplified least squares procedures, *Analytical Chemistry*, v. 36, p. 1627-1639.
- Scheinost, A. C., Chavernas, A., Barrón V. and Torrent, J., 1998, Use and limitations of second-derivative diffuse reflectance spectroscopy in the visible to near-infrared range to identify and quantify Fe oxide minerals in soils, *Clays and Clay Minerals*, v. 46, p. 528-536.
- Singer. R.B. and McCord, T. B., 1979, Mars: Large Scale Mixing of Bright and Dark Surface Materials and Implications for Analysis of Spectral Reflectance, *Proceeding of the 10th Lunar and Planetary Science Conference*, p.1835-1848.
- Tompkins, S., Mustard, J. F., Pieters, C. M. and Forsyth, D. W., 1997, Optimization of endmembers for spectral mixture analysis, *Remote Sensing of Environment*, v.59, p.472-489.
- Tsai, F. and Philpot, W. D., 1998, Derivative Analysis of Hyperspectral Data, *Remote Sensing of Environment*, v. 66, p. 41-51.
- Tsai, F. and Philpot, W. D., 2002, A derivative-aided hyperspectral image Analysis System for land-cover classification, *IEEE Transactions on Geoscience and Remote Sensing*, v. 40, p. 416-425.
- Wessman, C. A., 1989, An evaluation of Imaging Spectrometry for Estimating Forest Canopy Chemistry, *International Journal of Remote Sensing*, v. 10, p. 1293-1316.

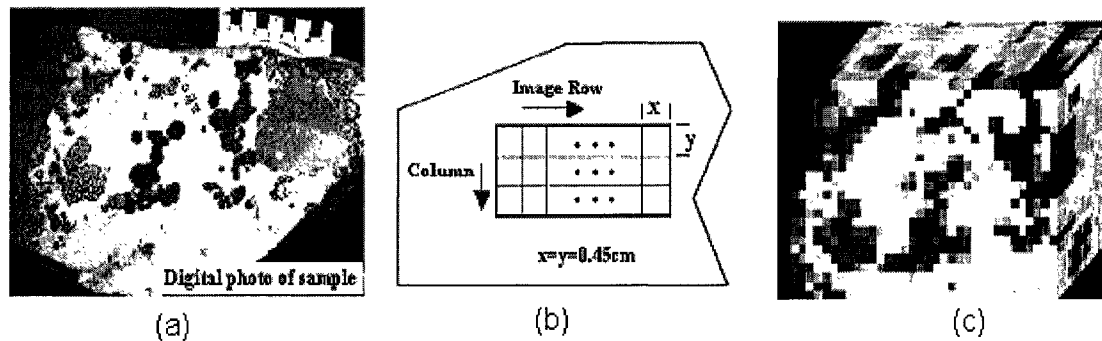


Figure 3.1 Photograph of the lichen encrusted quartzite sample and resulting hyperspectral data cube. (a) Digital photo of rock sample showing green lichen (*R. geographicum*) and black lichen (*R. bolanderi*) and the red cross marks used for coregistration with the spectral data; (b) schematic diagram of the spectral measurement layout. Each cell (0.45 cm by 0.45cm) is corresponding to one spectral measurement; the sample is translated through the field of view of the instrument along two directions (showed by the two arrows), that correspond to the image rows and columns in (c); (c) Hyperspectral image cube generated according to the measurement layout illustrated in (b). This is a three dimensional view of the spectral data. The front face is a color composite of bands 430nm (Blue), 550nm (Green) and 710nm (Red). The top and side faces of the cube are colored to show the reflectance variation with wavelength of pixels in the first row and last column (red means high value).

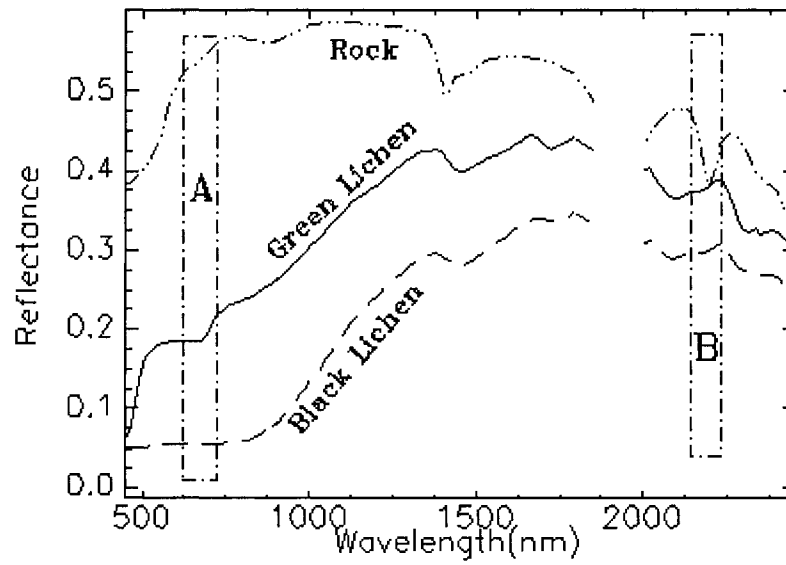


Figure 3.2 Endmember spectra for green lichen, black lichen and rock. The selection of the spectra is detailed in section 3.4. The strong water absorption feature near 1900 nm was discarded because of low signal. Box A marks the 680nm region where green lichen has a unique absorption feature. Box B marks the 2195nm region where quartzite has a diagnostic absorption feature.

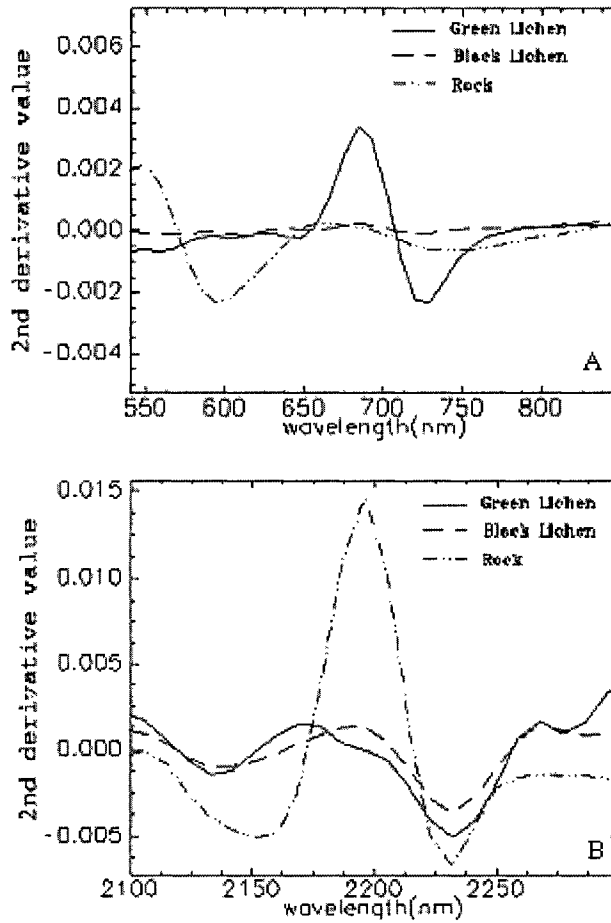


Figure 3.3 2nd derivative endmember spectra for quartzite, green lichen and black lichen at 680 nm (A) and 2195 nm (B). Quartzite has an overwhelming 2nd derivative value compared to green and black lichen at 2195nm while green lichen has distinct values near 680nm.

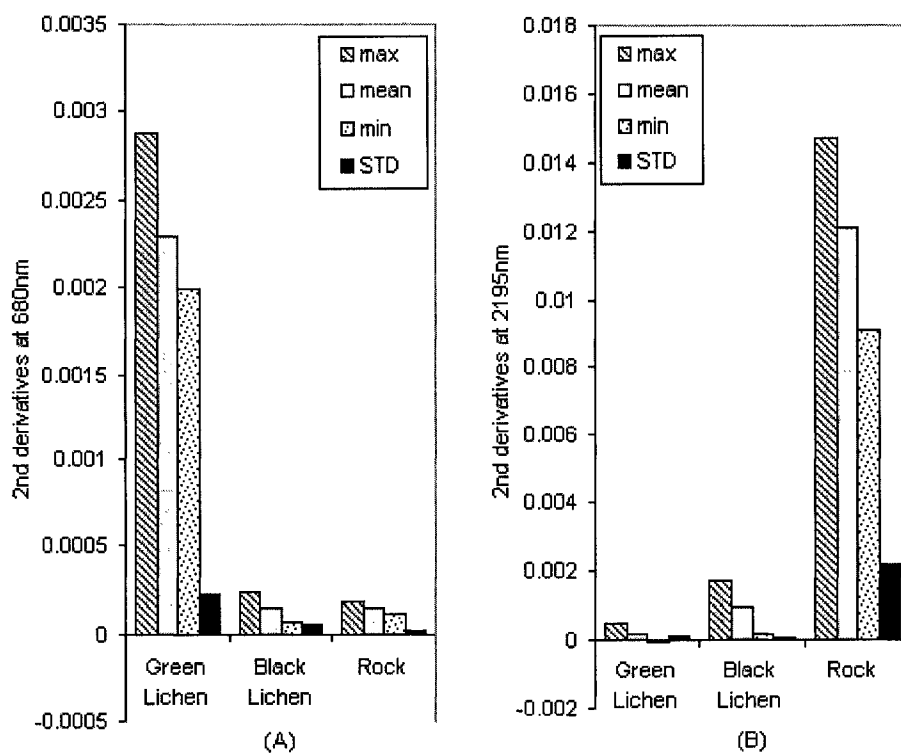


Figure 3.4 Mean, minimum, maximum, and standard deviation (STD) of 2nd derivative values at 680 nm (A) and 2195 nm (B) for locations of the sample with green lichen, black lichen and quartzite (rock).

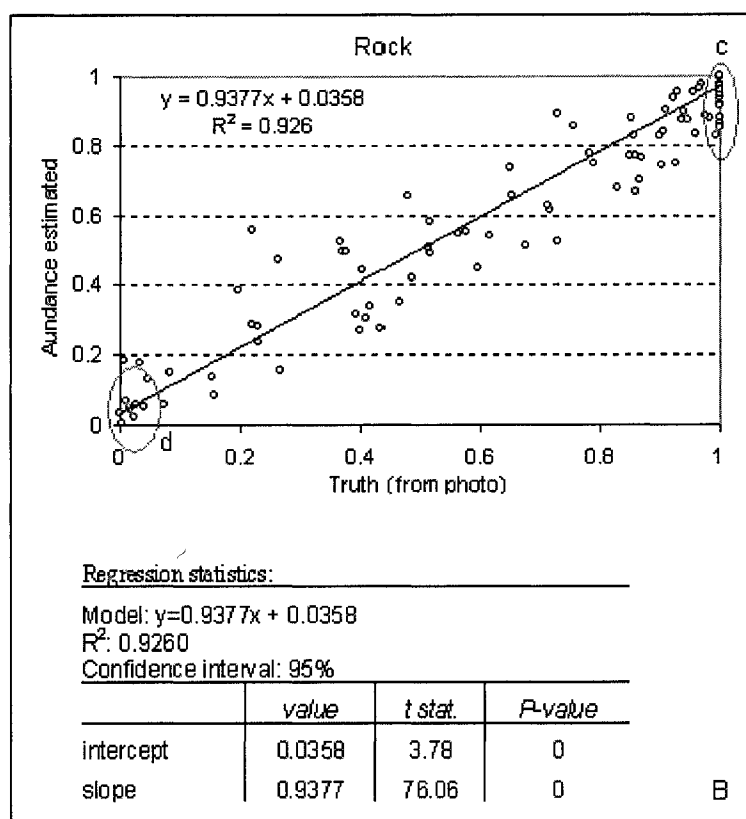
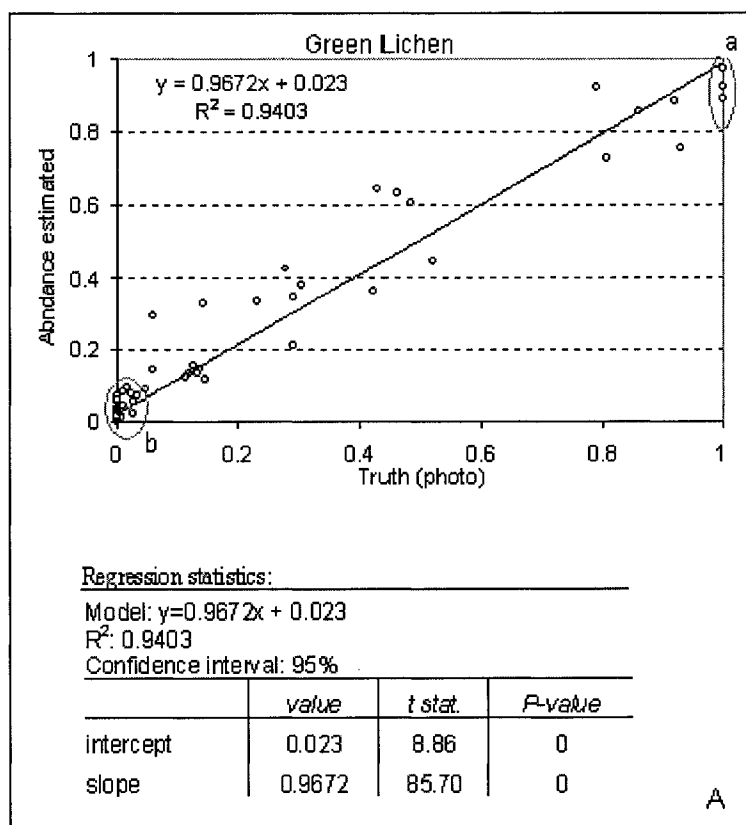


Figure 3.5 Comparison between the abundances of green lichen (A) and quartzite (B)

estimated using the DSU and “true” abundances observed from the digital photo. In both instances, the linear correlation has a slope <1 indicating that the DSU underestimates the true abundances. The circled areas show that data points tend to cluster when “true values” are approaching 0% or 100%, which reflects the natural variability of endmember surfaces that is not accounted for by DSU.

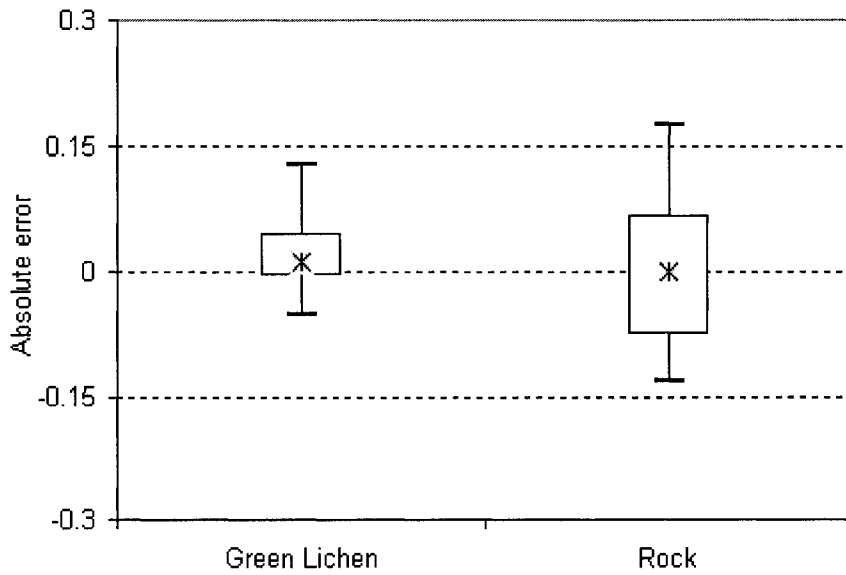


Figure 3.6 Distribution of the absolute errors of the estimated abundances for green lichen and rock. The error was calculated by subtracting the estimated abundance from the true abundance. The “X” symbol marks the median value for all the pixels; the box is for 15% and 85% percentile; whiskers for 5% and 95% percentile.

CHAPTER 4

SPECTRAL UNMIXING OF NORMALIZED REFLECTANCE DATA FOR THE DECONVOLUTION OF LICHEN AND ROCK MIXTURES

4.1. INTRODUCTION

Hyperspectral remote sensing systems are becoming increasingly available for regional geological mapping and mineral exploration where cost saving measures are key to commercial competitiveness (Kruse, 1999; Staenz et al., 1998). The mixture of several materials within individual pixels can complicate the analysis of multispectral and hyperspectral information, often masking the diagnostic spectral features of materials of interest and hampering their classification. A widespread example of this problem in high latitude, subarctic regions is the ubiquitous presence of rock encrusting lichens that may compromise the ability to map the reflectance signatures of minerals from imaging spectrometer data (Rivard and Arvidson, 1992). In tundra and open woodland habitats, lichens and mosses can cover an area by as much as 70% (Solheim et al., 2000), complicating comprehensive mapping exercises aimed at resource extraction. Fortunately, the use of spectral mixture analysis (SMA; Mustard and Sunshine, 1999; Smith et al., 1990) addresses the complexity of target identification within mixed pixels and can allow detection of substances exposed at subpixel resolution. Typically this approach assumes that mixed spectra result from the linear combination of spectral end-members (Singer and McCord, 1979).

The determination of lichen transmittance is the key issue in assessing the assumption that satellite reflectance measurements of lichen encrusted bedrock represent

mixtures of lichen and rock reflectance linearly weighted by their respective surface cover. Bechtel et al. (2002) estimated lichen transmittance to be <3% throughout the 350–2500 nm spectral region, using spectra measured from the foliose lichen *U. torrefacta* as a representative sample of a broader class of rock encrusting lichens. These findings suggest that the optical thickness of lichen largely prevents the transmission of light through the lichen mat to the underlying rock substrate. Using the band ratios 2132/2198 and 2232/2198 nm for five crustose lichen species (*U. torrefacta*, *R. bolanderi*, *R. geminatum*, *R. geographicum*, *A. cinerea*), Bechtel et al. (2002) also showed the similarity in shape of various lichen spectra in the short wave infrared (SWIR) spectral region supporting similar observations by Rivard and Arvidson (1992). These results imply that the mixing of lichen and rock spectra within a scene should be linear, and that spectral unmixing of rock and crustose/foliose lichens may be successfully accomplished using a single lichen end-member for this spectral range.

The incorporation of lichen endmember spectra into SMA presents new challenges, which will be addressed in this chapter. In SMA, the spectra of end-members are either extracted from the imagery or measured in the laboratory or in the field. Given that rock-encrusting lichens rarely fill a pixel (they are usually found in round patches on rocks in the field), it is not feasible to determine lichen endmember spectra from imagery. One must rely on field or laboratory measurements of varying species of lichens to define one or more lichen endmember spectra.

Differences in viewing and illumination geometry between field/laboratory spectra and imagery will result in spectral reflectance differences that introduce errors in SMA results. This study builds on the conclusions of Bechtel et al. (2002) and examines

the use of spectral normalization to minimize differences in SWIR reflectance of five lichen species and determine an optimal number of lichen endmember spectra for SMA. The findings are then applied to the SMA of an image generated in the laboratory for a lichen encrusted rock sample. Finally the unmixed abundances are correlated with lichen and rock abundances obtained from a high-resolution photograph and the implications of the results for the analysis of airborne/spaceborne hyperspectral imagery are discussed.

4.2 MATERIAL AND METHODS

4.2.1 Data acquisition

In this chapter we first examine the variability in spectral shape across lichen species making use of spectral data collected by Bechtel et al. (2002) for lichen bearing rocks sampled from the Gog Quartzite Formation in Jasper, Alberta, Canada (52°12'N, 117°15'W). Twenty-seven lichen bearing rock samples were collected and measured within a 2-week period to ensure a healthy condition of the lichens. Reflectance spectra were acquired from five different locations on each of the seventeen lichen patches under dry conditions, comprising a total of five different species (*U. torrefacta*, *R. bolanderi*, *R. geminatum*, *R. geographicum*, *A. cinerea*). The relevant measurement methodology is described by Bechtel et al. (2002). The quartzite substrate provides uniformly high reflectance and mineral absorption features that are well understood and discernable from those of lichen. The quartzite samples are compositionally homogenous and, therefore, show little spectral variation within sample and between samples.

To perform the SMA, a hyperspectral image was generated in the laboratory for one rock sample that comprises three surface types, namely green lichen (*R. geminatum*),

black lichen (*R. bolanderi*) and the rock substrate (*Quartzite*) (Figure 4.1a). The spectral data were acquired with an ASD FieldSpec FR portable spectroradiometer that operates in the spectral region between 350 and 2500nm, with a spectral resolution of 3nm at 700nm, 10nm at 1500nm, and 10nm at 2100nm (Analytical Spectral Devices, 2001). Spectral measurements were collected using a fiber optic (FOV 25°) along the normal direction to the surface at a distance of 1 cm, which results in a spatial resolution of 0.45cm (illuminated footprint on the surface). The sample was illuminated with one quartz halogen lamp (50W) at an incident angle of 30 degrees. The reflectance spectrum was obtained by calculating the ratio of the radiance of the sample to the radiance of a 99% reflective reference panel (Spectralon, Labsphere, North Sutton, NH, USA) under the same illumination and viewing conditions. The spectrum recorded for each surface location is an average of 20 scans, resulting in an increase of 4.5 times in the signal to noise ratio (SNR). A flexible sample platform was used to hold and move the rock while preserving the viewing geometry for all measurements. The sample surface was scanned with a constant grid increment (0.45cm) along two orthogonal directions, thus capturing the local abundance variations of three endmembers (surface types) within each measurement (Figure 4.1b). The spectra varied significantly from spot to spot because some of the grid positions were fully occupied by lichens while some were filled with the rock substrate. Finally all spectral measurements were arranged as an image in accordance to their physical alignment in the grid (Figure 4.1c).

To assess the SMA results, a high resolution digital photo of the sample was co-registered to the hyperspectral image cube and used to estimate the abundances of lichen and rock within each spectral pixel (Figure 4.1a). Each spectral pixel (corresponding to

an area of 0.45 cm by 0.45 cm on the rock surface) contains approximately 100 pixels in the digital photo. Thus one pixel on the digital photo equals approximately 0.045cm by 0.045cm, which implies that most pixels will consist of a single surface type. A supervised maximum likelihood classification was then performed on the digital photo to assign each photo pixel to one of 3 surface types (green lichen, black lichen and rock). After grids of 0.45cm by 0.45cm (one grid cell corresponding to one spectral measurement) were overlaid on the classified photo, the abundance of each endmember within each spectral measurement grid was automatically estimated by counting the total number of pixels that belong to a given surface type on the photo.

4.2.2 Spectral features of lichens

In this section we summarize the key spectral features of rock encrusting lichens using typical spectra (Figure 4.2) obtained from the sample shown in Figure 4.1. Dark colored crustose and foliose lichens display a reflectance between 3 and 7% in the visible range. For green lichens such as *R. geographicum* the reflectance is near 5% at 400 nm and quickly rises to approximately 11-17% from 520 nm until the chlorophyll absorption at approximately 685 nm (Bechtel et al. 2002). *R. Geographicum* shows a green peak at approximately 550 nm that is more characteristic of vascular plants than some of the darker colored lichens. Based on these observations, Bechtel et al. (2002) devised two spectral ratios (400/685 nm against 773/685 nm) to isolate the spectral characteristics of different colors, types, and species of lichen. Both lichens display a gradual increase in reflectance to 1380 nm followed by an absorption feature centered near 1445 nm caused by water in the lichen. All lichens investigated by Bechtel et al. (2002) and Rivard and Arvidson (1992) then display an increase in reflectance reaching a maximum value

around 1860 nm. Beyond the water absorption feature near 1935 nm (masked on Figure 4.2) the spectra of lichens are similar in shape. A similar pattern was reported by Ager and Milton (1986) for a limited number of species. Three broad absorption features near 1730, 2100, and 2300 nm (Figure 4.2), are attributable to the presence of cellulose in lichen (Ager and Milton 1987; Bechtel et al., 2002). These are in turn accompanied by more subtle absorptions (e.g. 1690 and 1770 nm) whose amplitude can vary amongst species (Bechtel et al., 2002). Based on these observations and a difference of up to 10% in overall amplitude between lichen spectra in the short wave infrared, Bechtel et al. (2002) devised two spectral ratios (2132/2198 nm and 2232/2198 nm) to outline the similarity of lichen spectra in this spectral range.

4.2.3 Spectral mean normalization

Spectral mean normalization can be used to remove wavelength-independent magnitude differences between spectra and enhance wavelength-dependent effects (Cudahy et al., 1999). Thus it provides a means to suppress the reflectance magnitude differences between data sets caused by differing viewing and illumination geometry while enhancing differences in spectral shape. The spectral mean normalized spectrum can be calculated with the following equation:

$$r_n = \frac{r}{\bar{r}}, \quad (4-1)$$

where r_n is the normalized spectrum, r is the original spectrum, \bar{r} is the spectral mean over the defined spectral region.

Two spectra, r_1 and r_2 , differing only in spectral magnitude (e.g. varying illumination and viewing geometry), can be described by

$$r_1 = fr_2 \quad (4-2)$$

where f is a wavelength-independent multiplicative factor. The spectral means of these two spectra therefore will obey

$$\bar{r}_1 = f\bar{r}_2 \quad (4-3)$$

where \bar{r}_1 and \bar{r}_2 are spectral means for r_1 and r_2 , respectively. The normalized spectra have the following relationship:

$$r_{1_n} = \frac{r_1}{\bar{r}_1} = \frac{fr_2}{f\bar{r}_2} = \frac{r_2}{\bar{r}_2} = r_{2_n}, \quad (4-4)$$

where, r_{1_n} and r_{2_n} are spectral mean normalized spectra for r_1 and r_2 , respectively.

Given an atmospherically corrected airborne/spaceborne data, normalized image spectra should be comparable with normalized laboratory/field spectra for the same target. For lichen-rock mixtures, it is shown below that the normalized lab/field lichen spectra are similar to the normalized lichen endmember spectra estimated from the image of the rock sample.

4.2.4 SMA of normalized spectra

SMA uses a linear combination of reference spectra, known as endmembers, to approximate endmember abundances in a mixed pixel (Smith et al., 1990; Mustard and Sunshine, 1999). Typically the solution is obtained through least squares techniques (Shimabukuru et. al., 1991) and is constrained to yield abundances between 0 and 1 where the sum of the abundances for each pixel equals 1:

$$r_m = \sum_{k=1}^l EM_k * f_k \quad (4-5)$$

$$f_k \geq 0 \quad (4-6)$$

$$\sum_{k=1}^l f_k = 1.0 \quad (4-7)$$

where r_m is the spectrum of the mixture, EM_k is the spectrum for the k th endmember, l is the number of endmembers, and f_k is the weight (abundance) for the k th endmember in the mixture.

Given a linear mixture of endmembers, the normalized mixture spectrum can be written as

$$\frac{r_m}{r_m} = \sum_{k=1}^l \left(\frac{EM_k}{EM_k} \right) * \left(\frac{\overline{EM_k}}{r_m} * f_k \right) \quad (4-8)$$

where r_m and $\overline{EM_k}$ are the spectral mean for the mixture and the k th endmember, respectively.

Let

$$r_{m_n} = \frac{r_m}{r_m}, \quad (4-9)$$

$$EM_{k_n} = \frac{EM_k}{EM_k}, \quad (4-10)$$

$$f_{k_n} = \frac{\overline{EM_k}}{r_m} * f_k. \quad (4-11)$$

Equation 4-8 can be rewritten as

$$r_{m_n} = \sum_{k=1}^l EM_{k_n} * f_{k_n}, \quad (4-12)$$

where r_{m_n} is the normalized spectrum for the mixture, EM_{k_n} is the normalized spectrum for the k th endmember, and f_{k_n} is the weight for the k th endmember. Thus,

the normalized mixture spectrum can be modeled as the linear weighted sum of the normalized endmember spectra. This model is henceforth termed the Normalization Linear Mixture Model (NLMM) in this chapter.

The NLMM can also be constrained to yield weights (f_{k_n}) between 0 and 1 where the sum of the weights for each pixel equals 1:

$$f_{k_n} \geq 0 \quad (4-13)$$

$$\sum_{k=1}^l f_{k_n} = \sum_{k=1}^l \left(\frac{\overline{EM}_k}{r_m} * f_k \right) = \frac{1}{r_m} * \sum_{k=1}^l (\overline{EM}_k * f_k) = 1.0. \quad (4-14)$$

The NLMM presents advantages and disadvantages. A key advantage is the lack of sensitivity of the solution to errors in the magnitude of the endmember spectra, as is seen in SMA applied to reflectance spectra. A disadvantage is that it does not directly provide the abundance for each endmember. The relationship between the endmember abundance (f_k) and NLMM weight (f_{k_n}) is expressed by Eq. 4-11. In the results section below (Section 4.3), we show that the unmixing weight (f_{k_n}) from the NLMM correlates well with the abundance, and thus provides valuable relative abundance information in a scene.

4.3. RESULTS

4.3.1 Impact of the normalization on lichen spectra

Figure 4.3a displays spectra for 5 lichen species (*R. geographicum*, *R. bolanderi*, *R. geminatum*, *U. torrefacta*, and *A. cinerea*), the last three measured by Bechtel et al. (2002). Each spectrum is the mean of five 0.78 cm² locations. The data on Figure 4.3a

illustrate findings from previous studies suggesting that different lichen species have spectra with similar shapes but different magnitude in the SWIR. If we regard each spectrum as a vector in n-dimension space, the largest angle between spectra of this lichen group (Table 4-1) is 0.053 radians (approximately 3 degrees) confirming the similarity in spectral shape across species. Although differences in reflectance of approximately 5-11% are observed across different lichen species (Figure 4.3a), the normalization procedure greatly reduces the observed variability to 2- 6.5% (Figure 4.3b) and captures the spectral shape common to lichens while retaining their diagnostic spectral features (e.g. 2100 and 2300nm).

Using the digital photo (Figure 4-1), we identified thirty pixels (each 0.64 cm²) occupied by lichen (green or black lichen) from the hyperspectral image of the quartzite sample. The within-class variation was calculated in terms of maximum, minimum, standard deviation and mean values prior and after the normalization (Figure 4.3c, d). The data cover a larger lichen area than that shown in Figure 4.3a,b and provide a better assessment of the spectral variability within lichen species. The largest reflectance difference between lichen pixels is 0.32 (Figure 4.3c) whereas the difference for the normalized reflectance is less than 0.1 (Figure 4.3d). The standard deviation for the mean normalized spectrum is much smaller than that for the mean reflectance spectrum and largely encompasses the variability observed across species (Figure 4.3b). The normalization significantly suppresses the spectral variability within the lichen class.

4.3.2 Impact of the normalization on the extraction of image endmembers

4.3.2.1 *Visual extraction*

The spectral variability within the lichen class impacts the number of lichen spectra required for the SMA. Multi-dimensional scatter plots provide an intuitive way to explore the spectral variation in an image and interpret the mixture relationship between endmembers. For a scene devoid of topography, candidate endmembers should appear near the corners of the convex hull in n-dimension space (Boardman, 1993). The image data of the quartzite sample (Figure 4.1) were examined using three absorptions diagnostic of lichen (2100 and 2300nm) and quartzite (2200 nm) (Figure 4.4) that enhance the spectral contrast between lichen and rock. Pixels occupied solely by lichen are located along a line of unit slope in reflectance (Figure 4.4 a, b), due to the similarity in their spectral shape but varying magnitude. The geometry of the reflectance data cloud would require green and black lichen endmembers (circled on Figure 4.4 a, b) to explain the lichen rock mixtures. For the normalization data, the distinction between two lichen endmembers is removed (Figure 4.4d) or substantially reduced (Figure 4.4c) (0.018 at 1730nm in Figure 4.4c versus 0.32 in Figure 4.4a). As a result of the normalization, the distribution of the mixtures observed for the normalized data would typically be explained using the manual selection of one lichen and two rock endmembers as seen in Figure 4.4d.

4.3.2.2 Automated extraction

The task of defining all scene endmembers required to solve mixtures of interest can be difficult as evident from the importance attributed to the topic in the recent literature (Tompkins *et al.*, 1997; Bateson *et al.*, 2000; Okin *et al.*, 2001; Dennison *et al.*, 2003). The automatic endmember extraction tool available in the Imaging Spectrometer Data Analysis System (Staenz *et al.*, 1998) uses the Iterative Error Analysis (IEA) to find

endmembers from a hyperspectral scene. IEA is based on the residual error image generated when a data set is unmixed using a Weighted Nonnegative Least Squares approach (WNNLS) (Haskell et al., 1981). The average spectrum of the scene is used as the starting endmember to initialize the unmixing process. The residual error image is essentially a distance measurement in n -dimensional space (n = number of bands) between the average spectrum and each spectrum of the image, and is used to locate the pixels that encompass the largest errors. These pixels, which are the farthest away from the average spectrum, then form a new endmember to unmix the data and the initial average spectrum is discarded. This process is repeated until the number of endmembers specified by the user is reached or until a specified average error tolerance condition is met. For this study we used IEA with a predetermined average unmixing error tolerance of 0.02 to extract spectral endmembers from our reflectance and normalized reflectance images.

Two lichen (green and black lichen) and three rock endmembers (Figure 4.5a) were extracted from the reflectance image. In contrast three endmembers (one lichen and two rocks; Figure 4.5b) were extracted from the normalized reflectance image. These number and type of endmembers are consistent with those determined from the visual extraction. From this analysis, a key finding is that the SMA of normalized reflectance does not require any a priori knowledge of lichen speciation because any lichen spectrum can be used to unmix any mixture of rock and lichen for the 2000-2400 nm range.

4.3.3 Unmixing results

In this section we present the unmixing results of the SMA and NLMM (Figure 4.6) conducted respectively on the reflectance and normalized reflectance images using the

endmembers extracted from the IEA (Figure 4.5). The results are compared to the abundances of rock and lichen calculated from the digital photograph (Figure 4.1). The ordinary least squares solutions of the mixture model (Eq. 4-5 and 4-12) may yield values less than 0 and larger than 1 in the absence of constraints, but these values were set to 0 and 1 respectively in the constrained unmixing procedure. To minimize the impact of this factor on the regression analysis, the pixels which have unmixing results equal to 0 or 1 were excluded from the following analysis. The coefficient of determination (e.g. R^2) for the reflectance image is 0.91 (Table 4-2) for lichen and rock (Figure 4.5 a, b). The slope of the regression equations is near unity (≥ 0.95), and the intercepts close to 0 (< 0.06). The standard error of the regression for the reflectance image is 0.09 (Table 4-2) for lichen and rock indicating that the image data can be modeled well with the five endmembers extracted from the IEA. For the normalized reflectance image the coefficient of determination is also above 0.9 for lichen (0.92) and rock (0.91) (Figure 4.5 c, d). The slope of the regression equations is 0.86 and 0.85, and the intercept is 0.13 and 0.02 for lichen and rock respectively. The unmixing coefficients from the NLMM are not equal to abundances due to the inherent property of the NLMM (Equation 4-11), and thus the regression slopes do not approach a value of 1. However the small standard error of the regression (0.08 for lichen and rock; Table 4-2) demonstrates that the NLMM fits the data well with one normalized lichen endmember.

4.4. DISCUSSION AND CONCLUSIONS

The results of this study have important implications for the geological analysis of airborne/spaceborne hyperspectral data where rock encrusting lichens partially obscure

exposed bedrock. Rock encrusting lichens mask their substrate (Bechtel et al., 2002) and thus modulate the spectral signature of bedrock complicating the detection and quantitative mapping of minerals and rocks from imagery. Studies have shown that lithologic mapping is feasible using mixtures of lichen and rock as image endmembers (Staenz et al., 2000) but the identification and abundance estimation of minerals is negatively impacted. In addition such an approach is not likely to capture a broad range of lithologic spectral variability and would fail in instances where lichen exposure on a given rock substrate is regionally variable due to local topography or microclimate as is observed in regions of high and low latitudes.

We propose that lichen be used as an endmember in SMA to overcome these limitations. Because lichens rarely completely occupy image pixels, it is not feasible to define a lichen endmember from an image using visual or automated extraction tools. The results of this study suggest that this limitation can be surmounted using published spectra of rock encrusting lichens combined with the use of a normalization procedure applied to image and endmember spectra. Normalized spectra of five lichen species were found to be similar in shape and magnitude in the SWIR. This suggests that it may be feasible to perform the SMA of airborne/spaceborne imagery using a NLMM and one of any field/laboratory lichen spectra. The NLMM provides geologists with an opportunity to group all lichens into one endmember and further the analysis of rock and lichen mixtures without detailed knowledge of lichen species occurring in the region of interest.

The unmixing coefficients of NLMM provide a relative measure of endmember abundance as described in Section 4.2.4. Thus, two pixels with identical covers types and distribution but differing in local physical surface conditions (e.g. microtopography), will

result in identical NLMM unmixing coefficients because the albedo variation would be minimized by the normalization. In contrast, the unmixing abundances computed from SMA applied to the reflectance of the two pixels would not be comparable due to the magnitude difference between the selected endmember spectrum for SMA and the location-specific required spectrum. When computed for a scene, the NLMM unmixing coefficient for lichen will be a uniform indicator of the lichen coverage within the pixels of the scene. This feature of NLMM is helpful to label pixels using threshold method applied to the unmixing coefficients.

Finally the normalization may subdue the spectral magnitude differences among rocks, based on the lower number of rock endmembers predicted by the IEA for the normalized data (Figure 4.4, 4.5). Alternately the three rock endmembers extracted for the reflectance data may result from microtopography given that they differ principally in magnitude. The effect of microtopography on spectral amplitude would be minimized by the normalization and is consistent with fewer rock endmembers predicted for the normalized data (Figure 4.5b). An analysis of airborne/spaceborne imagery using the NLMM is required to adequately address this issue and represents the next step in this research.

ACKNOWLEDGEMENT

This research was funded by grants from the Geoides Canadian Network Centres of Excellence and the National Science and Engineering Research Council of Canada. We thank R. Bechtel from providing access to his spectral library for lichens, Karl Staenz

of the Canada Center for Remote Sensing for access to ISDAS, and Tom Cudahy for useful discussions.

REFERENCES

- Ager, C. M., and Milton, N. M., 1987, Spectral reflectance of lichens and their effects on the reflectance of rock substrates. *Geophysics*, v. 52, p. 898-906.
- Analytical Spectral Devices, 2001, www.asdi.com, 5335 Sterling Drive, Suite A, Boulder, CO 80301.
- Bateson, C. A., Asner, G. P. and Wessman, C. A., 2000, Endmember Bundles: A New Approach to Incorporating Endmember Variability into Spectral Mixture Analysis, *IEEE Transactions on Geoscience and Remote Sensing*, v. 38, p. 1083-1094.
- Bechtel, R., Rivard, B. and Sanchez, A., 2002, Spectral properties of foliose and crustose lichens based on laboratory experiments, *Remote Sensing of Environment*, v. 82, p. 389–396.
- Bierwirth, P., Huston, D., and Blewett, R., 2002, Hyperspectral mapping of mineral assemblages associated with gold mineralization in the central Pilbara, western Australia, *Economic Geology*, v. 97, p. 819-826.
- Boardman, J.W., 1993, Automating spectral unmixing of AVIRIS data using convex geometry concepts, *Summaries of the fourth Annual JPL airborne Geoscience Workshop*, JPL Publication 93-26, vol. 1: 11-14.
- Cudahy, T. J., Okada, K., Ueda, K., Brauhart, P., Huston, D., Cocks, T., Wilson, J., Mason, J. and Huntington, J.F., 1999, Mapping the Panorama VMS-style Alteration

and host rock mineralogy, Pilbara Block, using hyperspectral VNIR-SWIR data, *CSIRO report*.

- Dennison, P. E. and Roberts, D. A., 2003, Endmember selection for multiple endmember spectral mixture analysis using endmember average RMSE, *Remote Sensing of Environment*, v. 87, p. 123-135.
- Goetz, A.F.H., Rock, B.N., and Rowan, L.C., 1983. Remote sensing for exploration: an overview. *Economic Geology*, v. 28, p. 573–590.
- Haskell, K. H. and Hanson, R. J., 1981, An algorithm for linear least squares problems with equality and non negativity constraints, *Mathematical Programming*, v. 21, p. 98-118.
- Hunt, G.R., 1979, Near-infrared (1.3–2.4 mm) spectra of alteration minerals— potential for use in remote sensing, *Journal of Geophysics*, v. 44, p.1974–1986.
- Huntington, J.F., Green, A.A. and Craig, M.D., 1989, Identification — the goal beyond discrimination. In *Proceedings of the 12th Canadian Symposium on Remote Sensing and the International Geoscience and Remote Sensing Symposium (IGARSS'89)*, 10–14 July 1989, Vancouver, B.C. IEEE, Piscataway, N.J. pp. 6–11.
- Mustard, J.F. and Sunshine, J.M., 1999, Spectral analysis for earth science: investigations using remote sensing data, *Remote sensing for earth sciences: Manual of Remote Sensing*, 3rd ed., v.3, ed. A.N. Rencz, John Wiley and Sons, New York, p. 251-307.
- Neville, R.A., Rowlands, N., Marois, R. and Powell, I., 1995, SFSI: Canada's first airborne SWIR imaging spectrometer, *Canadian Journal of Remote Sensing*, v. 21, p. 328–336.

- Neville, R.A., Staenz, K, Szeredi, T., Lefebvre, J. and Hauff, P., 1999, Automatic endmember extraction from hyperspectral data for mineral exploration, http://www.ccrs.nrcan.gc.ca/ccrs/rd/sci_pub/bibpdf/4637.pdf.
- Okin, G.S., Roberts, D. A., Murray, B. and Okin, W.J., 2001, Practical limits on hyperspectral vegetation discrimination in arid and semiarid environments, *Remote Sensing of Environment*, v.77, p. 212-225.
- Rivard, B. and Arvidson, R. E., 1992, Utility of imaging spectrometry for lithologic mapping in Greenland, *Photogrammetric Engineering and Remote Sensing*, v. 58, p. 945– 949.
- Rollin, E.M., Milton, E.J and Roche, P., 1994, The influence of weathering and lichen cover on the reflectance spectra of granitic rocks, *Remote sensing of Environment*, v. 50, p. 194-199.
- Satterwhite, M. B., Henley, J. P. and Carney, J. M., 1985, Effects of lichens on the reflectance spectra of granite rock surfaces, *Remote Sensing of Environment*, v. 18, p. 105-112.
- Shimabukuru, Y.E. and Smith, J.A., 1991, The least squares mixing models to generate fraction images derived from remote sensing on multispectral Data, *IEEE Transactions on Geoscience and Remote Sensing*, v. 29, p.16-20.
- Smith, M., Ustin, S. L., Adams, J. B., and Gillespie, A. R., 1990, Vegetation in deserts: I. A regional measure of abundance from multispectral images, *Remote Sensing of Environment*, v.31, p. 1-26.

- Solheim I., 2000, Measurement and modeling of the spectral and directional reflection properties of lichen and moss canopies, *Remote Sensing of Environment*, v. 72, p. 78-94.
- Staenz K., Nadeau C., Secker J. and Budkewitsch P., 2000, Spectral Unmixing Applied to Vegetated Environments in the Canadian Arctic for Mineral Mapping, *XIXth ISPRS Congress and Exhibition*, Amsterdam, July, 15-23.
- Staenz, K., Szeredi, T. and Schwarz. J., 1998, ISDAS - A System for Processing/Analyzing Hyperspectral Data; Technical Note, *Canadian Journal of Remote Sensing*, v. 24, p. 99-113.
- Tompkins, S., Mustard, J. F., Pieters, C. M. and Forsyth, D. W., 1997, Optimization of endmembers for spectral mixture analysis, *Remote Sensing of Environment*, v. 59, p. 472-489.

Table 4-1 Spectral angles (radian) between five lichen species measured from 2000-2400 nm. (The spectrum for each species for the corresponding spectral region is shown on Figure 4.3a.)

	<i>R.geminatum</i>	<i>U. torrefacta</i>	<i>R. bolanderi</i>	<i>A. cinerea</i>	<i>R. geographicum</i>
<i>R. geminatum</i>	0.000	0.021	0.017	0.026	0.038
<i>U. torrefacta</i>	0.021	0.000	0.011	0.014	0.051
<i>R. bolanderi</i>	0.017	0.011	0.000	0.022	0.053
<i>A. cinerea</i>	0.026	0.014	0.022	0.000	0.046
<i>R. geographicum</i>	0.038	0.051	0.053	0.046	0.000

Table 4-2 Statistics for regressions between the unmixing results and true abundance for rock and lichen

	Reflectance		Normalized Reflectance	
	Lichen	Rock	Lichen	Rock
Confidence interval	95%	95%	95%	95%
R squares	0.91	0.91	0.92	0.91
Standard error of the regression	0.09	0.09	0.08	0.08
Slope / p-value	0.95 / 0.00	0.96 / 0.00	0.86 / 0.00	0.85 / 0.00
Intercept / p-value	0.06 / 0.00	0.00 / 0.00	0.13 / 0.00	0.02 / 0.00

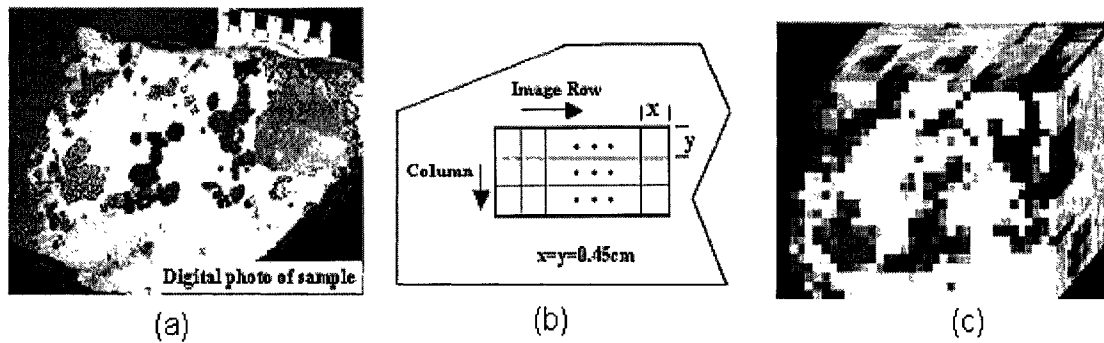


Figure 4.1 Photograph of the lichen encrusted quartzite sample and resulting hyperspectral data cube. (a) Digital photo of rock sample showing green lichen (*R. geographicum*) and black lichen (*R. bolanderi*) and the red cross marks used for coregistration with the spectral data; (b) schematic diagram of the spectral measurement layout. Each cell (0.45 cm by 0.45cm) is corresponding to one spectral measurement; the sample is translated through the field of view of the instrument along two directions (showed by the two arrows), that correspond to the image rows and columns in (c); (c) Hyperspectral image cube generated according to the measurement layout illustrated in (b). This is a three dimensional view of the spectral data. The front face is a color composite of bands 430nm (Blue), 550nm (Green) and 710nm (Red). The top and side faces of the cube are colored to show the reflectance variation with wavelength of pixels in the first row and last column (red means high value).

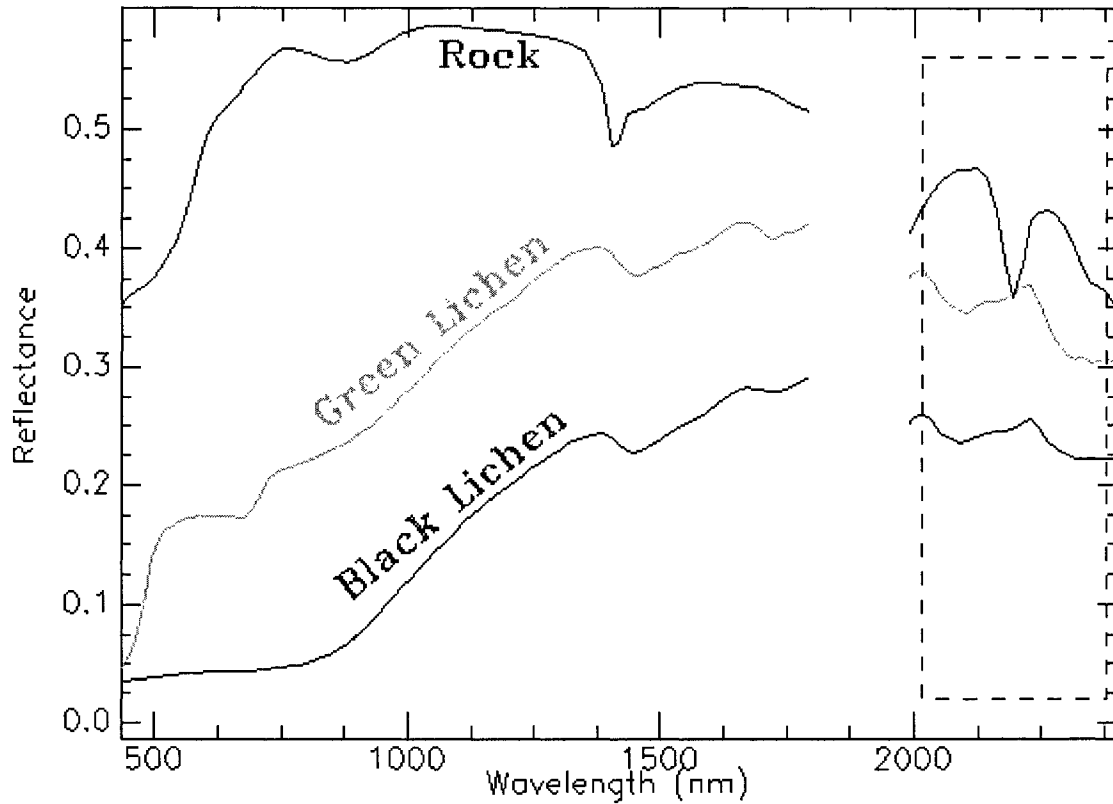


Figure 4.2 Type spectra obtained for the sample shown in Figure 4.1. The strong water absorption feature near 1900 nm was discarded because of low signal. The Box marks the short wave infrared (SWIR) spectral region used in figures below (Figure 4.3, 4.4 and 4.5). Quartzite has a strong hydroxyl (OH) absorption feature near 2194nm distinct from the broader absorptions features centered near 2100 nm and 2300 nm displayed by lichen.

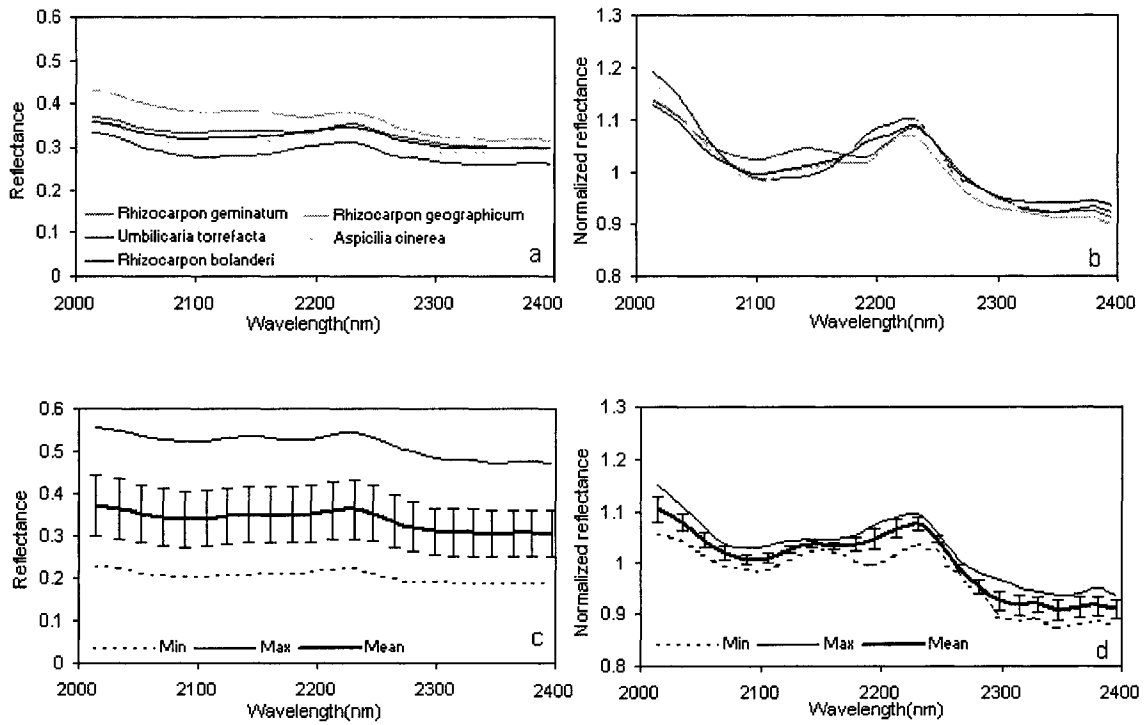


Figure 4.3 Variability in lichen spectra in reflectance and normalized reflectance. a, b: Spectra of five lichen species. Each spectrum is the mean of five different 0.78 cm^2 locations; c, d: Minimum, maximum and mean \pm one standard deviation value of thirty pixels (each 0.64 cm^2) occupied by lichen (green or black lichen) from the hyperspectral image of the quartzite sample (Figure 4.1).

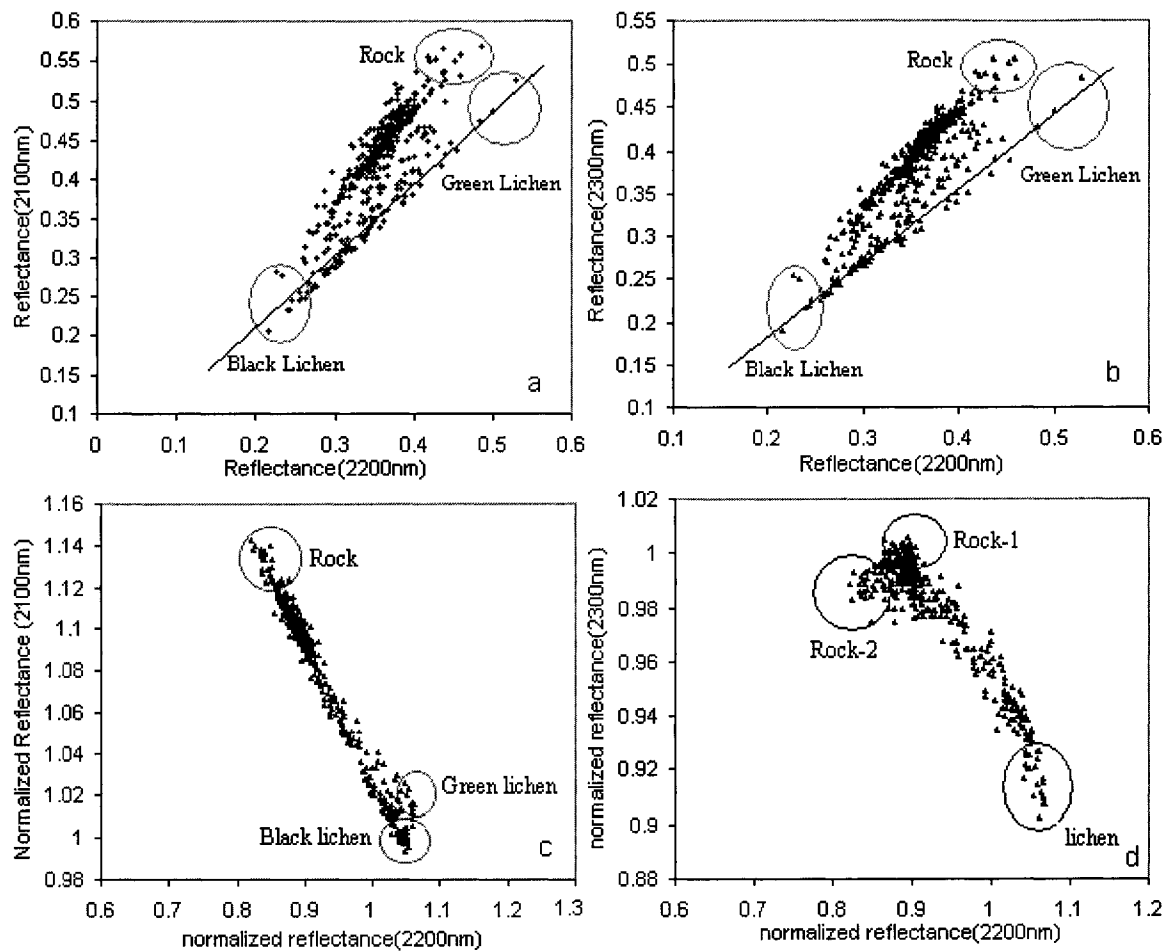


Figure 4.4 Data clusters for the image shown on Figure 4.1 prior to (a and b) and following the spectral normalization (c and d). Circles mark the location for the visual extraction of potential endmembers. Black lines have a unit slope. Pixels occupied solely by lichen are located along this line due to the similarity in their spectral shape but varying magnitude (a, b). The distinction between two lichen endmembers is removed (d) or substantially reduced (c) (0.018 at 1730nm in c versus 0.32 in a).

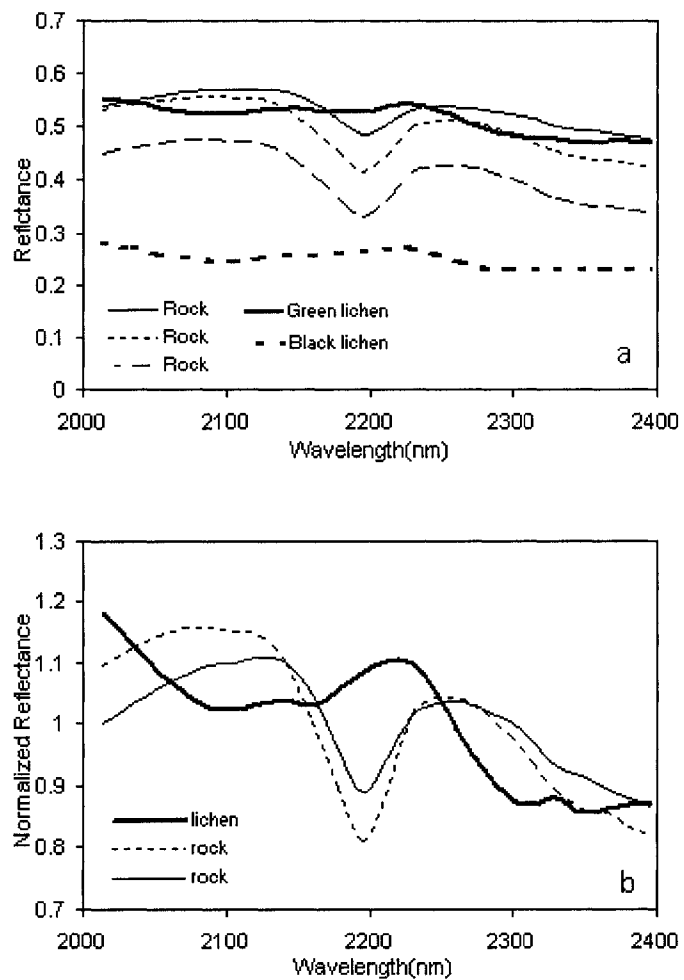


Figure 4.5 Endmember spectra predicted using the IEA for the reflectance image (a), and the normalized reflectance image (b). Only one lichen endmember is required to solve the lichen-rock mixture of the normalized image.

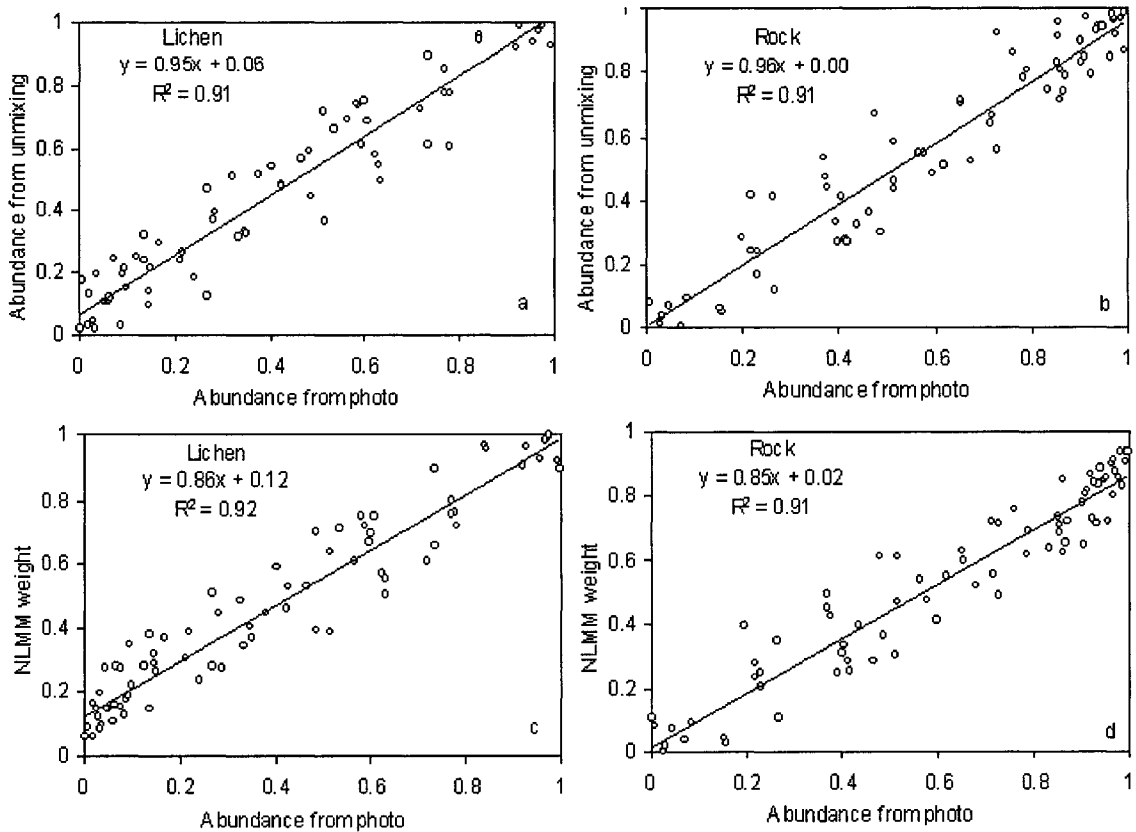


Figure 4.6 Comparison between the abundance of lichen and rock estimated from the photo and the unmixing results using the endmembers shown in Figure 4.5. (a) and (b) for unmixing results from reflectance data; (c) and (d) for unmixing results from normalized reflectance data. For the reflectance image, the unmixing results are abundances directly comparable with those estimated from the photo. For the normalized reflectance image, the unmixing results are weights proportional to the abundances estimated from the photo.

CHAPTER 5

CONCLUSIONS AND FUTURE WORK

5.1 CONCLUSIONS

This study has explored the feasibility of using hyperspectral data for lithologic mapping in vegetated areas. Three topics relevant to the analysis of such data were addressed, namely the impact of vegetation on the extraction of geological endmembers, the deconvolution of lichen and rock mixtures, and the development of novel spectral mixture models to facilitate the retrieval of rock signatures from hyperspectral data. The recurring theme of the research is the challenge of retrieving valuable lithologic information from hyperspectral data in the presence of vegetation and lichens. The major achievements of this thesis can be summarized as follows.

- (a) Limitation exists in the convex-based endmember selection method when applied to the retrieval of rock signatures (in the hyperspectral domain) in vegetated regions with a low abundance of rock outcrops. In a case study the method failed to provide useful geological endmembers. The convex-based method is fundamentally a statistical approach dependent on the spectral variance of the scene. In vegetated areas, rock outcrops commonly occupy a very low percentage of the land cover. Most of the scene variance is determined by the dominant cover type, i.e. vegetation; consequently, the method is optimal for the analysis of vegetation. The selection of spectral endmembers should be guided by field observations and measurements to perform the spectral mixture analysis.

- (b) The traditional accuracy assessment methodology (e.g. confusion matrix) may not be adequate to perform accuracy checks when map units consist of dispersed small patches. The analysis of hyperspectral data for a greenstone belt exposed north of Rouyn Noranda shows that the accuracy assessment method appears to work fairly well for map units with large patches and rock types with substantial outcrop exposure (e.g. rhyolite), but may not be suitable to assess the accuracy for map units with small patches (e.g. diorite). In such instances a mismatch of a few outcrops between image and map or the lack of a precise location for an outcrop or map contact will substantially impact the accuracy of results. Fieldwork rather than image to map verifications may still be the most effective means to assess the unmixing results.
- (c) A novel partial spectral unmixing model, the DSU, was developed by incorporating the derivative spectra into SMA. The key strength of DSU is that the abundance estimation of endmembers does not require a thorough knowledge of all endmembers at hand as long as the unknowns do not display conflicting absorptions features with that of the material of interest. By using derivative spectra instead of reflectance spectra, DSU is relatively insensitive to variations in illumination intensity caused by changes in sun angle, cloud cover, or topography. In other words, DSU emphasizes the spectral shape of the target that is directly relevant to the composition of the target. The DSU results for the laboratory experiment show that the algorithm is promising for the quantitative analysis of hyperspectral data. The DSU can be used for the direct abundance estimation of minerals without a detailed spectral knowledge of non-geological targets because

many minerals have absorption features distinct from those of non-geological targets (e.g. vegetation). In addition, by focusing on a spectral region unique to lichens (e.g. 1730 nm) where rock/minerals lack spectral contrast, it may be feasible to use the DSU to determine the lichen coverage within each pixel of a hyperspectral image and further purify the rock spectra contaminated by the signature of lichen.

- (d) A spectral mean normalization can suppress intra-class variation for a variety of targets including lichen, and the NLMM provides a novel way to deconvolve the lichen-rock mixtures using one of any field/laboratory lichen spectra if the analysis uses the SWIR spectral region. The normalization can minimize amplitude differences in reflectance amongst spectra while retaining the spectral shape, which makes it feasible to use field or laboratory spectra as endmembers. The normalized spectra of five lichen species were found to be very similar in shape and magnitude in the SWIR, which provides geologists with an opportunity to group all lichens into one endmember using NLMM and further the analysis of rock and lichen mixtures without a detailed knowledge of lichen species occurring in the region of interest.

5.2 FUTURE WORK

The research of this thesis demonstrates the challenges and potential of lithologic mapping using hyperspectral data in vegetated regions. The following research avenues have been identified for future work.

Two novel unmixing methods (DSU and NLMM) were proposed in this study, but they were tested on spectral measurements conducted in the laboratory using a simple scene (a rock sample). Tests on natural scenes are now required to assess their value for applied geologic remote sensing. There may also be benefit in an analysis that combines both methods.

An absorption feature was observed at 1730nm for all lichen species, which opens the possibility to use the DSU to estimate the lichen abundance based on the 2nd derivative value at this wavelength. Further research is required to handle the range of values observed for lichens at this wavelength during estimation of lichen abundance in lichen-rock mixtures and perhaps to remove the lichen contribution from rock endmembers extracted from the image data.

APPENDIX 1

DISCRIMINATION BETWEEN LICHEN AND ROCK/MINERALS USING SECOND ORDER DERIVATIVE SPECTRA

A1.1 BACKGROUND

As evident from the previous Chapters and related literature (Ager and Milton, 1987; Rivard and Arvidson, 1992; Rollin et al., 1994; Staenz et al., 2000, Bechtel et al., 2002), the ubiquitous presence of lichen coatings on rock outcrops is a challenge for lithologic mapping using imaging spectrometer data collected at high latitudes, because lichens affect the overall spectral shape and can mask spectral features of the host rock.

Chapter 3 elaborated a mixing model whereby the abundance of a single spectral endmember in a mixture could be calculated if the assumption that the endmember was characterized by a unique spectral feature could be met. In nature, lichens are observed in the presence of a wide variety of minerals/rocks. For the DSU to be of use in the deconvolution of lichen and rock/mineral mixtures, one needs to know if one or many spectral features observed in lichens are unique with respect to minerals. Ager and Milton (1987) suggested that wavelengths 1730nm and 2100nm may be candidates for this purpose. Bechtel et al. (2002) examined the use of the 2200nm band for the discrimination of lichens and quartzite. The quartzite displayed a hydroxyl absorption feature at 2198nm, and Bechtel et al. (2002) designed a ratio index ($2132/2198$ vs. $2232/2198$) effective for the separation of lichens from a hydroxyl feature at this wavelength. The study failed to examine a wide range of documented hydroxyl features that cover other portions of the short wave infrared spectrum. In this appendix the

spectral properties of an extensive mineral spectral library are contrasted with that of lichens at these key wavelengths to assess their uniqueness and usefulness for the discrimination of lichens and rocks. The derivative analysis described in Chapter 3 was used to: (1) capture the spectral absorption features of lichens; (2) identify an optimal wavelength to distinguish lichens from minerals/rocks; (3) explore the benefit of 2nd derivative spectra for the interpretation of the rock-lichen mixture.

A1.2 DESCRIPTION OF THE DATA

The publicly available USGS mineral spectral library (Clark, et al., 1993) and the lichen spectral library of Bechtel et al. (2002) were used to explore the variation of 2nd derivative spectra across different minerals and lichen species. The USGS mineral library contains spectra of 423 minerals and has been used extensively as a reference for mineral identification in hyperspectral remote sensing (Clark, et al., 1993). The lichen spectral library consists of 85 spectra collected from five rock encrusting lichen species (*R. geographicum*, *R. bolanderi*, *R. geminatum*, *U. torrefacta*, and *A. cinerea*). Measurement details are described by Bechtel et al. (2002).

The hyperspectral image of a lichen encrusted quartzite sample was used to assess the results derived from the analysis of spectral libraries and to demonstrate how the derivative spectra facilitate the analysis of mixing relationships between lichen and rock. The sample comprises three surface types, namely green lichen (*R. geographicum*), black lichen (*R. bolanderi*) and the rock substrate (*quartzite*). The detailed description of the experimental setup and spectral features for these surfaces can be found in Chapter 3 and 4.

A1.3 RESULTS

A1.3.1 Absorption features of lichen

Spectral studies of lichens in the past have revealed that lichens share some absorption features at wavelengths 680nm, 1730nm, 2100nm and 2300nm (Ager and Milton, 1987; Bechtel et al., 2002). The feature at 680nm is attributed to the presence of chlorophyll while features at 1730nm, 2100nm and 2300nm are related to cellulose (Ager and Milton, 1987; Rivard and Arvidson, 1992). Generally these spectral features are broad and relatively shallow. Using 2nd derivative spectra, the background (continuum) can be removed to highlight these spectral features. The calculation of derivatives is described in Chapter 3. Figure A1-1 provides an illustration of both reflectance and 2nd derivative spectra for two lichen species (*R. geographicum* and *R. bolanderi*). The broad and shallow absorption features on the reflectance spectra (Figure A1-1a) become distinctive peaks on the 2nd derivative spectra (Figure A1-1b) and the interference of the background has been minimized.

A1.3.2 Optimal band for discrimination of rock and lichen

An optimal band for separation of lichens from minerals should be one where lichens have a diagnostic absorption feature but most minerals are spectrally flat. In other words, minerals should have zero (or near zero) 2nd derivative values at this band while lichens have significantly nonzero 2nd derivative values.

Figure A1-2 indicates that lichens have positive 2nd derivative values at both 1730 and 2100nm while minerals have zero means but the values spans a large range. The range of 2nd derivative values for lichens overlaps with that of minerals at both bands.

The overlap is particularly large at 2100nm where mineral values span a large range from -0.093 to 0.149. A further examination of the 2nd derivatives values at 1730nm and 2100nm as a function of minerals (Figure A1-3) reveals that a number of minerals have non-zero values. The twenty most extreme values include *Alunite*, *Actinolite*, *Azurite*, *Antigorite*, *Buddingtonite*, *Colemanite*, *Cookeite*, *Dickite*, *Halloysite*, *Howlite*, *Kaolinite*, *Lizardite*, *Margarite*, *Niter*, *Pinnoite*, *Pyrophyllite*, *Scolecite*, *Sillimarite*, *Syngenite*, and *Topaz*, of which some are common rock forming minerals or minerals of value for remote sensing exploration (Figure A1-3a). Consequently the 2100nm band cannot be exploited for DSU without compromising the detection of these important minerals. The variation of the 2nd derivative values at 1730nm is considerably smaller (Figure A1-3b). Nine minerals (*Analcime*, *Azurite*, *Carnallite*, *Datolite*, *Gypsum*, *Jarosite*, *Mascagnite*, *Natrolite* and *samarium oxide**) have extreme positive/negative values. And of these only *gypsum* is considered as one of common rock forming minerals. When these nine minerals are excluded from the database, the 2nd derivative values for minerals at 1730nm span a small range that does not overlap with that of lichens (Figure A1-4). Thus the 2nd derivative values of the lichen rock mixtures at 1730nm are predominantly determined by the abundance and type of lichens. Figure A1-5 indicates that green and black lichens respectively occupy the upper and lower range of 2nd derivative values at 1730 nm.

A1.3.3 Rock-lichen mixtures for the quartzite sample

Scatter plots are commonly used to visually and intuitively explore the separability of, and relationship between, endmember clusters in hyperspectral data. In this section, a

* I regarded Samarium oxide as one mineral in this thesis according to the documentation of USGS spectral library (USGS, 2000). But it is a reagent-grade chemical material (Sm_2O_3) used to study the absorption features due to the presence of samarium in the mineral (Rowan et al., 1986).

scatter plot of data at 680nm and 1730nm was selected to analyze the mixing relationships between rock and lichens (Figure A1-6). The wavelength 680nm was utilized because it represents the chlorophyll absorption that varies with different lichen species (Ager and Milton, 1987). The 2nd derivative values at this band will represent variability in band depth of the chlorophyll absorption. Spectra with greatest band depth display the largest 2nd derivatives. The wavelength 1730nm was used because as seen above, this band is unique to lichens and thus helps to distinguish lichen from minerals. To display the location of pure pixels (endmembers) in the scatter plot (Figure A1-6), the digital photo was used to identify three areas for three surface types (green lichen, black lichen and rock), respectively. In the scatter plot of reflectance values, clusters for the three surface components are relatively broad and poorly defined (Figure A1-6a) complicating the selection of endmembers and the visualization of mixing relationship. On Figure A1-6b however, the 2nd derivative values for rock pixels are close to zero and the data points for pure rock pixels form a smaller and denser cluster. Pixels for black lichen have 2nd derivative values close to zero at 680nm and an intermediate positive value (around 0.04) at 1730nm because black lichen has a weak chlorophyll absorption feature (Figure A1-1). The pixels for green lichen have the largest 2nd derivative values at both 680nm and 1730nm because of the stronger chlorophyll absorption feature and cellulose absorption feature (1730nm) (Figure A1-1). Based on the geometry of the whole data cloud, three endmembers can clearly be identified: rock and two lichens. In addition one can infer that most mixed pixels are composed of black lichen + rock.

A1.4. DISCUSSION AND CONCLUSION

With the aid of the 2nd derivative spectra, the band at 1730nm was found to be robust for the separation of lichens from minerals (Figure A1-4). It follows that one can quickly distinguish the lichen-dominated pixels from the rock-dominated pixels based on the 2nd derivative value at this band. A simple segmentation can thus be used to crop the lichen-dominated pixels from further spectral analysis and may facilitate the identification of “purer” pixels. This band is also a potential wavelength region where the DSU (Chapter 3) could be applied to group all lichen into one class and remove or minimize the effect of lichen in rock/lichen mixtures.

The scatter plot of 2nd derivative values at 1730nm and 680nm was found to be helpful to interpret the lichen-rock mixtures and identify potential lichen endmembers. The starting point of this observation is that rock/mineral are spectrally featureless around 680nm and 1730nm but different lichen species will tend to have different absorption depth at these wavelengths. By removing the background and highlighting the spectral shape differences among different surface types, the 2nd derivative values of rock pixels cluster near a (0,0) value and the spectral difference across lichen species are accentuated. Lichens of different colors, which are a function of the chlorophyll pigmentation, will tend to plot in different clusters. In this study, pure green and black lichen pixels occupy two corners of the data cloud. By using this scatter plot, we can visually examine the mixing relationships between rock and different lichens.

It should be pointed out that mixtures of lichen and rock in this study were considered without the interference of other components. Nature is more complex. For instance, dry plant materials frequently have absorption features near 1730nm (Elvidge,

1990), and thus lichens cannot be separated from dry plant materials using only the 2nd derivative values at 1730nm. Thus, caution is required when applying the results of this study to regions where dry plant material is an important surface component.

The results presented in this appendix are based on spectral libraries with a limited number of lichen species. The effectiveness of the method proposed needs to be tested with airborne/spaceborne hyperspectral data. Because the method is based on derivative analysis, the noise level of the derivative spectra calculated from such data will be a key consideration to determine its value for applied work.

REFERENCES

- Ager C.M. and Milton N.M., 1987, Spectral reflectance of lichens and their effects on the reflectance of rock substrates, *Geophysics*, v. 52, p. 898-906.
- Bechtel, R., Rivard, B and Sanchez, A., 2002, Spectral properties of foliose and crustose lichens based on laboratory experiments, *Remote Sensing of Environment*, v. 82, p. 389–396.
- Demetriades-Shah, T. H., Stevenand, M. D. and Clark, J. A., 1990, High Resolution Derivatives Spectra in Remote Sensing, *Remote Sensing of Environment*, v. 33, p. 55-64.
- Elvidge, C. D., 1990, Visible and Near Infrared Reflectance Characteristics of Dry Plant Materials. *International Journal of Remote Sensing*, v. 11, p. 1775-1795.
- Huiand, K. and Gratzl, M., 1996, Anomalies of convolutional smoothing and differentiation, *Analytical Chemistry*, v. 68, p. 1054-1057.

- Rivard, B., and Arvidson, R.E., 1992, Utility of imaging spectrometry for lithologic mapping in Greenland, *Photogrammetric Engineering and Remote Sensing*, v. 58, p. 945-949.
- Rollin, E. M., Milton, E. J. and Roche, P., 1994, The influence of weathering and lichen cover on the reflectance spectra of granite rocks, *Remote Sensing of Environment*, v. 50, p. 194-199.
- Rowan, L. C., Kingston, M. J. and Crowley, J. K., 1986, Spectral Reflectance of Carbonatites and Related Alkalic Igneous Rocks: Selected Samples from Four North American Localities, *Economic Geology*, v. 81, p. 857-871.
- Satterwhite, M. B., J. P. Henley, and Carney, J. M., 1985, Effects of lichens on the reflectance spectra of granitic rock surfaces. *Remote Sensing of Environment*, v. 18, p. 105-112.
- Tsai, F. and Philpot, W., 1998, Derivative analysis of hyperspectral data, *Remote Sensing of Environment*, v. 66, p. 41-51.
- USGS, 2000, <http://speclab.cr.usgs.gov/spectral.lib04/DESCRIPT/samarium.GDS36.html>

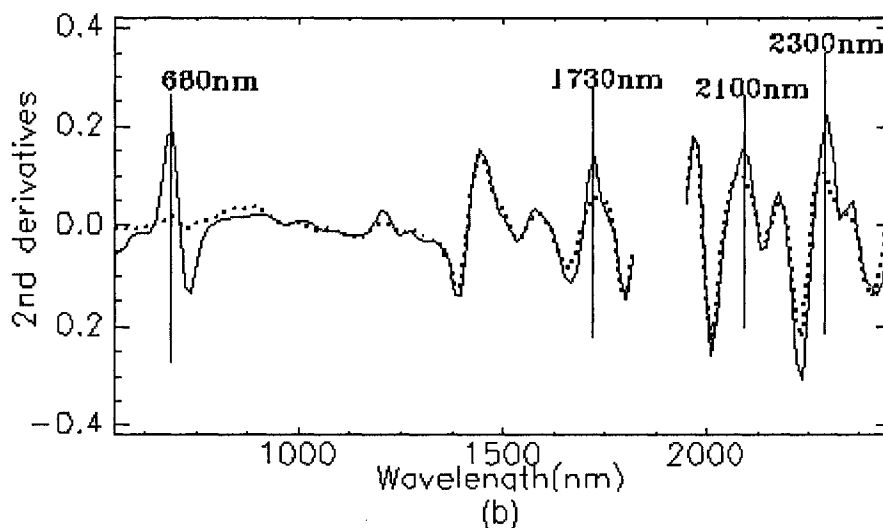
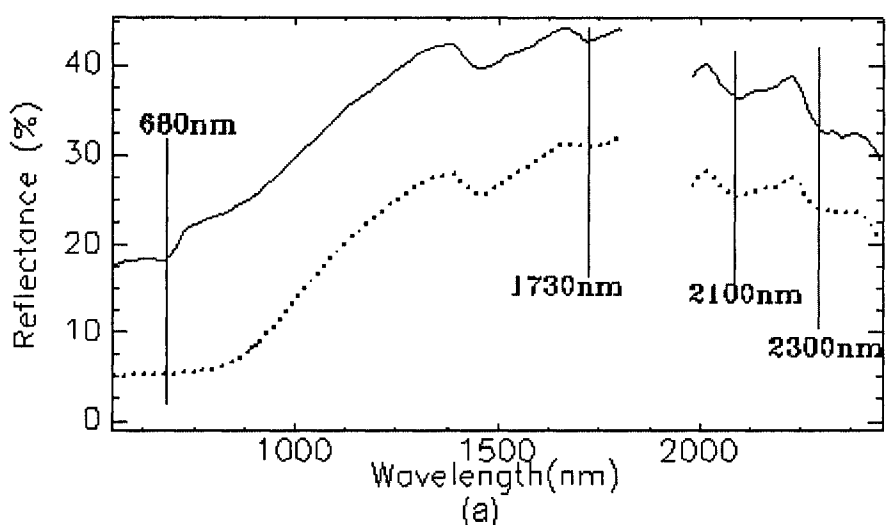


Figure A1-1 Comparison between reflectance (a) and 2nd derivative spectra (b) for two lichen species. Solid and dashed lines are for *R. geographicum* and *R. bolanderi* respectively. The dominant lichen spectral features were labeled with vertical blue lines. The spectral region near 1900nm was masked because of the high noise level due to the strong water absorption.

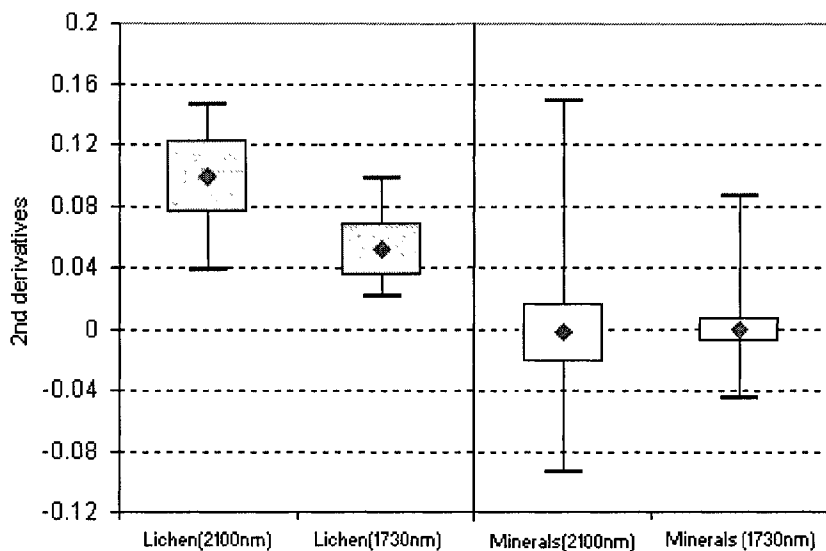
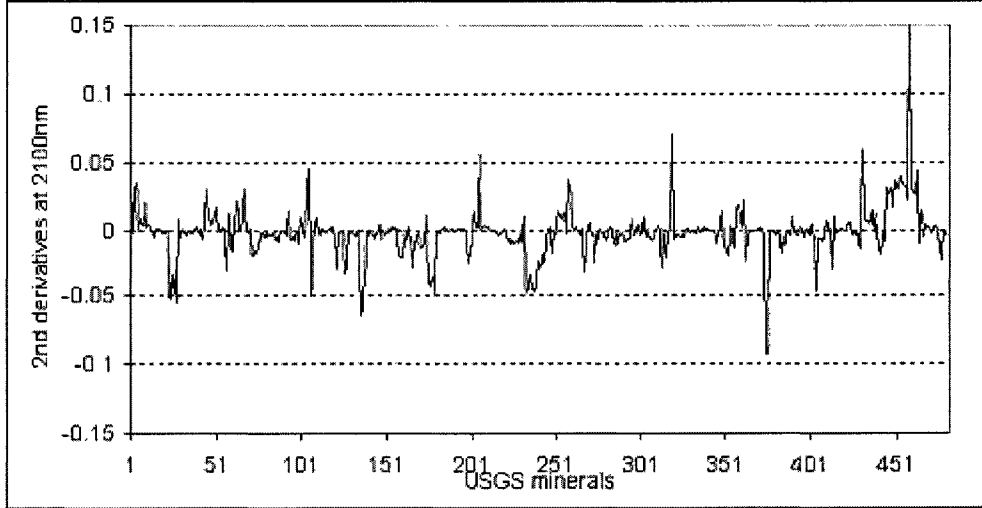
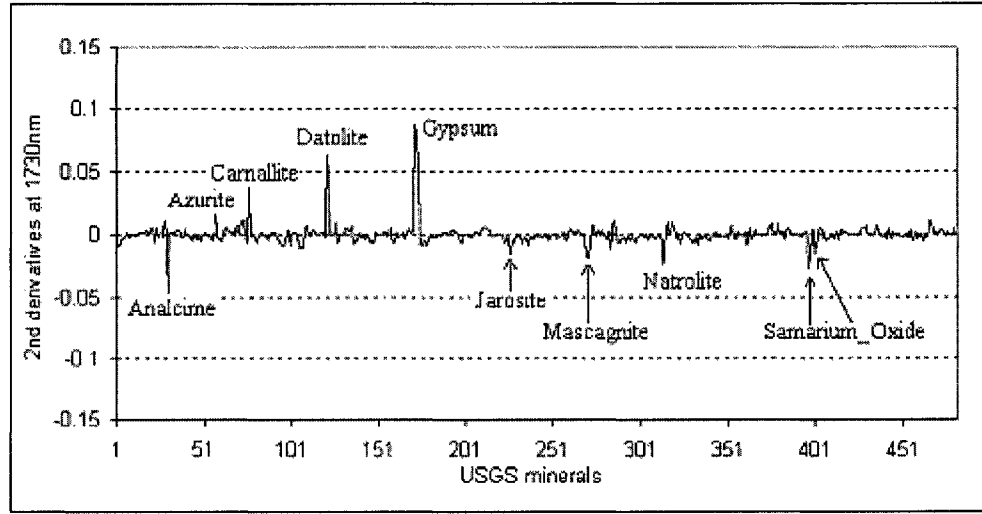


Figure A1-2 Mean, standard deviation, minimum and maximum 2nd derivative values observed for the lichen and USGS mineral library at 1730nm and 2100nm. The statistics for lichens and minerals were calculated respectively from 85 spectra over 5 lichen species 481 spectra for 423minerals. The squares are mean values; the boxes are for mean \pm 1STD; the whiskers for maximum and minimum values.



(a)



(b)

Figure A1-3 Second order derivative values at 1730nm (b) and 2100nm (a) for mineral spectra of the USGS library. The x-axis is the index # of the minerals in the USGS library.

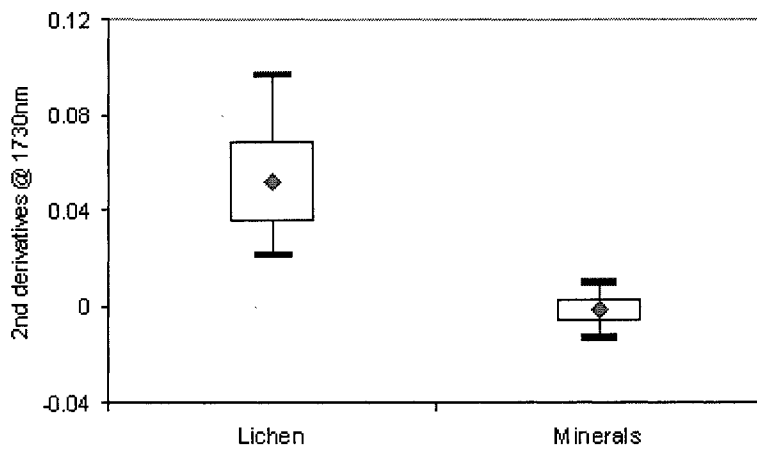


Figure A1-4 Mean, standard deviation, minimum and maximum 2nd derivative values observed for the lichen and USGS mineral library at 1730nm and 2100nm (9 minerals identified in Figure A1-2b excluded). The squares are mean values; the boxes are for mean \pm 1STD; the whiskers for maximum and minimum values.

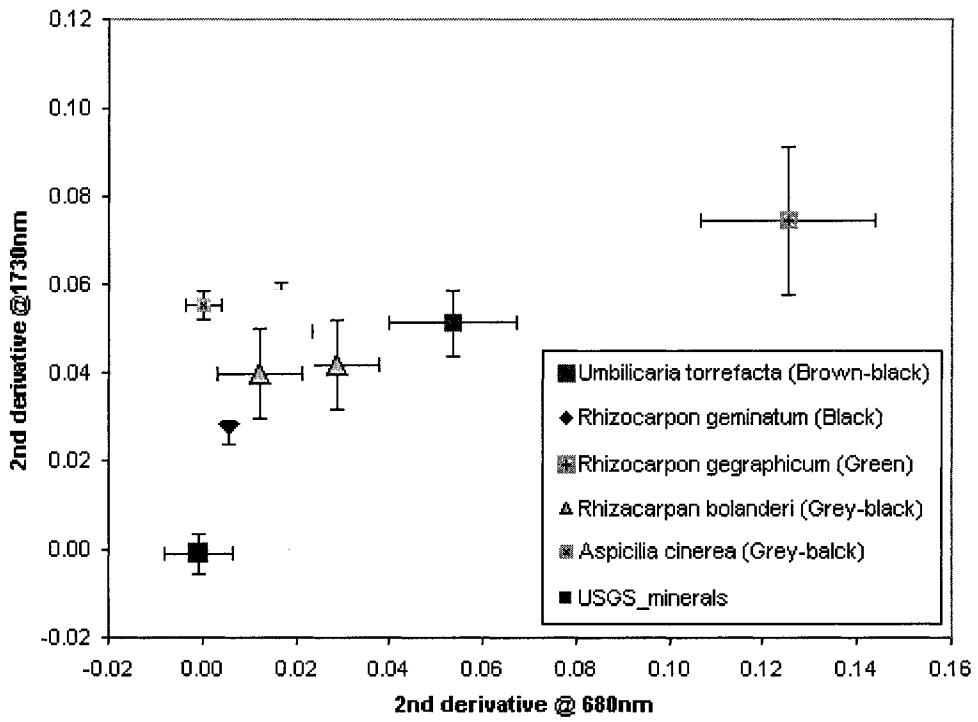


Figure A1-5. Mean 2nd derivative values of 5 lichen species at 680nm and 1730 nm. Error bars include one standard deviation.

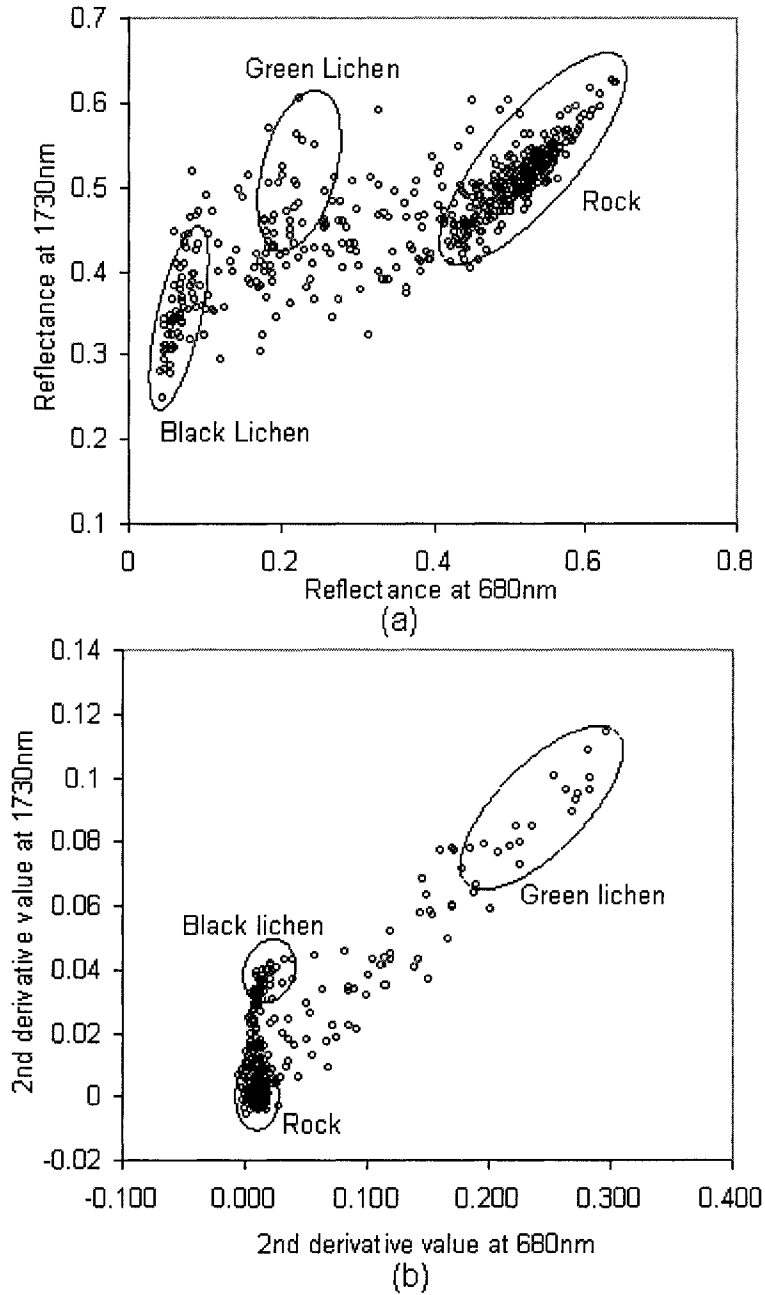


Figure A1-6 Scatter plots of reflectance (a) and 2nd derivative values (b) at 680nm and 1730nm measured from the lichen encrusted quartzite sample. Pure pixels for three surface types are marked by circles.